Abstract

Some aspects of the three body problem are investigated with a view to understanding more fully some fundamental processes occurring in stellar dynamics.

Three-body encounters in a stellar system can result in the formation of a binary system if the third star carries away sufficient kinetic energy to leave the other two bound. Subsequent encounters with such a binary are one of the main mechanisms for dynamical evolution of the system. In chapter two the energy change in a hard binary is calculated when the third star moves on a distant nearly parabolic orbit. Previous results fail in certain important cases (e.g. a circular binary), and the new results give a complete treatment.

Chapters three and four are motivated by the problem of determining the rate at which stars escape from a globular cluster. This process has important consequences for the evolution of systems of globular star clusters. Hénon(1988) developed a *model* problem which mimics chaotic aspects of a star's motion within a globular cluster. This model (chapter three) describes a particle bouncing on an inclined surface and is used to understand the mechanism underpinning the escape process in globular clusters. Orbital trajectories of escaping stars are investigated in chapter four by applying parts of the theory presented in chapter three. The motion of a star within a globular cluster is modelled using Hill's Equations. By applying numerical integration the trajectory of a star, with given initial conditions, may be followed in phase space. Different cases are considered depending on whether the cluster moves in a circular or noncircular orbit around the centre of the galaxy. In the circular case the orbital motion is viewed on an appropriate surface of section. Escaping stars are all found to lie inside a tubular surface which connects the cluster with the outside world. In the noncircular case the initial conditions leading to stable/unstable orbits are investigated. The escape process for highly eccentric orbits is modelled by supposing that the star is subjected to an impulsive force each time the cluster moves through the galactic pericentre.

Models of Three Body Scattering and Escape

Alan Roy

Doctor of Philosophy
University of Edinburgh
2001

Acknowledgements

In presenting this Thesis I wish to acknowledge the help and encouragement I have received.

First of all I wish to thank my Supervisor, Professor Douglas Heggie, for his valuable help and experience in assisting me carry out the research presented in this Thesis.

In the second place I am most grateful to my colleagues Steven Purchase, Nikolaos Georgakarakos and Saul Nsubuga for many useful and interesting conversations. Their presence created a unique atmosphere in the office.

Thirdly, I would like to mention the names of two teachers who taught me mathematics during my years at Wick High School. Mrs Margaret Rosie and Miss Elizabeth Manson were both dedicated teachers who fostered my interest in the subject.

Fourthly I wish to put on record my appreciation of the financial help I have received from the Engineering and Physical Sciences Research Council.

Finally I wish to thank my parents for their kindness and generosity and for playing a supportive role throughout the course of the degree.

Declaration

I declare that this thesis was composed by myself and that the work contained therein is my own, except where explicitly stated otherwise in the text.

Contents

1 Introduction 4

1.1 Historical overview 4

1.2 The restricted three body problem. 5

1.2.1 Particular solutions of the restricted problem 9

1.3 Hill's Equations 11

1.3.1 Hill's Equations and Globular Clusters 12

1.3.2 Chaos and Poincaré's *"perceptive genius"* 13

1.4 The Elliptic Restricted Problem 15

1.5 Aims of the thesis 15

2 Three-Body Scattering 20

2.1 Introduction 20

2.2 Preliminaries 22

2.3 Binaries with non-circular orbits 24

2.3.1 Theory 24

2.3.2 Comparison with numerical results 30

2.4 Binaries with circular orbits 31

2.4.1 Circular Orbits/Non-equal masses 31

2.4.2 Circular orbits/equal masses 36

2.4.3 Comparison with numerical results 37

2.4.4 Second order perturbation calculation 38

2.4.5 Summary 47

3 Chaotic Scattering 48

3.1 Background to the model 50

3.2 Hénon's Model Problem using Billiards 52
3.3 The large r limit 54
3.4 Dimensionless form 57
3.5 Properties 58
3.5.1 Equations for the iterated mapping 58
3.5.2 Fixed Points 59
3.5.3 Regions in the surface of section 60
3.5.4 Asymptotic behaviour 61
3.5.5 Computation of X and w from the S sequence 62
3.6 The h-orbits 64
3.7 Symbolic Representation of an h-orbit 65
3.8 Relation between A and h 67
3.8.1 Non-round A 68
3.8.2 Round A, $0 < A < 1$ 69
3.9 Escape Distributions I 71
3.9.1 Numerical Approach 79
3.10 Chaotic Transport 80
3.10.1 Mathematical Framework 82
3.10.2 Turnstile Dynamics 84
3.11 Escape Distributions II 88
3.11.1 Area of the lobe 88
3.11.2 Escape rates 90
3.11.3 Analytical results 93
3.11.4 Numerical results 99
3.11.5 "Brute force" calculation 100
3.12 Summary 100

4 Globular Clusters and Hill's Problem **102**

4.1 Introduction 102
4.2 Formulation of the problem 103
4.2.1 Hamiltonian Formulation 104
4.3 Analytical Theory 106

4.3.1 Equilibrium Points 106
4.3.2 Linearisation around the Equilibrium Points 107
4.3.3 The limiting curves. 109
4.3.4 An approximate relationship between A and $H - H_{crit}$. 110
4.4 Numerical Investigation 112
4.4.1 The stable and unstable manifolds. 112
4.5 Comparison with Hénon's model 121
4.5.1 The Escape Channels 128
4.5.2 The h-orbits 130
4.6 The Escape Flux 132
4.6.1 Discrete Case 132
4.6.2 Continuous Case 133
4.6.3 Analytical determination of $\mu(E_0)$. 137
4.7 Escape in the 3-Dim Hill Problem 138
4.7.1 Analytical determination of $\mu(\mathcal{E}_0)$. 143
4.8 The Elliptic Hill Problem 143
4.8.1 The Quasi-Periodic Orbits 145
4.8.2 Regularisation 147
4.8.3 Escape Analysis of h-orbits. 150
4.8.4 Escape at high eccentricities 153
4.9 Conclusion 158

A Integral Formulas **164**

Chapter 1

Introduction

1.1 Historical overview

The three body problem is a classical problem in mathematics which emerged shortly after the publication of Newton's *Principia* in 1687. On the surface it appears remarkably simple but this impression is deceptive. It is, in fact, a complicated nonlinear problem which has challenged the minds of many distinguished mathematicians throughout history. The excellent book by June Barrow-Green(1996) reviews the history of the problem from the time of Newton to the present day. This book is the source from which the historical details presented in this chapter are taken.

In general we consider three point masses, and assume that the bodies move under the influence of their mutual gravitational attraction. A three body system which serves as a useful example is the system consisting of the sun, the earth and the moon. In the early days of navigation it was of practical concern to be able to describe the motion of the moon, and the outcome of much research in this area came to be known as Lunar Theory. Mathematical theories were developed which sought to find approximate solutions to the motion of the moon based on series expansions. The first successful approximation was discovered by Clairaut(1747) using infinite series solutions to a much simplified system of differential equations. In recognition of his paper *Théorie de la Lune* he was awarded a prize by the St. Petersburg Academy.

In the meantime Euler and Lagrange were considering many new and important aspects of the problem and this culminated in their sharing of the *Prix de l'Academie de Paris* in 1772. In particular Euler had devised an innovative formulation of what is known as the restricted problem (cf. sec. 1.2) using a rotating coordinate system. The (planar) restricted problem is a special case of the three body problem in which two of the bodies move in circular orbits around their centre of mass whilst the third body, which is assumed to be a massless particle, moves in the plane defined by the two revolving bodies. For his part in the prize Lagrange had succeeded in showing that the three body problem could be reduced from a system of order eighteen to a system of order seven. This was later reduced to a sixth order system in 1843 by Jacobi. Jacobi also showed that Euler's formulation of the restricted problem could be represented by a fourth-order system of differential equations, one integral of which (the Jacobian integral) was found (cf. sec. 1.2). Further work was carried out by the American mathematician G.W. Hill who used the Jacobian integral to impose constraints on the motion of the massless particle. These constraints are known (in geometrical terms) as the *zero velocity curves.*

1.2 The restricted three body problem.

While the *general* three-body problem, in which all three bodies have finite mass, is considered in chapter two of this thesis, the *restricted* problem provides a good approximation for several real physical situations. For example, one could consider the motion of the moon around the earth in the presence of the sun. The earth's orbit about the sun is very close to being circular (the eccentricity is approximately 0.017) and the motion of all three bodies is almost coplanar. Furthermore, the mass ratios and mean distances between the bodies are approximately in keeping with the assumptions of the restricted problem.

The derivation of the differential equations of motion for the restricted problem is as follows. Let m_1 and m_2 denote the masses of the two finite bodies.

Distance is rescaled to make the mutual distance between the two massive bodies (or primaries) unity; mass is rescaled to make the sum of the masses = 1; time is rescaled to make the gravitational constant $G = 1$. The 'average' angular velocity is defined as the /emphmean motion. A consequence of the choice of units is that the mean motion n is unity. This is clear from Kepler's third law, which here takes the form

$$n = \frac{\sqrt{G(1-\mu+\mu)}}{a^{\frac{3}{2}}}.$$

where a is the semi-major axis of the elliptical orbit. We work in a barycentric frame of reference and write $m_1 = 1 - \mu$ and $m_2 = \mu$. (In general $\mu = \frac{m_2}{m_1+m_2}$). If the coordinates of m_1, m_2 and the third particle are (ξ_1, η_1), (ξ_2, η_2) and (ξ, η) respectively and

$$r_1 = \sqrt{(\xi - \xi_1)^2 + (\eta - \eta_1)^2}$$

$$r_2 = \sqrt{(\xi - \xi_2)^2 + (\eta - \eta_2)^2},$$

then the equations of motion of the third particle are

$$\frac{d^2\xi}{dt^2} = -(1-\mu)\frac{(\xi - \xi_1)}{r_1^3} - \mu\frac{\xi - \xi_2}{r_2^3} \tag{1.1}$$

$$\frac{d^2\eta}{dt^2} = -(1-\mu)\frac{(\eta - \eta_1)}{r_1^3} - \mu\frac{\eta - \eta_2}{r_2^3}. \tag{1.2}$$

A new frame of reference (x, y) is now introduced having the same origin as before but now rotating in the (ξ, η) plane. In the new coordinate system the primaries occupy fixed positions on the x-axis.

The equations linking the old and new variables are

$$\xi = x\cos t - y\sin t \tag{1.3}$$

$$\eta = x\sin t + y\cos t. \tag{1.4}$$

Similar equations exist for (ξ_1, η_1) and (ξ_2, η_2).

We can easily find expressions for eqns(1.1) and (1.2) in terms of x and y. This is achieved by differentiating eqns(1.3) and (1.4) twice, with respect to t, and substituting the resulting expressions into eqns(1.1) and (1.2). After further manipulation we obtain the equations

$$\frac{d^2x}{dt^2} - 2\frac{dy}{dt} = x - (1-\mu)\frac{(x - x_1)}{r_1^3} - \mu\frac{(x - x_2)}{r_2^3}$$

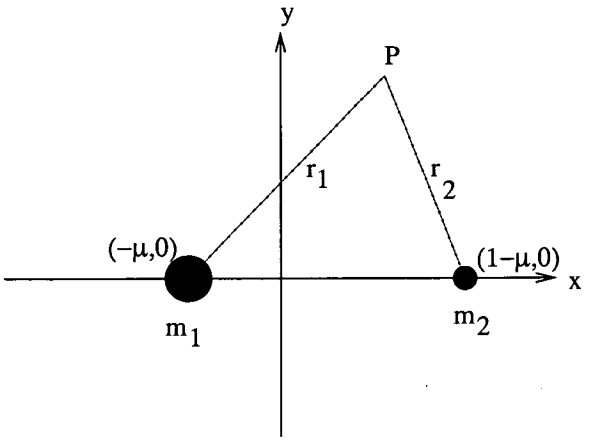

Figure 1.1: The restricted problem.

$$\frac{d^2y}{dt^2} + 2\frac{dx}{dt} = y - (1-\mu)\frac{(y-y_1)}{r_1^3} - \mu\frac{(y-y_2)}{r_2^3}.$$

The angular velocity of the rotating frame is such that $y_1 = y_2 = 0$. The above equations therefore become

$$\frac{d^2x}{dt^2} - 2\frac{dy}{dt} = x - (1-\mu)\frac{(x-x_1)}{r_1^3} - \mu\frac{(x-x_2)}{r_2^3} \tag{1.5}$$

$$\frac{d^2y}{dt^2} + 2\frac{dx}{dt} = y - (1-\mu)\frac{y}{r_1^3} - \mu\frac{y}{r_2^3}. \tag{1.6}$$

The advantage of using the rotating frame is that $x_1(=-\mu)$ and $x_2(=1-\mu)$ are time independent. The two second order differential equations in (1.5) and (1.6) may be replaced by a set of four first order equations and therefore represent a system of order four. In 1836 Jacobi showed that the system could be reduced further to one of order three through the introduction of an integral (known today as the Jacobian integral). This integral is straightforward to derive (cf. Murray and Dermott 2000). Firstly observe that eqns(1.5) and (1.6) may be written as

$$\frac{d^2x}{dt^2} - 2\frac{dy}{dt} = \frac{\partial U}{\partial x} \tag{1.7}$$

$$\frac{d^2y}{dt^2} + 2\frac{dx}{dt} = \frac{\partial U}{\partial y} \tag{1.8}$$

where

$$U = \frac{1}{2}(x^2+y^2) + \frac{1-\mu}{r_1} + \frac{\mu}{r_2}$$

and

$$r_i^2 = (x - x_i)^2 + y^2, \quad i = 1, 2.$$

Multiplying these by

$$2\frac{dx}{dt} \text{ and } 2\frac{dy}{dt}$$

respectively and adding gives

$$2\frac{dx}{dt}\frac{d^2x}{dt^2} + 2\frac{dy}{dt}\frac{d^2y}{dt^2} = 2\frac{dx}{dt}\frac{\partial U}{\partial x} + 2\frac{dy}{dt}\frac{\partial U}{\partial y}. \tag{1.9}$$

Finally (1.9) may be integrated with respect to time to give

$$\left(\frac{dx}{dt}\right)^2 + \left(\frac{dy}{dt}\right)^2 = 2U - C \tag{1.10}$$

which may be written as

$$V^2 = 2U - C$$

where C is a constant and V is the speed in the rotating frame.

This equation, which connects the magnitude of the velocity vector of the particle to its location, is known as the Jacobi integral. The integral may be used to establish certain forbidden regions from which the particle is excluded. These regions can be seen by equating the left hand side of eqn(1.10) to zero. We then obtain the equation of a curve which separates phase space into three connected parts depending on whether the velocity is real or imaginary - see fig(1.2).

The American mathematician and astronomer George W. Hill (1838-1914) was the first to apply this principle to celestial mechanics. Having derived a model for the motion of the moon he was able to show that the earth-moon distance must remain bounded for all time. He therefore proposed that the moon can never "escape" and must always remain within a certain distance of the earth. Such ideas were carried further by George Darwin who, in 1897, made further deductions relating to the stability of the moon's orbit. One deficiency in Hill's simplified model is that it neglects the eccentricity of the Earth's orbit and the effect of the moon's mass. A refined model, taking these factors into consideration, was proposed by Szebehely and McKenzie (1977). The authors show that in these circumstances escape becomes possible.

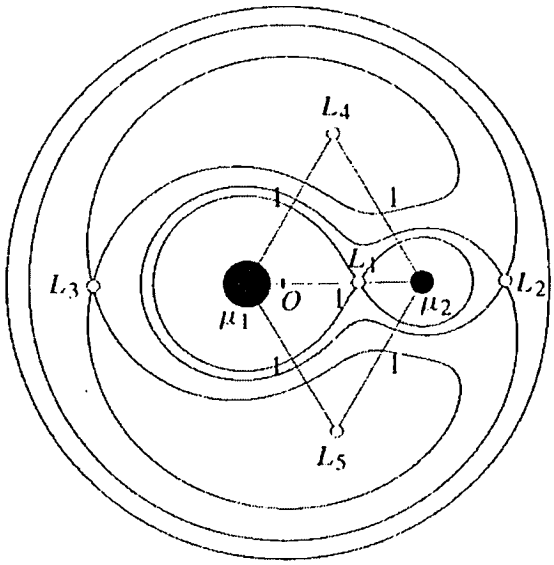

Figure 1.2: This diagram (from Murray 2000) shows the curves obtained by equating the left hand side of eqn(1.10) to zero. Three critical values of the constant C are considered. In this case $\mu_1 = -\mu$ and $\mu_2 = 1 - \mu$.

1.2.1 Particular solutions of the restricted problem

An equilibrium solution is one in which all three bodies remain in a fixed geometric configuration for all time. Euler established particular (collinear) solutions to the restricted problem in which all the bodies remain at fixed positions on a straight line. Lagrange obtained equilateral solutions in which all the bodies move as if they were attached to the vertices of a triangle. Both the line and the triangle rotate with constant angular velocity about the centre of mass of the bodies.

Associated with these solutions are five equilibrium points in the rotating frame which are characterised by the fact that if the third particle is placed at any one of these points, with zero velocity, it will stay there forever. The terms "*libration points*" and "*Lagrangian points*" are also used, with the notation L_1, ... L_5 - see fig(1.3). The collinear points are represented by the points L_1, L_2 and L_3 and the equilateral points are represented by L_4 and L_5. At the Lagrangian points the forces acting on the third body are balanced.

Observational evidence relevant to these equilibria was obtained in 1906 by

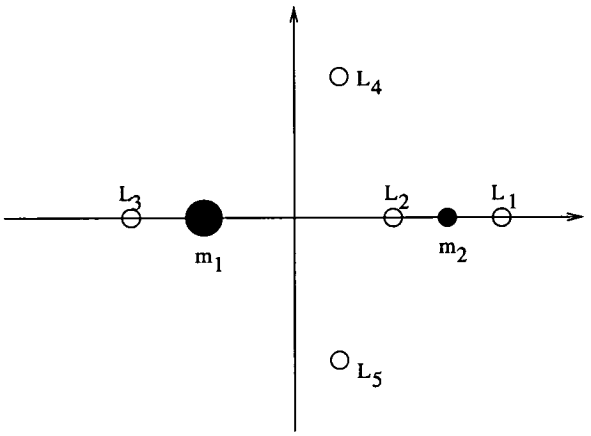

Figure 1.3: The five Lagrangian points.

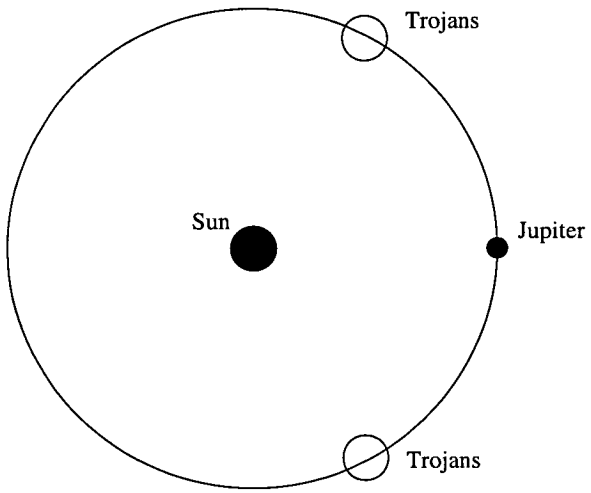

Figure 1.4: Jupiter and the Trojans.

Max Wolf. Around this time the first of two groups of asteroids located close to the L_4 and L_5 positions for the Sun and Jupiter were discovered. These asteroids are known as the Trojans - see fig(1.4).

1.3 Hill's Equations

Since the mass of the earth is tiny compared to that of the sun, Hill considered a limiting case of the restricted problem in which $\mu = \frac{m_2}{m_1+m_2} \to 0$. His approximate model for the moon assumed that

(i) the solar parallax is zero (which implies that the distance between the earth and the moon is very small compared to the distance between the sun and the earth),

(ii) the solar eccentricity is zero (which implies that the earth's orbit is taken to be circular) and

(iii) the lunar inclination is zero.

Hill's equations may be derived from the restricted problem as follows. A translation is performed along the x-axis so that the coordinate system is now centred on the smaller primary. We then allow $\mu \to 0$ and rescale the units so that we may focus our interest on the region around the smaller primary i.e. the earth. Hill's equations in this new coordinate system (sometimes referred to as *Hill's coordinates*) are given by

$$\ddot{x} - 2\dot{y} = 3x - \frac{x}{(x^2+y^2)^{\frac{3}{2}}}, \tag{1.11}$$

$$\ddot{y} + 2\dot{x} = -\frac{y}{(x^2+y^2)^{\frac{3}{2}}}. \tag{1.12}$$

Hill sought periodic solutions to these equations which were invariant under $x \to -x$ and $y \to -y$. These solutions are therefore symmetric with respect to the x and y axes separately under a time reversal. (The solution whose period corresponded to that of the moon is known today as *Hill's variational orbit*). Hill(1877) described these periodic orbits in a paper which he published privately on the motion of the lunar perigee. A more detailed treatment is contained in Hill's 1878 paper which he submitted to the *American Journal of Mathematics*.

Hill's approach was based on the assumption that the periodic orbits could be represented as Fourier series. By substituting the Fourier series into eqns. (1.11) and (1.12) he was able to determine the coefficients as functions of a parameter m which is defined by

$$m = \frac{n'/n}{1 - n'/n}.$$

(Here n' and n are, respectively, the mean motions (or 'average ' angular velocities) of the sun around the earth-sun system and of the moon around the earth.) In order to simplify the notation Hill introduced complex variables before carrying out the substitution. By varying the value of m, Hill was able to consider a family of periodic orbits.

Though Hill's discoveries were of great importance to astronomy, it is worth noting that it was some time before his work was fully appreciated by his peers. To some extent this may have been due to Hill's nationality. In America, during the nineteenth century, mathematics still remained in its infancy. June Barrow-Green cites evidence suggesting that Hill's particular style of mathematics made his work difficult to comprehend.

1.3.1 Hill's Equations and Globular Clusters

Hill's equations can also be used to understand the mechanism whereby stars escape from a globular cluster. The rate at which stars escape from a globular cluster is affected by the gravitational field of a galaxy which may be represented by the distant perturber in Hill's problem. In particular the escape rate depends critically on a pair of periodic orbits (called Lyapounov orbits) which occur at either side of the cluster near the Lagrangian points. A link exists here between the dynamics of escaping stars (chap. 3,4) and three-body scattering (chap.2). In the *elliptic* generalisation of Hill's problem, stars orbiting the primary may become unbound by the perturbing action of the galaxy; the scattering problem is concerned with the effects of a perturber moving on a *parabolic* relative orbit.

In applying Hill's equations to a globular cluster we make the assumptions that both the galaxy and the cluster can be reduced to point masses and that

the orbit of the cluster is circular. These approximations mean that we have an instance of the circular restricted problem, the three bodies being the galaxy, cluster and star. Moreover, the mass ratio $\mu(= M_{cluster}/M_{galaxy})$ is typically of the order 10^{-9} to 10^{-6} and this means that the system may be modelled by Hill's equations.

1.3.2 Chaos and Poincaré's *"perceptive genius"*

The advent of fast computers has brought about many interesting developments. It is now possible to follow the trajectories of individual orbits in Hill's problem using numerical integration. Hénon(1970), for example, carried out a numerical exploration of Hill's problem and suggested that there are no upper bounds on the dimension of quasi-periodic retrograde satellites.

Numerical techniques have also revealed the existence of chaotic motions in certain regions of phase space. Froechlé(1991), for example, has used such techniques to study asteroidal orbital chaos.

It is remarkable, however, to note that Poincaré had, in fact, discovered the existence of chaos long before the invention of modern computers. In the third volume of his memoir *Les Méthodes Nouvelles de la Mécanique Céleste* Poincaré(1899) describes what is known today in the theory of dynamical systems as a *homoclinic tangle.* His description, which deals with chaotic aspects of the restricted problem, talks about two curves *"intersecting (to) form a kind of net, web or infinitely tight mesh; neither of these two curves can ever intersect itself, but must fold back on itself in a very complex way in order to intersect all the links of the chain infinitely often"*. Poincaré wrote "on sera frappé de la complexité de cette figure que je ne cherche même pas à tracer". Today such figures are drawn with the aid of computers. The basic structure of a typical homoclinic tangle is shown schematically in fig(1.5). In chapters three and four the importance of a homoclinic tangle is shown in the context of understanding how stars escape from a globular cluster.

Poincaré's discovery seemed little more than a mathematical curiosity at the time of publication. But George Darwin(1900) accurately predicted that

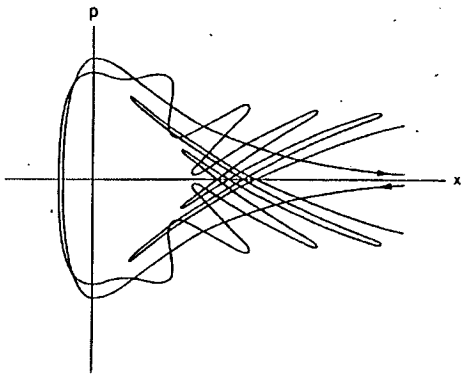

Figure 1.5: A homoclinic tangle (after Wiggins 1992).

"*for half a century to come it (Méthodes Nouvelles) will be the mine from which humbler investigators will excavate their materials*". It has been said that Darwin was somewhat conservative in his outlook and indeed his prediction was too restricted. Even today it would be fair to say that Poincaré's results continue to find important applications in the theory of dynamical systems.

The phenomenon of chaos provides an interesting link between two problems considered in this thesis: the scattering problem and the escape problem. Scattering problems concern the approach of a third body to a binary, and its eventual ejection; escape concerns the ejection of one component of a binary by the action of a third body.

It has been noticed that scattering problems exhibit the hall-marks of chaos, in particular, sensitive dependence on initial conditions (Eckhardt 1988, Boyd and McMillan 1992,1993). Petit and Hénon(1986) noticed in a different context, that this is linked with the dynamics in the vicinity of a certain periodic orbit near the Lagrangian point. For this reason Hénon developed a simplified model of the dynamics, and it turns out that this model is ideally suited to developing an understanding of escape processes. These processes depend on the chaotic dynamics related to the aforementioned periodic orbit, and is the main theme developed in chapter three.

1.4 The Elliptic Restricted Problem

The simplest generalisation of the circular restricted problem is to consider the case in which the primaries describe elliptical orbits. This problem is considerably more complicated since the differential equations governing the motion of the particle no longer possess a time-invariant quantity such as the Jacobi integral. It does, however, serve as a more realistic model for many observed phenomena in our solar system and beyond. The main asteroid belt between Mars and Jupiter is a useful example. Studies in recent times (e.g. Milani and Nobili 1984) have investigated to what extent the eccentricity of Jupiter's orbit affects the rate at which mass is lost from the outer asteroid belt. In addition to this, Jupiter's eccentricity is known to perturb the orbital elements of the Trojan asteroids (see Erdi 1981). In both cases the authors use the elliptic restricted problem as a basic model. Keenan (1981) uses the elliptic restricted problem to investigate the stability of stellar orbits in open and globular clusters. It has also been used by Benest(1988, 1989, 1996, 1998) to search for the existence of stable planetary orbits in stellar systems. A technique described in Benest(1998) is used to explore orbital stability and is implemented in chapter four.

1.5 Aims of the thesis

In this Thesis we shall investigate aspects of the three body problem which are of relevance in stellar dynamics.

Chapter two deals with three body scattering. Three body scattering is one of the fundamental processes which occur in the study of star clusters. Its importance lies in the fact that when a binary and a third star interact with each other energy changes occur which affect the evolution of the entire system.

Globular clusters are found to undergo a "collapse phase" in which the inner regions of the cluster accelerate towards an infinite central density. It is rather like the gravitational collapse leading to the formation of individual stars. Existing models break down in these circumstances due to the appearance of

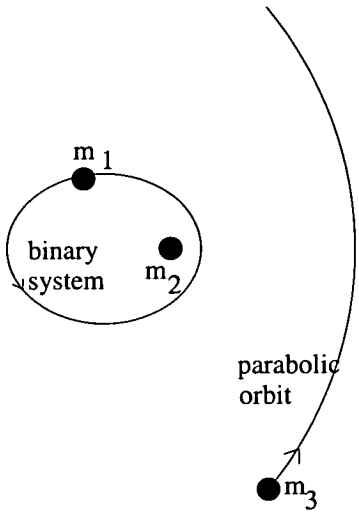

Figure 1.6: Three body scattering.

singularities in the theory. New physical processes emerge which release energy and counteract the gravitational collapse. A detailed description of this may be found in Elson and Hut(1987). In the evolution of a single star this process is nuclear burning. In that of a cluster it corresponds to the formation of binaries. Encounters between single stars and binaries then cause the binaries to become more tightly bound and to release energy.

In chapter two we present an approximate analytical technique for computing the change in the binding energy of a binary when the third star moves in a distant parabolic orbit (fig 1.6). This is an example of a tidal encounter since we assume that the distance of the third star always considerably exceeds the size of the binary. The binary is therefore perturbed only slightly. Different cases arise depending on the choice of masses and the angle of inclination of the plane in which the third star moves. Numerical experiments are performed as a means of checking the analytical theory.

Chapters three and four deal with escape rate distributions. Escape rate distributions are important in another physical process which occurs during the evolution of a cluster, namely, that of *evaporation.* Evaporation occurs when stars receive enough energy to escape from the cluster into the gravitational field of the galaxy. The rate of evaporation may be thought of in terms of an escape flux. The number of stars which escape in a given time are those contained in

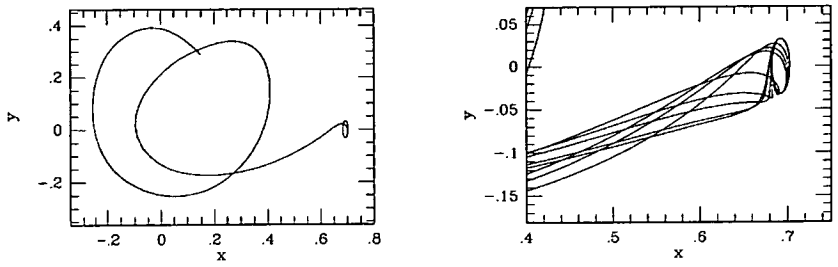

Figure 1.7: The tubular surface within which escaping stars are found (after Fukushige and Heggie 2000). The "mouth" (or cross-section) of the pipe is shown on the right, close to one of the Lagrangian points. The centre of the cluster is at the origin. If a star's coordinates (x, y) satisfy $|x| > 0.693\ldots$ then that star is considered to lie *outside* the cluster. More will be said about this in chapter four.

a certain volume of phase space, and the rate at which phase space is detrained from the cluster can be considered as a flux. In fact, escaping stars are all found to lie inside a tubular surface resembling a pipe whose cross-sectional area is a function of the energy - see fig.(1.7). This was first discovered by Fukushige and Heggie(2000). (There are, in fact, two pipes which are connected to either end of the cluster.) This implies that the flux of escapers is a function of the energy. If the energy, E, lies below some critical value E_{crit}, the cross-sectional area vanishes and hence the flux is zero. As E increases beyond E_{crit} the mouth of our hose pipe expands and the flux of escapers increases accordingly. The situation is analogous to turning on a kitchen tap. When the tap is turned off the valve is closed and no water flows; this corresponds to $E \leq E_{crit}$. As the tap is turned on, the valve opens. The flow of water increases depending on the position of the tap; this corresponds to $E > E_{crit}$.

The rate at which phase space escapes is first investigated in chapter two using a *model* problem devised by Hénon (1988). Hénon's model, which describes the motion of a particle bouncing on an inclined surface, mimics the behaviour of Hill's equations in certain respects. In this model there is a particular region of the planar phase space which may be thought of as resembling the interior of

the cluster, to which a particle may remain temporarily bound. After a certain number of bounces the particle usually escapes to an unbounded region of the phase space in the same way that an escaping star is eventually carried out of the cluster via the interior of the tubular surface. Our goal is to understand the reasons for the distribution of escape times. If we can do this for Hénon's simplified model problem it is hoped that the same knowledge may be applied to Hill's equations. This would be of value to our understanding of the dynamics of globular clusters.

In the latter part of chapter three this escape mechanism is described in precise mathematical terms and some necessary background theory known in the language of dynamical systems as *turnstile dynamics* (Wiggins 1992) is presented. We show how this theory may be applied to Hénon's model to calculate an escape distribution for a general class of orbits. Numerical and analytical techniques analogous to the approach by Rom-Kedar et al. (1988) in another context are presented.

The central theme of the investigation in chapter three is to ascertain the rate at which stars escape from a globular cluster. In chapter four we compute the flux of escapers by applying parts of the theory in chapter three to Hill's problem. This is most easily done when the orbital trajectories of escaping stars are viewed on a particular surface of section (known as a *Poincaré surface*). The "pipe" (described above) leaves an impression of its cross section every time it intersects the surface of section. A revealing picture of the way orbits escape begins to emerge and the similarities between Hénon's model and Hill's problem become more striking. It is possible to identify those regions of phase space (lying on the surface) which are immediately detrained from the cluster. The techniques of chapter three are then used to compute an escape distribution.

When the cluster moves on an eccentric orbit the rate of evaporation of stars increases when the cluster passes through pericentre, i.e. its closest distance to the galactic centre. The latter part of chapter four explores this phenomenon for high eccentricities. Escape times are also investigated for a two dimensional family of orbits using the Elliptic Hill equations as a basic model. (The Elliptic

Hill equations arise from the limiting case of the Elliptic Restricted Problem in which $\mu \to 0$.) Periodic orbits are also studied in the context of this discussion.

Chapter 2

Three-Body Scattering

2.1 Introduction

Different types of encounter arise when a star interacts with a binary. The following classification which is taken from Heggie(1975) describes some important background theory.

Suppose that a third body approaches a binary, whose initial binding energy [1] is x, with a relative velocity of magnitude V_0 when the separation is still very large. During the ensuing encounter, let the binding energy of the pair change by an amount y, and, if the third body escapes to infinity afterwards, let its final velocity be V_1. If all the masses are equal to m, conservation of energy in the rest frame of the centre of mass of the three bodies implies that

$$\frac{1}{3}mV_1^2 = \frac{1}{3}mV_0^2 + y. \tag{2.1}$$

To see this, suppose that the third body moves with velocity v in the rest frame. The barycentre of the binary will then move with velocity $-v/2$ - see fig(2.1). The total kinetic energy (before the interaction) is given by

$$\frac{1}{2}mv^2 + \frac{1}{2}(2m)(-\frac{v}{2})^2 = \frac{3}{4}mv^2.$$

The relative velocity V_0 (in terms of v) is

$$V_0 = v - (-\frac{v}{2}) = \frac{3v}{2}$$

[1] The binding energy is the absolute value of the potential energy of the binary. It is the energy, which, when added to the binary causes the stars to separate completely.

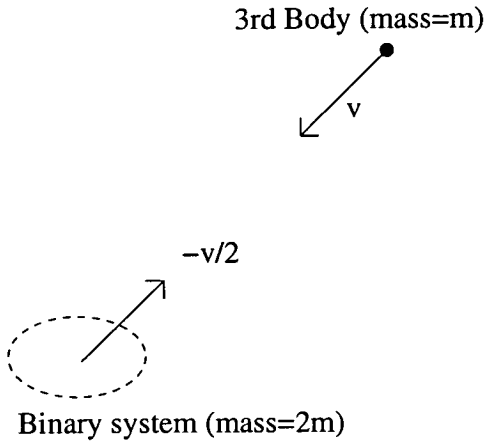

Figure 2.1: This shows (schematically) the third body as it approaches the binary; the velocities are given in the rest frame of the centre of mass of the three bodies.

and the kinetic energy is therefore $mV_0^2/3$. After separation the kinetic energy is $mV_1^2/3$ and since the total energy is conserved we obtain eqn(2.1).
If $y > 0$, the third body will escape, and the encounter results in a "de-excitation". If $-\frac{1}{3}mV_0^2 < y < 0$, escape of the third body still occurs, and if in addition $-x < y$ then the binary survives the encounter, which is referred to as an "excitation". On the other hand, if $-\frac{1}{3}mV_0^2 < y < -x$, the binary is destroyed, the process known in atomic physics as "ionization". It may possibly happen in this case that the third body forms a new binary with one component of the old. Such an event, called an "exchange" encounter, will occur in general when $y < -x$ and $y < -\frac{1}{3}mV_0^2$, for these conditions imply the original binary is disrupted and yet, by eqn(2.1), the third body is unable to escape to infinity from the centre of mass of the old binary. If finally, $-x < y < -\frac{1}{3}mV_0^2$, no particle escapes to infinity, at least not immediately, and the outcome of such a "resonance" encounter is decided by further interactions.

The particular problem which is investigated in this chapter is concerned with the effect of a passing third star on the energy of a hard binary. The binary is *hard* since its binding energy far exceeds the kinetic energy of the third star, i.e. $x >> mV_0^2/3$ (cf. Spitzer 1986). Theoretical and numerical techniques are used to compute the energy change when the third body remains *outside* the

binary and moves on a nearly parabolic path. This study is motivated by a need to understand the release of energy in 3-body encounters in star clusters.

Heggie (1975) has computed a formula for the energy change. His formula suffers from the following deficiencies.

(i) Certain coefficients which depend on the eccentricity, e, and the orientation of the orbits are not worked out explicitly; this is put right with a full rederivation in sec(2.3).

(ii) It fails when the binary is circular; this is rectified in sec(2.4.1) for non-equal masses and in sec(2.4.2) and (2.4.4) in the case of equal masses.

For circular orbits and equal masses it was found that the lowest-order approximation failed to account for the non-zero mean value of the change in energy of the binary observed in the numerical data. The theory is corrected in sec(2.4.4) using second order perturbation theory.

Sections (2.3) and (2.4.2) largely follow an unpublished manuscript by Haddow and Heggie(1996) but with more complete numerical results. Sections (2.4.1) and (2.4.4) are entirely new.

2.2 Preliminaries

Let m_1 and m_2 be the masses of the components of the binary, and m_3 be the mass of the third star approaching the binary from infinity. Let $\mathbf{r}$ be the position of star 2 relative to star 1 and let $\mathbf{R}$ be the position of star 3 relative to the barycentre of the binary. The situation is illustrated in fig(2.2).

Notation: G is the universal constant of gravitation, $M_{12} = m_1 + m_2$, $M_{123} = m_1 + m_2 + m_3$, and $\mu_i = m_i/M_{12}$ $(i = 1, 2)$ so that $\mu_1 + \mu_2 = 1$.

The equations governing the relative motion of these three stars are easily derived from the equations of motion of the 3-body problem, and may be written in the form

$$\ddot{\mathbf{r}} = -GM_{12}\frac{\mathbf{r}}{r^3} + Gm_3\frac{\partial \mathcal{R}}{\partial \mathbf{r}} \tag{2.2}$$

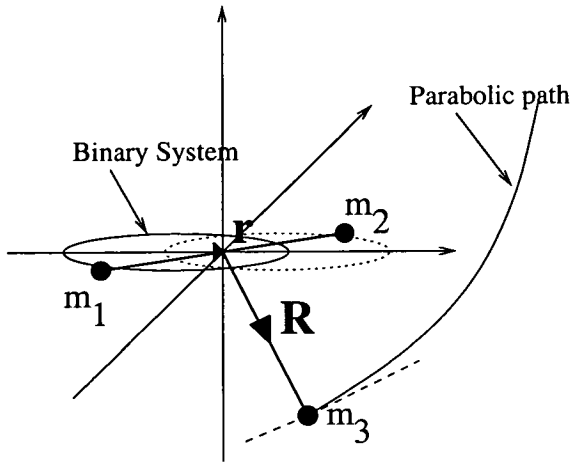

Figure 2.2: The frame of the barycentre of the binary showing the approximate elliptical motion of bodies m_1, m_2 and the approximate parabolic path of the third star.

$$\ddot{\mathbf{R}} = GM_{123}\mu_1\mu_2\frac{\partial \mathcal{R}}{\partial \mathbf{R}} \tag{2.3}$$

where $\mathcal{R}$ is the *perturbing function* given by

$$\mathcal{R} = \frac{1}{\mu_2\left|\mathbf{R}+\mu_2\mathbf{r}\right|} + \frac{1}{\mu_1\left|\mathbf{R}-\mu_1\mathbf{r}\right|}.$$

(Since the third body moves on a *distant* parabolic orbit we may assume that $|\mathbf{R}| >> |\mathbf{r}|$.) This can be expanded in terms of Legendre polynomials (Plummer(1960), Heggie(1975)) to give [2]

$$\mathcal{R} = \frac{1}{R}\left(\frac{1}{\mu_2}+\frac{1}{\mu_1}\right) + \frac{1}{2}\frac{r^2}{R^3}\left(3\left(\frac{\mathbf{r}.\mathbf{R}}{rR}\right)^2 - 1\right) + O\left(\frac{r^3}{R^4}\right). \tag{2.4}$$

The energy of the binary, ε, is given by

$$\varepsilon = -\frac{Gm_1m_2}{r} + \frac{m_1m_2}{2M_{12}}\dot{\mathbf{r}}^2.$$

Its derivative with respect to time is

$$\begin{aligned}\frac{d\varepsilon}{dt} &= \frac{m_1m_2}{M_{12}}\left(GM_{12}\frac{\mathbf{r}}{r^3}+\ddot{\mathbf{r}}\right).\dot{\mathbf{r}} \\ &= \frac{Gm_1m_2m_3}{M_{12}}\dot{\mathbf{r}}.\frac{\partial \mathcal{R}}{\partial \mathbf{r}} \quad \text{(by (2.2))}.\end{aligned} \tag{2.5}$$

[2] In many applications $\mathcal{R}$ would include a term $-\frac{1}{\mu_1\mu_2 R}$ (so that eqn(2.3) takes the form of perturbed Kepler motion) and different mass factors.

The total change in the energy of the binary over the duration of the encounter is found by integrating eqn(2.5) from $-\infty$ to ∞ with respect to time t. This means that

$$\delta\varepsilon = \int_{-\infty}^{\infty} \frac{Gm_1m_2m_3}{M_{12}} \dot{\mathbf{r}}.\frac{\partial \mathcal{R}}{\partial \mathbf{r}}\, dt. \tag{2.6}$$

2.3 Binaries with non-circular orbits

2.3.1 Theory

The integration in eqn(2.6) may be transformed by noting that

$$\frac{d\mathcal{R}}{dt} = \frac{d\mathbf{r}}{dt}.\frac{\partial \mathcal{R}}{\partial \mathbf{r}} + \frac{d\mathbf{R}}{dt}.\frac{\partial \mathcal{R}}{\partial \mathbf{R}}.$$

Eqn(2.6) is therefore equivalent to

$$\delta\varepsilon = \frac{Gm_1m_2m_3}{M_{12}} \int_{-\infty}^{\infty} \left[\frac{d\mathcal{R}}{dt} - \dot{\mathbf{R}}.\frac{\partial \mathcal{R}}{\partial \mathbf{R}}\right] dt.$$

But $\mathcal{R} \to 0$ as $t \to \pm\infty$ and so

$$\delta\varepsilon = -\frac{Gm_1m_2m_3}{M_{12}} \int_{-\infty}^{\infty} \dot{\mathbf{R}}.\frac{\partial \mathcal{R}}{\partial \mathbf{R}} dt. \tag{2.7}$$

In the first instance we use a zero-order approximation to $\mathcal{R}$ to evaluate the above integral. If the perturbation is ignored in eqn(2.2), then

$$\ddot{\mathbf{r}} = -GM_{12}\frac{\mathbf{r}}{r^3}.$$

Assuming an elliptical orbit for the binary, this has the solution

$$\mathbf{r} = a(\cos E - e)\hat{\mathbf{a}} + b \sin E \hat{\mathbf{b}} \tag{2.8}$$

(cf. Plummer 1960) where a, b are the lengths of the semi-axes of the orbit, $\hat{\mathbf{a}}$ and $\hat{\mathbf{b}}$ are unit vectors parallel to them, the eccentricity $e \equiv (a^2 - b^2)^{1/2}/a$, and E is the eccentric anomaly. It is related to the time t by Kepler's equation which is

$$n(t - t_0) = E - e \sin E \tag{2.9}$$

where t_0 is constant and n (the mean motion) is given by

$$n^2a^3 = GM_{12}. \tag{2.10}$$

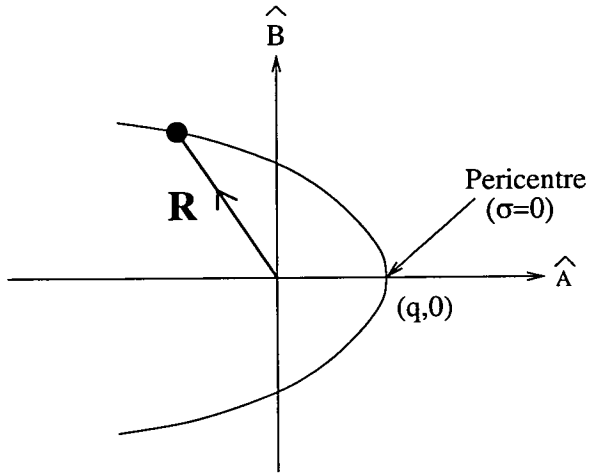

Figure 2.3: The orbital plane of motion of m_3 relative to the barycentre of the binary showing the orientation of the parabolic path of the third star with respect to the coordinate axes $(\hat{\mathbf{A}}, \hat{\mathbf{B}})$.

Similarly, substitution of the first term of eqn(2.4) into eqn(2.3) gives

$$\ddot{\mathbf{R}} = -GM_{123}\frac{\mathbf{R}}{R^3}$$

which (assuming a parabolic orbit for the third body) has the solution

$$\mathbf{R} = q(1-\sigma^2)\hat{\mathbf{A}} + 2q\sigma\hat{\mathbf{B}} \tag{2.11}$$

where q is the periastron distance of the third star to the barycentre of the binary, and $\hat{\mathbf{A}}$, $\hat{\mathbf{B}}$ are unit vectors in the directions of the axes of the relative orbit of the third body. The orientation of the parabola with respect to the axes is illustrated in fig(2.3). σ, which is a dimensionless parameter governing the parabolic orbit, is related to t by

$$\sqrt{\frac{GM_{123}}{2q^3}}t \approx \sigma + \frac{1}{3}\sigma^3. \tag{2.12}$$

(cf. Plummer 1960) We shall assume that the masses are comparable and that $q \gg a$, i.e. that the distance of closest approach of the third body much exceeds the semi-major axis of the binary. This also justifies neglect of higher-order terms in eqn(2.4).

The expressions for $\mathbf{r}$ and $\mathbf{R}$ in eqns(2.8) and (2.11) are now substituted into the expansion for

$$\frac{\partial \mathcal{R}}{\partial \mathbf{R}}$$

obtained from eqn(2.4).

Our goal is to compute the integral in eqn(2.7). It is easy to see that the first term in eqn(2.4) will vanish when inserted in eqn(2.7). The first term gives

$$\int_{-\infty}^{\infty} \dot{\mathbf{R}}.\frac{\partial \mathcal{R}}{\partial \mathbf{R}} dt = -(\frac{1}{\mu_2} + \frac{1}{\mu_1}) \int_{-\infty}^{\infty} \frac{\mathbf{R}.\dot{\mathbf{R}}}{R^3} dt$$

$$= -(\frac{1}{\mu_2} + \frac{1}{\mu_1}) \left[\frac{1}{R}\right]_{-\infty}^{\infty} = 0$$

since $R \to \infty$ as $t \to \pm\infty$. For this reason, the second term in eqn(2.4) is taken as the approximation for $\mathcal{R}$.

Since $r = a(1 - e\cos E)$ the expression for $\mathcal{R}$ is given by

$$\begin{aligned} \mathcal{R} \;=\; & \frac{1}{2R^5} \{\, 3\,[\, a^2(\cos E - e)^2(\hat{\mathbf{a}}.\mathbf{R})^2 + 2ab\,(\cos E - e)\sin E\,(\hat{\mathbf{a}}.\mathbf{R})\,(\hat{\mathbf{b}}.\mathbf{R}) \\ & + b^2(\hat{\mathbf{b}}.\mathbf{R})^2 \sin^2 E\,] - R^2a^2(1 - e\cos E)^2\,\}\,. \end{aligned} \tag{2.13}$$

An infinite expansion for any term of the form $\sin mE$ or $\cos mE$ as a Fourier series in $M = n(t - t_0)$ maybe obtained from Kepler's Eqn(2.9). For our purpose the following approximations will be used (cf. Plummer 1960) :

$$\begin{aligned} \sin E &\simeq \sin M(J_0(e) + J_2(e)) \\ \cos E &\simeq -\frac{1}{2}e + \cos M(J_0(e) - J_2(e)) \\ \sin 2E &\simeq 2\sin M(J_{-1}(e) + J_3(e)) \\ \cos 2E &\simeq 2\cos M(J_{-1}(e) - J_3(e)) \end{aligned} \tag{2.14}$$

where $J_p(e)$ is the Bessel function of order p and argument e. As mentioned by Heggie(1975) the additional terms of the expansions may be neglected since they oscillate more rapidly than $\sin M$ or $\cos M$ and it will be seen from what follows that their contribution to $\delta\varepsilon$ would be insignificant.

Eqns(2.14) are now substituted into the expression for $\mathcal{R}$ in eqn(2.13). Terms which are independent of M may be ignored since they are perfect differentials

of functions which vanish as $R \to \infty$. This yields the following expression for $\mathcal{R}$:

$$\mathcal{R} = \frac{1}{R^5}\left\{\left[\frac{3}{2}e_1a^2(\hat{\mathbf{a}}.\mathbf{R})^2 - \frac{3}{2}e_2b^2(\hat{\mathbf{b}}.\mathbf{R})^2 - \frac{1}{2}ee_3a^2R^2\right]\cos M + 3e_4ab\,\hat{\mathbf{a}}.\mathbf{R}\,\hat{\mathbf{b}}.\mathbf{R}\sin M\right\} \tag{2.15}$$

where

$$\begin{aligned} e_1 &= J_{-1}(e) - 2eJ_0(e) + 2eJ_2(e) - J_3(e) \\ e_2 &= J_{-1}(e) - J_3(e) \\ e_3 &= eJ_{-1}(e) - 2J_0(e) + 2J_2(e) - eJ_3(e) \\ e_4 &= J_{-1}(e) - eJ_0(e) - eJ_2(e) + J_3(e). \end{aligned}$$

In order to compute the integral in eqn(2.7) it is necessary to evaluate

$$\dot{\mathbf{R}}.\frac{\partial \mathcal{R}}{\partial \mathbf{R}}.$$

It can easily be shown from eqn(2.11) that

$$\begin{aligned} \mathbf{R}.\dot{\mathbf{R}} &= 2q^2(1+\sigma^2)\sigma\dot{\sigma} \\ &= 2qR\sigma\dot{\sigma}. \end{aligned}$$

This gives

$$\begin{aligned} \dot{\mathbf{R}}.\frac{\partial}{\partial \mathbf{R}}\left(\frac{(\hat{\mathbf{a}}.\mathbf{R})^2}{R^5}\right) &= \frac{2\,\hat{\mathbf{a}}.\mathbf{R}\,\hat{\mathbf{a}}.\dot{\mathbf{R}}}{R^5} - \frac{5(\hat{\mathbf{a}}.\mathbf{R})^2\,\mathbf{R}.\dot{\mathbf{R}}}{R^7} \\ &= \frac{2\,\hat{\mathbf{a}}.\mathbf{R}\,\hat{\mathbf{a}}.\mathbf{R}'\dot{\sigma}}{R^5} - \frac{10(\hat{\mathbf{a}}.\mathbf{R})^2q\sigma\dot{\sigma}}{R^6} \\ &= \frac{(2\,\hat{\mathbf{a}}.\mathbf{R}\,\hat{\mathbf{a}}.\mathbf{R}'R - 10(\hat{\mathbf{a}}.\mathbf{R})^2q\sigma)\,\dot{\sigma}}{R^6} \end{aligned} \tag{2.16}$$

where

$$R' = \frac{dR}{d\sigma}.$$

The other terms in eqn(2.15) are handled in similar fashion. Writing $\cos M = Re(e^{iM}) = Re(e^{-int_0}e^{int})$ and $\sin M = Re(-ie^{-int_0}e^{int})$ we see that it is necessary to evaluate integrals of the form

$$I_\alpha = \int_{-\infty}^{\infty} \frac{e^{int}\sigma^\alpha}{(1+\sigma^2)^6}\dot{\sigma}dt$$

where $\sigma(t)$ is given by eqn(2.12) and $\alpha = 0, 1, 2 \ldots 5$. To make explicit the dependence on σ it is necessary to expand

$$\begin{aligned} \hat{\mathbf{a}}.\mathbf{R} \quad &\text{as} \quad q(1-\sigma^2)\hat{\mathbf{a}}.\hat{\mathbf{A}} + 2q\sigma\hat{\mathbf{a}}.\hat{\mathbf{B}} \\ \hat{\mathbf{a}}.\mathbf{R}' \quad &\text{as} \quad -2q\sigma\hat{\mathbf{a}}.\hat{\mathbf{A}} + 2q\hat{\mathbf{a}}.\hat{\mathbf{B}} \end{aligned}$$

and similarly for $\hat{\mathbf{b}}.\mathbf{R}$ and $\hat{\mathbf{b}}.\mathbf{R}'$.

From eqns(2.12) and (2.10) it is clear that

$$nt = K(\sigma + \frac{1}{3}\sigma^3) \quad \text{where} \quad K = \sqrt{\frac{2M_{12}q^3}{M_{123}a^3}}.$$

The integral, I_α, is then given by

$$I_\alpha = \int_{-\infty}^{\infty} \frac{e^{iK(\sigma+\frac{1}{3}\sigma^3)}\sigma^\alpha}{(1+\sigma^2)^6} d\sigma.$$

Three integrations by parts, bearing in mind that K is very large ($q \gg a$ implies that $K \gg 1$), permits the following approximation :

$$I_\alpha \simeq \frac{(iK)^3}{10.6.2} \int_{-\infty}^{\infty} \sigma^{\alpha-3} e^{iK(\sigma+\frac{1}{3}\sigma^3)} d\sigma.$$

This integral can be evaluated using the method of steepest descents (cf. Heggie 1975). The relevant saddle point is at $\sigma = i$, and if we write $\sigma = i + U$ we find that

$$I_\alpha \simeq \frac{(iK)^3}{120} \int_{-\infty}^{\infty} e^{iKi(\frac{2}{3}+U^2)} i^{\alpha-3} dU.$$

This then yields

$$I_\alpha \simeq \frac{i^\alpha\sqrt{\pi}}{120} K^{\frac{5}{2}} e^{-\frac{2}{3}K} \quad (K \to \infty) \tag{2.17}$$

Substituting eqn(2.15) into eqn(2.7) and using eqn(2.17) gives

$$\begin{aligned}
\delta\varepsilon \simeq\ & -\frac{Gm_1m_2m_3}{M_{12}q^3}\frac{\sqrt{\pi}}{120} K^{\frac{5}{2}} e^{-\frac{2}{3}K} \times \\
& \Big\{ 60\, a^2 e_1 (\sin nt_0 (\hat{\mathbf{a}}.\hat{\mathbf{B}})^2 + 2\cos nt_0 \hat{\mathbf{a}}.\hat{\mathbf{A}}\hat{\mathbf{a}}.\hat{\mathbf{B}} - \sin nt_0 (\hat{\mathbf{a}}.\hat{\mathbf{A}})^2) \\
& + 120\, ab\, e_4 (-\sin nt_0 \hat{\mathbf{b}}.\hat{\mathbf{B}}\, \hat{\mathbf{a}}.\hat{\mathbf{A}} - \sin nt_0 \hat{\mathbf{a}}.\hat{\mathbf{B}}\, \hat{\mathbf{b}}.\hat{\mathbf{A}} \\
& + \cos nt_0 \hat{\mathbf{a}}.\hat{\mathbf{B}}\, \hat{\mathbf{b}}.\hat{\mathbf{B}} - \cos nt_0 \hat{\mathbf{a}}.\hat{\mathbf{A}}\, \hat{\mathbf{b}}.\hat{\mathbf{A}}) \\
& + 60\, b^2 e_2 (\sin nt_0 (\hat{\mathbf{b}}.\hat{\mathbf{A}})^2 - 2\cos nt_0 \hat{\mathbf{b}}.\hat{\mathbf{B}}\, \hat{\mathbf{b}}.\hat{\mathbf{A}} - \sin nt_0 (\hat{\mathbf{b}}.\hat{\mathbf{B}})^2) \Big\}
\end{aligned}$$

(A simple way to arrive at this expression from eqn(2.16) is to replace the denominator in eqn(2.16) by q^6, to replace $\mathbf{R}$ and $\mathbf{R}'$ by their values at the saddle point $\sigma = i$, i.e. $\mathbf{R} = 2q(\hat{\mathbf{A}} + i\hat{\mathbf{B}})$ and $\mathbf{R}' = 2q(-i\hat{\mathbf{A}} + \hat{\mathbf{B}})$, and to multiply by $\frac{\sqrt{\pi}}{120} K^{\frac{5}{2}} e^{-\frac{2K}{3}}$.)

It is convenient to introduce the angles ω, Ω and i to describe the parabolic path of the third body. This is illustrated in fig(2.4). If a frame of reference is

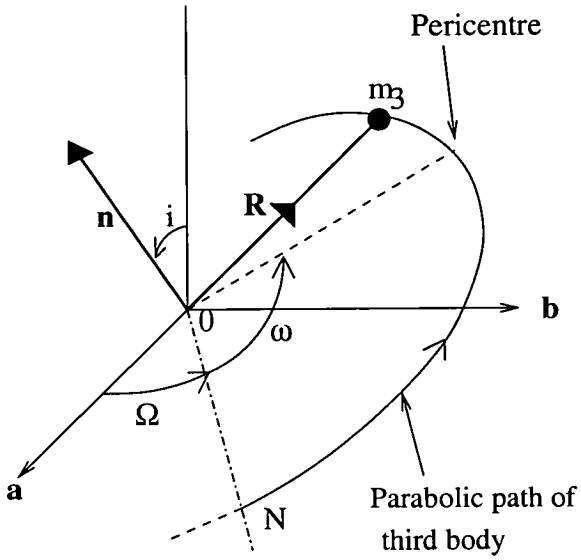

Figure 2.4: The angles describing the orientation of the parabolic orbit. Ω, ω, and i are the longitude of the ascending node, the argument of pericentre and the inclination respectively; ON shows the line in which the plane of motion of the third body intersects the plane of motion of the binary; $\mathbf{n}$ is the vector perpendicular to the plane of motion of the third body.

chosen such that $\hat{\mathbf{a}} = (1,0,0)$ and $\hat{\mathbf{b}} = (0,1,0)$ then (cf. Plummer 1960)

$$\hat{\mathbf{A}} = (\cos\Omega\cos\omega - \cos i\sin\Omega\sin\omega, \sin\Omega\cos\omega + \cos i\cos\Omega\sin\omega, \sin i\sin\omega)$$

$$\hat{\mathbf{B}} = (-\cos\Omega\sin\omega - \cos i\sin\Omega\cos\omega, -\sin\Omega\sin\omega + \cos\omega\cos i\cos\Omega, \sin i\cos\omega). \tag{2.18}$$

Thus

$$\begin{aligned}
\delta\varepsilon \simeq\ & -\frac{Gm_1m_2m_3}{M_{12}q^3}\frac{\sqrt{\pi}}{8}K^{\frac{5}{2}}e^{-\frac{2}{3}K}\Big\{ e_1a^2\Big[\sin(2\omega+nt_0)\ (\cos 2i-1) \\
& -\sin(2\omega+nt_0)\cos(2i)\cos(2\Omega) - 3\sin(nt_0+2\omega)\cos(2\Omega) \\
& -4\sin(2\Omega)\cos(2\omega+nt_0)\cos(i)\Big] \\
& + e_2b^2\Big[\sin(2\omega+nt_0)\ (1-\cos 2i) \\
& -\sin(2\omega+nt_0)\cos(2i)\cos(2\Omega) - 3\sin(nt_0+2\omega)\cos(2\Omega) \\
& -4\cos(nt_0+2\omega)\sin(2\Omega)\cos i\Big] \\
& + e_4\,ab\Big[-2\cos(2i)\cos(2\omega+nt_0)\sin(2\Omega)
\end{aligned}$$

$$-6\cos(2\omega + nt_0)\sin(2\Omega)$$
$$-8\cos(2\Omega)\sin(2\omega + nt_0)\cos i \Big] \Big\}. \qquad (2.19)$$

In the coplanar case when $i = 0$, eqn(2.19) reduces to :

$$\delta\varepsilon \simeq \frac{Gm_1m_2m_3}{M_{12}q^3}\frac{\sqrt{\pi}}{2}K^{\frac{5}{2}}e^{-\frac{2K}{3}}(e_1a^2 + 2e_4ab + e_2b^2)\sin(2\omega + 2\Omega + nt_0).$$

Notice that Ω and ω only appear in the combination $\Omega+\omega$, which is the longitude of pericentre.

The following comments may be made about eqn(2.19):

(i) The exponential term involves the ratio of the mean motion of the third body to the mean motion of the binary. This is characteristic of the behaviour of adiabatic invariants (cf. Goldstein 1980).

(ii) The influence of higher frequency terms such as $\sin 2M$ and $\cos 2M$ has been neglected. These give exponentials which decay even more rapidly with increasing q (i.e. increasing K).

(iii) The derivation of exponentially small terms lacks rigour, because many terms in the expansion, which formally could dominate the exponential result, have been neglected. Our justification for this is based on analogous problems where the results can be justified rigorously (cf. Goldstein).

2.3.2 Comparison with numerical results

Eqn(2.19) has been tested against the results obtained from numerical experiments. We assume that $m_1 = m_2 = m_3 = 1$ and that $a = 1$ initially. The numerical procedure uses units such that $G = 1$. Various input parameters are required before the initial conditions of the bodies may be assigned.

A frame of reference is chosen which is centred (initially) on the barycentre of m_1 and m_2. At the start of the simulation the third body, m_3, is assumed to lie at a suitably large distance, R_{init} (say), from the origin so that its influence on the binary is insignificant. In addition to R_{init} the program takes, as input parameters, the angle of inclination, i, of the plane of motion of the third body and its periastron distance, q. Taking the longitude of the ascending node,

$\Omega = 0$, the program then computes suitable initial conditions for m_3 so that its motion follows the parabolic orbit specified by the input parameters.

The other input parameters relate to bodies m_1 and m_2 which form the binary system. When $R = R_{init}$ the program requires the user to specify the eccentric anomaly, E_{init} of either m_1 or m_2. This will fix the phase of the binary. The only remaining input parameter is the eccentricity, e_{init}. The program then assigns suitable initial conditions to m_1 and m_2.

The program then numerically integrates the motion of the system until the distance of the third body from the barycentre of the binary exceeds R_{init}. When this condition is satisfied the binary is approximated by a new Keplerian orbit a' (say). The energy change is then given by $(1/2) - (1/a')$. The program also computes the argument of pericentre, ω and the mean anomaly of the binary, nt_0 when the third body is at pericentre. These quantities are required so that the theoretical formula may be applied.

The results shown in fig(2.4) show the change in energy as a function of the initial phase, E_{init}, of the binary for various inclinations. Fig(2.5) shows how the energy change is related to the periastron distance q.

2.4 Binaries with circular orbits

Circular binaries are particularly important since they occur frequently in globular clusters. The foregoing theory fails in this special case and a full rederivation is given as follows.

2.4.1 Circular Orbits/Non-equal masses

In order to find the dominant contribution to the energy we are forced to look at the third term in the expansion of the perturbing function $\mathcal{R}$ in eqn(2.4). (We shall see in sec(2.4.2) that the second term in the expansion of the perturbing function gives a less significant contribution due to integrations involving $\sin 2M$, $\cos 2M$.) This term is given by

$$-\frac{r^3}{R^4}\frac{1}{2}\left[\, 5(\frac{\mathbf{r}.\mathbf{R}}{rR})^3 - 3(\frac{\mathbf{r}.\mathbf{R}}{rR}) \,\right](\mu_2 - \mu_1).$$

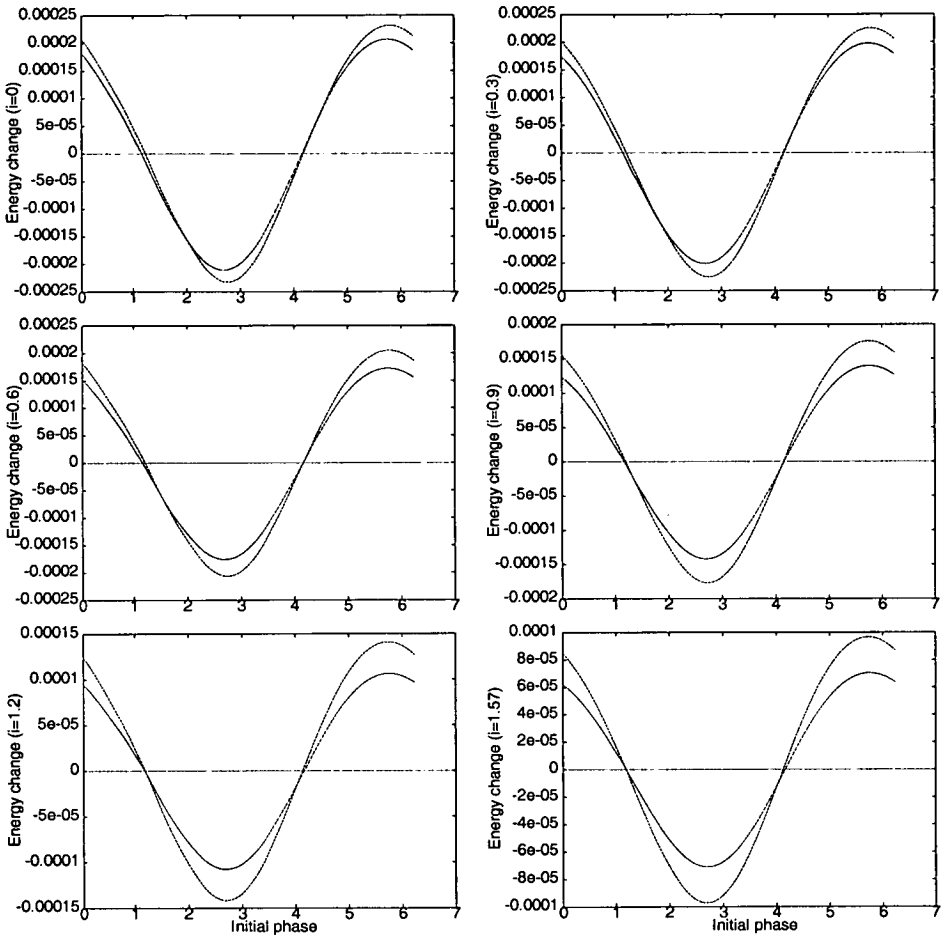

Figure 2.5: This shows $\delta\varepsilon$ against the initial phase of the binary for various angles of inclination. For each value of i a comparison is made between the numerical results (green) and the theoretical prediction (blue) obtained from eqn(2.19); $R_{init} = 80$, $e_{init} = 0.1$, $q = 5$.

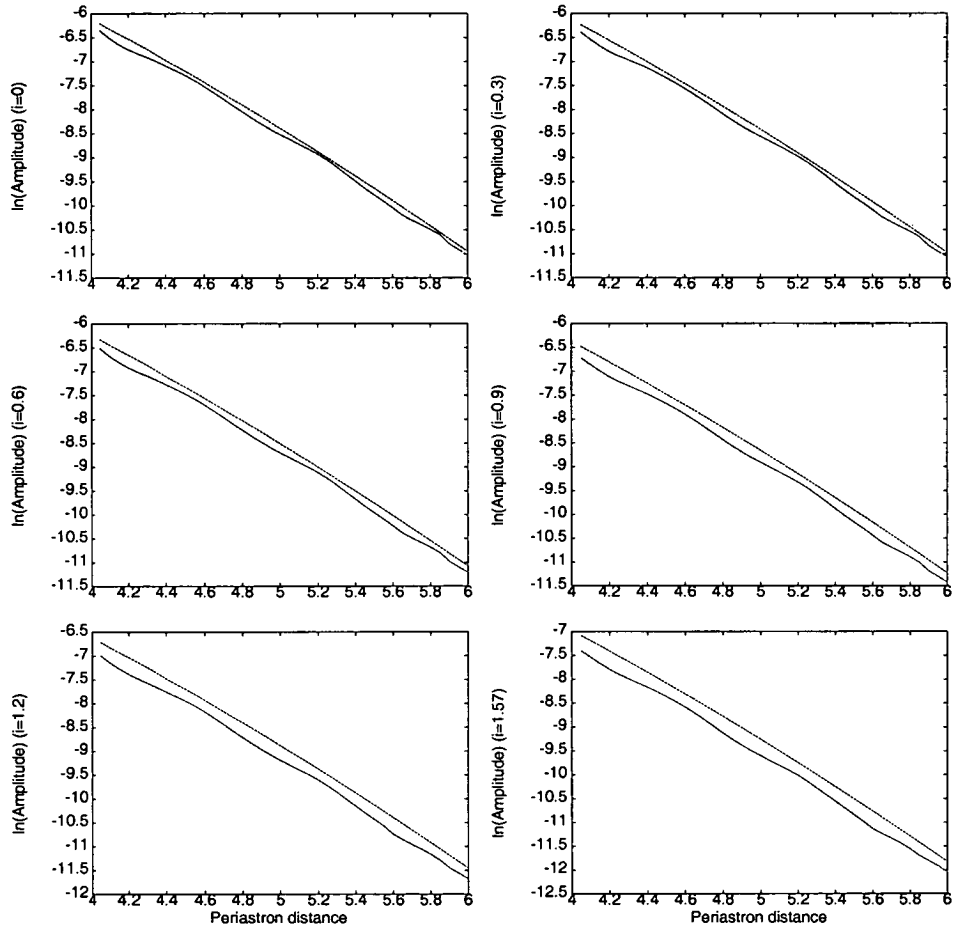

Figure 2.6: This shows the natural log of the amplitude of the change in energy $\delta\varepsilon$ against the periastron distance, q, for various angles of inclination. The numerical results (green) are obtained for $e_{init} = 0.1$ and $R_{init} = 80$.

For a circular orbit the eccentricity $e = 0$ and the expression for $\mathbf{r}$ is given by

$$\mathbf{r} = a\cos E\ \hat{\mathbf{a}} + a\sin E\ \hat{\mathbf{b}}$$

where $E = M$. Substituting this into the expression for $\mathcal{R}$ gives

$$\begin{aligned}\mathcal{R} &= \frac{a^3}{2R^4}\Bigg[\ \frac{5}{R^3}\Bigg(\cos^3 E(\hat{\mathbf{a}}.\mathbf{R})^3 + 3\cos^2 E\sin E(\hat{\mathbf{a}}.\mathbf{R})^2(\hat{\mathbf{b}}.\mathbf{R}) \\ &\quad +3\sin^2 E\cos E(\hat{\mathbf{a}}.\mathbf{R})(\hat{\mathbf{b}}.\mathbf{R})^2 + \sin^3 E(\hat{\mathbf{b}}.\mathbf{R})^3\ \Bigg) \\ &\quad -\frac{3}{R}(\cos E(\hat{\mathbf{a}}.\mathbf{R}) + \sin E(\hat{\mathbf{b}}.\mathbf{R}))\ \Bigg](\mu_2 - \mu_1).\end{aligned}$$

The following trigonometric identities are used to simplify the expression :

$$\begin{aligned}\cos^3 E &= \frac{3}{4}\cos E + \frac{1}{4}\cos 3E; \quad \sin^3 E = \frac{3}{4}\sin E - \frac{1}{4}\sin 3E \\ \cos^2 E\sin E &= \frac{1}{4}\sin E + \frac{1}{4}\sin 3E; \quad \sin^2 E\cos E = \frac{1}{4}\cos E - \frac{1}{4}\cos 3E.\end{aligned}$$

This gives

$$\begin{aligned}\mathcal{R} &= \Bigg[\Bigg(\frac{15a^3(\hat{\mathbf{a}}.\mathbf{R})^3}{8R^7} + \frac{15a^3(\hat{\mathbf{a}}.\mathbf{R})(\hat{\mathbf{b}}.\mathbf{R})^2}{8R^7} - \frac{3a^3(\hat{\mathbf{a}}.\mathbf{R})}{2R^5}\Bigg)\cos E \\ &\quad + \Bigg(\frac{15a^3(\hat{\mathbf{a}}.\mathbf{R})^2(\hat{\mathbf{b}}.\mathbf{R})}{8R^7} + \frac{15a^3(\hat{\mathbf{b}}.\mathbf{R})^3}{8R^7} - \frac{3a^3(\hat{\mathbf{b}}.\mathbf{R})}{2R^5}\Bigg)\sin E\ \Bigg](\mu_2 - \mu_1) \\ &\quad + \text{terms of higher frequency.}\end{aligned} \tag{2.20}$$

The first integral is evaluated asymptotically by applying eqn(A.8) in the Appendix:

$$\int_{-\infty}^{\infty}\dot{\mathbf{R}}.\frac{\partial}{\partial\mathbf{R}}\left(\frac{15a^3(\hat{\mathbf{a}}.\mathbf{R})^3\cos E}{8R^7}\right)dt = -\frac{15a^3}{8q^4}\frac{\sqrt{\pi}}{120}K^{\frac{7}{2}}e^{-\frac{2}{3}K}\times \tag{2.21}$$

$$\Big(\ 8(\hat{\mathbf{a}}.\hat{\mathbf{A}})^3\sin nt_0 - 24(\hat{\mathbf{a}}.\hat{\mathbf{A}})^2(\hat{\mathbf{a}}.\hat{\mathbf{B}})\cos nt_0 - 24\sin nt_0(\hat{\mathbf{a}}.\hat{\mathbf{A}})(\hat{\mathbf{a}}.\hat{\mathbf{B}})^2 + 8\cos nt_0(\hat{\mathbf{a}}.\hat{\mathbf{B}})^3\ \Big).$$

The next integral is obtained by applying eqn(A.12) :

$$\int_{-\infty}^{\infty}\dot{\mathbf{R}}.\frac{\partial}{\partial\mathbf{R}}\left(\frac{15a^3(\hat{\mathbf{a}}.\mathbf{R})(\hat{\mathbf{b}}.\mathbf{R})^2\cos E}{8R^7}\right)dt = \frac{-a^3}{8q^4}\sqrt{\pi}K^{\frac{7}{2}}e^{-\frac{2K}{3}}\times \tag{2.22}$$

$$\begin{aligned}&\Big(\ \sin nt_0(\hat{\mathbf{a}}.\hat{\mathbf{A}})(\hat{\mathbf{b}}.\hat{\mathbf{A}})^2 - 2\cos nt_0(\hat{\mathbf{a}}.\hat{\mathbf{A}})(\hat{\mathbf{b}}.\hat{\mathbf{A}})(\hat{\mathbf{b}}.\hat{\mathbf{B}}) - \cos nt_0(\hat{\mathbf{a}}.\hat{\mathbf{B}})(\hat{\mathbf{b}}.\hat{\mathbf{A}})^2 \\ &-2\sin nt_0(\hat{\mathbf{a}}.\hat{\mathbf{B}})(\hat{\mathbf{b}}.\hat{\mathbf{A}})(\hat{\mathbf{b}}.\hat{\mathbf{B}}) - \sin nt_0(\hat{\mathbf{a}}.\hat{\mathbf{A}})(\hat{\mathbf{b}}.\hat{\mathbf{B}})^2 + \cos nt_0(\hat{\mathbf{b}}.\hat{\mathbf{B}})^2(\hat{\mathbf{a}}.\hat{\mathbf{B}})\ \Big)\end{aligned}$$

By eqn(A.1), where the distinction between E and M is immaterial, the integral

$$\int_{-\infty}^{\infty} \dot{\mathbf{R}}.\frac{\partial}{\partial \mathbf{R}}\left(\frac{-3a^3(\hat{\mathbf{a}}.\mathbf{R})\cos E}{2R^5}\right) dt = \frac{-a^3\sqrt{\pi}}{4q^4} K^{\frac{5}{2}} e^{-\frac{2K}{3}} \times$$

$$(-\sin nt_0(\hat{\mathbf{a}}.\hat{\mathbf{A}}) + \cos nt_0(\hat{\mathbf{a}}.\hat{\mathbf{B}})). \tag{2.23}$$

Notice that this is one order smaller in K, and will be neglected.

The contribution from the terms $\sim \sin E$ is given as follows. ¿From eqn(A.11) it is found that

$$\int_{-\infty}^{\infty} \frac{15a^3}{8}\dot{\mathbf{R}}.\frac{\partial}{\partial \mathbf{R}}\left(\frac{(\hat{\mathbf{b}}.\mathbf{R})^3}{R^7}\right)\sin E\, dt = \frac{-a^3}{q^4}\frac{\sqrt{\pi}}{8} K^{\frac{7}{2}} e^{-\frac{2K}{3}} \times \tag{2.24}$$

$$\left(\cos nt_0(\hat{\mathbf{b}}.\hat{\mathbf{A}})^3 + 3\sin nt_0(\hat{\mathbf{b}}.\hat{\mathbf{A}})^2(\hat{\mathbf{b}}.\hat{\mathbf{B}}) - 3\cos nt_0(\hat{\mathbf{b}}.\hat{\mathbf{A}})(\hat{\mathbf{b}}.\hat{\mathbf{B}})^2 - \sin nt_0(\hat{\mathbf{b}}.\hat{\mathbf{B}})^3\right).$$

¿From eqn(A.13) the integral

$$\int_{-\infty}^{\infty} \frac{15a^3}{8}\dot{\mathbf{R}}.\frac{\partial}{\partial \mathbf{R}}\left(\frac{(\hat{\mathbf{a}}.\mathbf{R})^2(\hat{\mathbf{b}}.\mathbf{R})}{R^7}\right)\sin E dt = \frac{-a^3}{8q^4}\sqrt{\pi} K^{\frac{7}{2}} e^{-\frac{2K}{3}} \times \tag{2.25}$$

$$\left(\cos nt_0(\hat{\mathbf{b}}.\hat{\mathbf{A}})(\hat{\mathbf{a}}.\hat{\mathbf{A}})^2 + 2\sin nt_0(\hat{\mathbf{b}}.\hat{\mathbf{A}})(\hat{\mathbf{a}}.\hat{\mathbf{A}})(\hat{\mathbf{a}}.\hat{\mathbf{B}}) + \sin nt_0(\hat{\mathbf{b}}.\hat{\mathbf{B}})(\hat{\mathbf{a}}.\hat{\mathbf{A}})^2\right.$$

$$\left. -2\cos nt_0(\hat{\mathbf{b}}.\hat{\mathbf{B}})(\hat{\mathbf{a}}.\hat{\mathbf{A}})(\hat{\mathbf{a}}.\hat{\mathbf{B}}) - \cos nt_0(\hat{\mathbf{b}}.\hat{\mathbf{A}})(\hat{\mathbf{a}}.\hat{\mathbf{B}})^2 - \sin nt_0(\hat{\mathbf{a}}.\hat{\mathbf{B}})^2(\hat{\mathbf{b}}.\hat{\mathbf{B}})\right).$$

Applying eqn(A.4) the integral

$$\int_{-\infty}^{\infty} \dot{\mathbf{R}}.\frac{\partial}{\partial \mathbf{R}}\left(\frac{-3a^3(\hat{\mathbf{b}}.\mathbf{R})\sin E}{2R^5}\right) dt$$

is of lower order in K. The faster oscillating terms $\sim \sin 3E, \cos 3E$ may be ignored since they their contribution to the energy change is exponentially small. This means that $\delta\varepsilon$ is given by (combining the results for eqns(2.21), (2.22), (2.24) and (2.25))

$$\delta\varepsilon \simeq \frac{Gm_1m_2m_3}{M_{12}}\frac{\sqrt{\pi}a^3}{8q^4} K^{\frac{7}{2}} e^{-\frac{2K}{3}}(\mu_2 - \mu_1)\left[\sin nt_0(\hat{\mathbf{a}}.\hat{\mathbf{A}})^3\right.$$

$$-3\cos nt_0(\hat{\mathbf{a}}.\hat{\mathbf{A}})^2(\hat{\mathbf{a}}.\hat{\mathbf{B}}) - 3\sin nt_0(\hat{\mathbf{a}}.\hat{\mathbf{A}})(\hat{\mathbf{a}}.\hat{\mathbf{B}})^2 + \cos nt_0(\hat{\mathbf{a}}.\hat{\mathbf{B}})^3$$

$$+\sin nt_0(\hat{\mathbf{a}}.\hat{\mathbf{A}})(\hat{\mathbf{b}}.\hat{\mathbf{A}})^2 - 2\cos nt_0(\hat{\mathbf{a}}.\hat{\mathbf{A}})(\hat{\mathbf{b}}.\hat{\mathbf{A}})(\hat{\mathbf{b}}.\hat{\mathbf{B}}) - \cos nt_0(\hat{\mathbf{a}}.\hat{\mathbf{B}})(\hat{\mathbf{b}}.\hat{\mathbf{A}})^2$$

$$-2\sin nt_0(\hat{\mathbf{a}}.\hat{\mathbf{B}})(\hat{\mathbf{b}}.\hat{\mathbf{A}})(\hat{\mathbf{b}}.\hat{\mathbf{B}}) - \sin nt_0(\hat{\mathbf{a}}.\hat{\mathbf{A}})(\hat{\mathbf{b}}.\hat{\mathbf{B}})^2 + \cos nt_0(\hat{\mathbf{b}}.\hat{\mathbf{B}})^2(\hat{\mathbf{a}}.\hat{\mathbf{B}})$$

$$\left.+\cos nt_0(\hat{\mathbf{b}}.\hat{\mathbf{A}})^3 + 3\sin nt_0(\hat{\mathbf{b}}.\hat{\mathbf{A}})^2(\hat{\mathbf{b}}.\hat{\mathbf{B}}) - 3\cos nt_0(\hat{\mathbf{b}}.\hat{\mathbf{A}})(\hat{\mathbf{b}}.\hat{\mathbf{B}})^2\right.$$

$$-\sin nt_0(\hat{\mathbf{b}}.\hat{\mathbf{B}})^3+\cos nt_0(\hat{\mathbf{b}}.\hat{\mathbf{A}})(\hat{\mathbf{a}}.\hat{\mathbf{A}})^2+2\sin nt_0(\hat{\mathbf{b}}.\hat{\mathbf{A}})(\hat{\mathbf{a}}.\hat{\mathbf{A}})(\hat{\mathbf{a}}.\hat{\mathbf{B}})$$
$$+\sin nt_0(\hat{\mathbf{b}}.\hat{\mathbf{B}})(\hat{\mathbf{a}}.\hat{\mathbf{A}})^2-2\cos nt_0(\hat{\mathbf{b}}.\hat{\mathbf{B}})(\hat{\mathbf{a}}.\hat{\mathbf{A}})(\hat{\mathbf{a}}.\hat{\mathbf{B}})-\cos nt_0(\hat{\mathbf{b}}.\hat{\mathbf{A}})(\hat{\mathbf{a}}.\hat{\mathbf{B}})^2$$
$$-\sin nt_0(\hat{\mathbf{a}}.\hat{\mathbf{B}})^2(\hat{\mathbf{b}}.\hat{\mathbf{B}})\Big]$$

with an error smaller by a factor of order $\frac{1}{K}$.

We choose axes such that the longitude of the ascending node of the orbit of the third body, relative to the plane of motion of the binary, is $\Omega = 0$. Since the binary is initially circular we may also take $\hat{\mathbf{a}}, \hat{\mathbf{b}}$ anywhere in its plane of motion, and therefore take

$$\hat{\mathbf{a}} = (1,0,0) \qquad \hat{\mathbf{b}} = (0,1,0)$$
$$\hat{\mathbf{A}} = (\cos\omega, \cos i\sin\omega, \sin i\sin\omega) \quad \hat{\mathbf{B}} = (-\sin\omega, \cos i\cos\omega, \sin i\cos\omega).$$

This means that

$$(\hat{\mathbf{a}}.\hat{\mathbf{A}}) = \cos\omega \qquad (\hat{\mathbf{a}}.\hat{\mathbf{B}}) = -\sin\omega$$
$$(\hat{\mathbf{b}}.\hat{\mathbf{A}}) = \cos i\sin\omega \quad (\hat{\mathbf{b}}.\hat{\mathbf{B}}) = \cos i\cos\omega.$$

The expression for $\delta\varepsilon$ may be simplified to give

$$\delta\varepsilon \simeq \frac{Gm_1m_2m_3}{M_{12}}\frac{\sqrt{\pi}a^3}{8q^4}K^{\frac{7}{2}}e^{-\frac{2K}{3}}(\mu_2-\mu_1)(1+\cos i)\sin^2 i \;\times$$
$$\Big[(\cos^3\omega - 3\sin^2\omega\cos\omega)\sin nt_0 + (3\cos^2\omega\sin\omega - \sin^3\omega)\cos nt_0\Big].$$

2.4.2 Circular orbits/equal masses

Unfortunately, the theory must be rederived in the case when the masses of the components of the binary are equal ($\mu_1 = \mu_2$). As before, lowest order perturbation theory is used and in the case of a circular binary $E = M$ from eqn(2.10). Then all the "odd" terms in the expansion of eqn(2.4) vanish, i.e. those with factors $\frac{1}{R}(\frac{r}{R})^n$ with n odd. The dominant contribution is obtained when $n = 2$ from terms in $\cos 2M$ and $\sin 2M$. This is because all the terms involving $\sin M$ and $\cos M$ in the expansion of eqn(2.13) disappear when $e = 0$. In performing the integral in eqn(2.7) integrals of the following form require to be evaluated:

$$I_\alpha = \int_{-\infty}^{\infty}\frac{e^{2iK(\sigma+\frac{1}{3}\sigma^3)}\sigma^\alpha}{(1+\sigma^2)^6}d\sigma$$

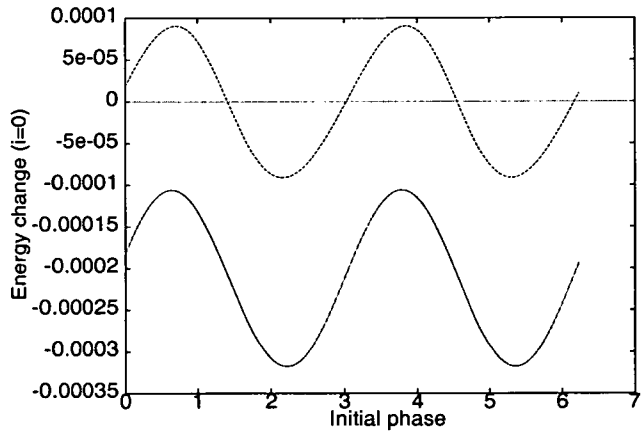

Figure 2.7: The numerical results (green) compared with the analytical theory (blue) in eqn(2.27) when the binary motion is circular ($q = 4$).

where α=0,1,2...5.

By the methods of sec(2.3.1) it is found that

$$\begin{aligned} I_\alpha &\simeq \frac{(2iK)^3}{10.6.2} e^{-\frac{4}{3}K} \sqrt{\frac{\pi}{2K}}\, i^{\alpha-3} \\ &= \frac{i^\alpha}{15}\sqrt{\frac{\pi}{2}} e^{-\frac{4}{3}K} K^{\frac{5}{2}} \quad (K \to \infty). \end{aligned}$$

Hence, using eqns(2.18)

$$\delta\varepsilon \simeq \frac{8Gm_1m_2m_3\sqrt{2\pi}}{aM_{123}} e^{-\frac{4}{3}K} K^{\frac{1}{2}} \sin(2\omega + 2\Omega + 2nt_0) \cos^4\frac{i}{2}. \tag{2.26}$$

2.4.3 Comparison with numerical results

Eqn(2.26) has been tested numerically in the case when $i = 0$, when the energy change is given by

$$\delta\varepsilon \simeq \frac{Gm_1m_2m_3}{M_{12}} \frac{8a^2}{q^3} \sqrt{\frac{\pi}{2}} e^{-\frac{4K}{3}} K^{\frac{5}{2}} \sin\left(2nt_0 + 2\Omega + 2\omega\right). \tag{2.27}$$

The same numerical procedure is used as before in sec(2.3.2) but in this case $e_{init} = 0$ since the binary is initially circular. Fig(2.7) compares the numerical results with the analytical theory in eqn(2.27). The sinusoidal component of eqn(2.27) is in phase with the numerical results and has nearly the correct amplitude but it fails to account for the non-zero mean which is observed.

2.4.4 Second order perturbation calculation

We show in this section that the non-zero mean can be explained in terms of second order perturbation theory, at least in the coplanar case. (A similar non-zero mean arises in the noncoplanar case but the following theory is restricted to the case $i = 0$ for simplicity.) The following argument explains why this might be expected.

We have already seen, by comparing eqn(2.19) and eqn(2.26), that the change of energy in an eccentric binary is much greater than in a circular binary, in the sense that $e^{-\frac{2K}{3}} \gg e^{-\frac{4K}{3}}$ for $K \gg 1$. But these results are based on 1st order perturbation theory. At second order we have to allow for the fact that the passing star induces a tiny eccentricity on the binary. This may induce a much larger mean energy change than was obtained from 1st order theory.

The Hamiltonian for the binary is a periodic function of the mean anomaly of the binary and is given by

$$\mathcal{H} = \frac{p^2}{2\frac{m_1 m_2}{M_{12}}} - \frac{G m_1 m_2}{r} + H'$$

where

$$\mathbf{p} = \left(\frac{m_1 m_2}{m_1 + m_2}\right)\dot{\mathbf{r}}$$

and

$$H' = -\frac{G m_1 m_2 m_3}{M_{12}}\mathcal{R}.$$

In place of $\mathbf{p}$ and $\mathbf{r}$ the Hamiltonian may be expressed in terms of a set of orbital elements which are particularly useful for describing elliptic motion. These elements, known as *Delaunay's variables*, are defined as follows (cf. Plummer 1960):

$$\begin{aligned} L &= m\sqrt{G(m_1 + m_2)a} & l &= nt + M_0 \\ G &= m\sqrt{G(m_1 + m_2)a(1 - e^2)} & g &= \omega \\ H &= m\sqrt{G(m_1 + m_2)a(1 - e^2)}\cos i & h &= \Omega \end{aligned} \tag{2.28}$$

where

$$m = \frac{m_1 m_2}{m_1 + m_2}.$$

In fact they are a set of action-angle variables for the Kepler problem. We concentrate attention on the Delaunay variable, L, which is directly related to the energy of the binary. Its conjugate variable l is the only "fast" variable in the problem. In the coplanar problem (since we are examining the case $i = 0$) the Delaunay variables H and h may be ignored. Without changing L, the variables $(L,\ G\ ;l,\ g)$ may be transformed to a new set $(L,\ \rho_1\ ;\lambda,\ \omega_1)$ where

$$\rho_1 = L - G, \qquad \omega_1 = -g, \qquad \lambda = l + g.$$

These are still canonical, L and ρ_1 being conjugate to λ and ω_1 respectively. Since g is ill-defined when e becomes very small, it is better to use the eccentric variables x, y instead of ρ_1 and ω_1. The eccentric variables are particularly well-suited to the study of motions with small eccentricity. Both the eccentric and Delaunay variables are useful in celestial mechanics because they form a set of canonical variables which incorporate the orbital elements of the binary. The canonical momenta have physical meaning: L is associated with the energy of the binary and G gives the angular momentum; l is the mean motion and g gives the argument of pericentre. The eccentric variables are related to the Delaunay variables by

$$x = \sqrt{2\rho_1}\cos\omega_1 \simeq \sqrt{L}e\cos g, \qquad y = -\sqrt{2\rho_1}\sin\omega_1 \simeq \sqrt{L}e\sin g$$

and, being canonical, they satisfy

$$\dot{x} = \frac{\partial H'}{\partial y}, \qquad \dot{y} = -\frac{\partial H'}{\partial x}. \tag{2.29}$$

H' is then a periodic function of the mean longitude, λ, and may be expanded as follows

$$H' = \sum_{k=-\infty}^{\infty} c_k(L, x, y)e^{ik\lambda}$$

where x and y are the eccentric variables.

To explain the non-zero mean a contribution to the energy change is sought which is independent of the phase. This is the only result we shall seek. Roughly speaking, this contribution is found (in second-order perturbation theory) by combining the terms in $\delta\varepsilon$ corresponding to the coefficients c_{-1} and c_1 in the

expansion of H', so that the oscillatory components cancel. Because the calculation is complicated enough, and because it is narrowly focussed on a single result, we retain only the most significant relevant terms and ignore those which contribute only oscillatory corrections and those which are of relatively negligible order in the small expansion parameters r/R (equivalently, K^{-1}) and e.

¿From eqn(2.29)

$$\dot{x} \simeq \frac{\partial c_{-1}}{\partial y} e^{-i\lambda} + \frac{\partial c_1}{\partial y} e^{i\lambda} \quad \text{and} \quad \dot{y} \simeq -\frac{\partial c_{-1}}{\partial x} e^{-i\lambda} - \frac{\partial c_1}{\partial x} e^{i\lambda},$$

the approximate equality implying that we ignore all irrelevant terms. Using first order perturbation theory (cf. Goldstein 1980, Born 1960)

$$x_1 \simeq \int_{-\infty}^{t} \frac{\partial c_{-1}}{\partial y} e^{-i\lambda_0} dt + \int_{-\infty}^{t} \frac{\partial c_1}{\partial y} e^{i\lambda_0} dt$$

and

$$y_1 \simeq -\int_{-\infty}^{t} \frac{\partial c_{-1}}{\partial x} e^{-i\lambda_0} dt - \int_{-\infty}^{t} \frac{\partial c_1}{\partial x} e^{i\lambda_0} dt \tag{2.30}$$

where subscripts 0 and 1 denote terms at zeroth and first order in a perturbation expansion and the partial derivatives

$$\frac{\partial c_{-1}}{\partial y}, \quad \frac{\partial c_1}{\partial y}, \quad \frac{\partial c_{-1}}{\partial x}, \quad \frac{\partial c_1}{\partial x}$$

are evaluated for the unperturbed motion $L = L_0, \quad x = x_0 = 0, \quad y = y_0 = 0.$

The rate of change of L to second order is,

$$\dot{L}_2 = -\frac{\partial H'}{\partial \lambda}$$

where the partial derivative is evaluated at

$$L = L_0 + L_1 \quad \lambda = \lambda_0 + \lambda_1$$
$$x = x_0 + x_1 \quad y = y_0 + y_1.$$

This gives

$$\begin{aligned} \dot{L}_2 &= \sum_{k=\pm 1} -ikc_k(L_0 + L_1, x_0 + x_1, y_0 + y_1) e^{ik(\lambda_0 + \lambda_1)} \\ &= \sum_{k=\pm 1} -ikc_k(L_0, x_0, y_0) e^{ik\lambda_0} - \sum_{k=\pm 1} ik(L_1 \frac{\partial c_k}{\partial L} + ik\lambda_1 c_k) e^{ik\lambda_0} \\ &\quad + \sum_{k=\pm 1} -ik(x_1 \frac{\partial c_k}{\partial x} + y_1 \frac{\partial c_k}{\partial y}) e^{ik\lambda_0}. \end{aligned} \tag{2.31}$$

The partial derivatives in eqn(2.31) are evaluated at the zero order solution. On integrating the first term, the first order contribution to L and hence the first order approximation for the change in energy of the binary is obtained. This has been previously calculated in eqn(2.26). We shall see that the second term vanishes. Finally, integration of the last term leads to a phase independent contribution which is calculated as follows.

$$\begin{aligned}
\dot{L}_2 &\simeq \sum_{k=\pm 1} -ik(x_1\frac{\partial c_k}{\partial x} + y_1\frac{\partial c_k}{\partial y})e^{ik\lambda_0} \\
&= i(x_1\frac{\partial c_{-1}}{\partial x} + y_1\frac{\partial c_{-1}}{\partial y})e^{-i\lambda_0} - i(x_1\frac{\partial c_1}{\partial x} + y_1\frac{\partial c_1}{\partial y})e^{i\lambda_0} (\text{by eqn(2.30)}) \\
&= i\left(\frac{\partial c_{-1}}{\partial x}e^{-i\lambda_0}\int_{-\infty}^{t}\frac{\partial c_1}{\partial y}e^{i\lambda_0}dt - e^{-i\lambda_0}\frac{\partial c_{-1}}{\partial y}\int_{-\infty}^{t}\frac{\partial c_1}{\partial x}e^{i\lambda_0}dt\right) \\
&\quad -i\left(\frac{\partial c_1}{\partial x}e^{i\lambda_0}\int_{-\infty}^{t}\frac{\partial c_{-1}}{\partial y}e^{-i\lambda_0}dt - e^{i\lambda_0}\frac{\partial c_1}{\partial y}\int_{-\infty}^{t}\frac{\partial c_{-1}}{\partial x}e^{-i\lambda_0}dt\right) \\
&= i\frac{\partial}{\partial t}\left(\int_{-\infty}^{t}\frac{\partial c_{-1}}{\partial x}e^{-i\lambda_0}dt\int_{-\infty}^{t}\frac{\partial c_1}{\partial y}e^{i\lambda_0}dt\right. \\
&\qquad \left. - \int_{-\infty}^{t}e^{-i\lambda_0}\frac{\partial c_{-1}}{\partial y}dt\int_{-\infty}^{t}\frac{\partial c_1}{\partial x}e^{i\lambda_0}dt\right),
\end{aligned}$$

retaining phase independent terms only. This implies that, at the end of the encounter,

$$\begin{aligned}
L_2 &= i\left(\int_{-\infty}^{\infty}\frac{\partial c_{-1}}{\partial x}e^{-i\lambda_0}dt\int_{-\infty}^{\infty}\frac{\partial c_1}{\partial y}e^{i\lambda_0}dt\right. \\
&\qquad \left. - \int_{-\infty}^{\infty}e^{-i\lambda_0}\frac{\partial c_{-1}}{\partial y}dt\int_{-\infty}^{\infty}\frac{\partial c_1}{\partial x}e^{i\lambda_0}dt\right). \qquad (2.32)
\end{aligned}$$

In the coplanar case the perturbing Hamiltonian is given in terms of the Legendre polynomial P_2 (cf. eqn.2.4). In terms of $\mathcal{R}$, an explicit expression is given in eqn(2.13) but it must be transformed to the new variables. Suppose that $\hat{\mathbf{a}}$ and $\hat{\mathbf{b}}$ are orthogonal unit vectors fixed in an inertial frame and in the plane of the binary. If g is measured with respect to this frame and $\hat{\mathbf{x}}_1$, $\hat{\mathbf{y}}_1$ are orthogonal unit vectors in the direction of the major and minor axes of the relative orbit then

$$\hat{\mathbf{x}}_1 = \cos g\ \hat{\mathbf{a}} + \sin g\ \hat{\mathbf{b}}, \quad \hat{\mathbf{x}}_2 = -\sin g\ \hat{\mathbf{a}} + \cos g\ \hat{\mathbf{b}}.$$

Then we expand eqn(2.9) to first order in e noting that $l = M$. From the relation between H, and $\mathcal{R}$ it is eventually found that, to first order in e,

$$H' = \frac{-G_1 m_1 m_2 m_3}{M_{12} R^5} \left\{ \frac{3}{2} \left(a \left[\cos\lambda - \frac{3}{2}\frac{x}{\sqrt{L}} + \frac{1}{2}\cos 2\lambda(\frac{x}{\sqrt{L}}) + \frac{1}{2}\sin 2\lambda(\frac{y}{\sqrt{L}}) \right] \hat{\mathbf{a}}.\mathbf{R} \right.\right.$$
$$\left. + a \left[\sin\lambda + \frac{1}{2}\sin 2\lambda(\frac{x}{\sqrt{L}}) - \frac{1}{2}\cos 2\lambda(\frac{y}{\sqrt{L}}) - \frac{3}{2}\frac{y}{\sqrt{L}} \right] \hat{\mathbf{b}}.\mathbf{R} \right)^2$$
$$\left. - \frac{1}{2}\frac{a^2}{R^3} \left(1 - \cos\lambda(\frac{x}{\sqrt{L}}) - \sin\lambda(\frac{y}{\sqrt{L}}) \right)^2 \right\}.$$

This may be expanded to lowest order in x, y to give

$$H' = -\frac{G m_1 m_2 m_3}{M_{12}} \left(\left[\frac{-15a^2}{4R^5}\frac{x}{\sqrt{L}}(\hat{\mathbf{a}}.\mathbf{R})^2 - \frac{9a^2}{2R^5}\frac{y}{\sqrt{L}}(\hat{\mathbf{a}}.\mathbf{R})(\hat{\mathbf{b}}.\mathbf{R}) \right.\right.$$
$$\left. + \frac{3a^2 x}{4\sqrt{L}R^5}(\hat{\mathbf{b}}.\mathbf{R})^2 + \frac{a^2 x}{\sqrt{L}R^3} \right] \cos\lambda$$
$$\left. + \left[\frac{3a^2 y}{4\sqrt{L}R^5}(\hat{\mathbf{a}}.\mathbf{R})^2 - \frac{9a^2 x}{2\sqrt{L}R^5}(\hat{\mathbf{a}}.\mathbf{R})(\hat{\mathbf{b}}.\mathbf{R}) - \frac{15a^2 y}{4\sqrt{L}R^5}(\hat{\mathbf{b}}.\mathbf{R})^2 + \frac{a^2 y}{\sqrt{L}R^3} \right] \sin\lambda \right)$$

where we have retained only the terms in $\sin\lambda$ and $\cos\lambda$.

Let us denote the coefficients of $\cos\lambda$ and $\sin\lambda$ by a_1 and b_1. The complex coefficients c_1, c_{-1} are then given by

$$c_1 = \frac{1}{2}(a_1 - ib_1), \qquad c_{-1} = \frac{1}{2}(a_1 + ib_1).$$

Since the orbit of the binary system is assumed to be initially circular the zero order solution may be written as

$$x = x_0 = 0; \quad y = y_0 = 0; \quad L = L_0; \quad a = a_0$$

Two of the partial derivatives, evaluated at the zero order solution, are given by:

$$\frac{\partial c_1}{\partial x} = \frac{-G m_1 m_2 m_3}{M_{12}} \left[\frac{-15a_0^2}{8\sqrt{L_0}R^5}(\hat{\mathbf{a}}.\mathbf{R})^2 + \frac{3a_0^2}{8\sqrt{L_0}R^5}(\hat{\mathbf{b}}.\mathbf{R})^2 \right.$$
$$\left. + \frac{a_0^2}{2\sqrt{L_0}R^3} + \frac{9ia_0^2}{4\sqrt{L_0}R^5}(\hat{\mathbf{a}}.\mathbf{R})(\hat{\mathbf{b}}.\mathbf{R}) \right]$$
$$\frac{\partial c_1}{\partial y} = \frac{-G m_1 m_2 m_3}{M_{12}} \left[\frac{-9a_0^2}{4\sqrt{L_0}R^5}(\hat{\mathbf{a}}.\mathbf{R})(\hat{\mathbf{b}}.\mathbf{R}) - \frac{3ia_0^2}{8\sqrt{L_0}R^5}(\hat{\mathbf{a}}.\mathbf{R})^2 \right.$$
$$\left. + \frac{15ia_0^2}{8\sqrt{L_0}R^5}(\hat{\mathbf{b}}.\mathbf{R})^2 - \frac{ia_0^2}{2\sqrt{L_0}R^3} \right].$$

If * denotes the complex conjugate then the remaining pair are easily obtained from

$$\left(\frac{\partial c_{-1}}{\partial x}\right)^* = \left(\frac{\partial c_1}{\partial x}\right) \quad \text{and} \quad \left(\frac{\partial c_{-1}}{\partial y}\right)^* = \left(\frac{\partial c_1}{\partial y}\right).$$

Having obtained the expressions for the partial derivatives the next step is to perform the integrations in eqn(2.32). Thus

$$\int_{-\infty}^{\infty} \frac{\partial c_{-1}}{\partial x} e^{-i\lambda_0} dt = \frac{-Gm_1m_2m_3}{M_{12}} \left(\frac{-15a_0^2}{8\sqrt{L_0}} \int_{-\infty}^{\infty} \frac{e^{-i(n_0t+\lambda_{00})}(\hat{\mathbf{a}}.\mathbf{R})^2 dt}{R^5} \right.$$

$$+\frac{3a_0^2}{8\sqrt{L_0}} \int_{-\infty}^{\infty} \frac{e^{-i(n_0t+\lambda_{00})}(\hat{\mathbf{b}}.\mathbf{R})^2 dt}{R^5} + \frac{a_0^2}{2\sqrt{L_0}} \int_{-\infty}^{\infty} \frac{e^{-i(n_0t+\lambda_{00})} dt}{R^3}$$

$$\left. -\frac{9a_0^2 i}{4\sqrt{L_0}} \int_{-\infty}^{\infty} \frac{e^{-i(n_0t+\lambda_{00})}(\hat{\mathbf{a}}.\mathbf{R})(\hat{\mathbf{b}}.\mathbf{R}) dt}{R^5} \right)$$

where we have written $\lambda_0 = \lambda_{00} + n_0 t$. The appendix contains formulae which enable these integrals to be computed approximately. From eqn(A.5) the integral

$$\frac{-15a_0^2}{8\sqrt{L_0}} \int_{-\infty}^{\infty} \frac{e^{-i(n_0t+\lambda_{00})}(\hat{\mathbf{a}}.\mathbf{R})^2 dt}{R^5} = -\frac{a_0^2}{\sqrt{L_0}} \frac{e^{-i\lambda_{00}} K^{\frac{5}{2}} \sqrt{\pi} e^{-\frac{2}{3}K}}{nq^3} \times$$

$$\left[\frac{5}{8}(\hat{\mathbf{a}}.\hat{\mathbf{A}})^2 - \frac{5i}{4}(\hat{\mathbf{a}}.\hat{\mathbf{A}})(\hat{\mathbf{a}}.\hat{\mathbf{B}}) - \frac{5}{8}(\hat{\mathbf{a}}.\hat{\mathbf{B}})^2 \right].$$

Similarly, from eqn(A.6),

$$\frac{3a_0^2}{8\sqrt{L_0}} \int_{-\infty}^{\infty} \frac{e^{-i(n_0t+\lambda_{00})}(\hat{\mathbf{b}}.\mathbf{R})^2 dt}{R^5} = \frac{a_0^2}{\sqrt{L_0}} \frac{e^{-i\lambda_{00}} K^{\frac{5}{2}} \sqrt{\pi} e^{-\frac{2}{3}K}}{nq^3}$$

$$\times \left[\frac{1}{8}(\hat{\mathbf{b}}.\hat{\mathbf{A}})^2 - \frac{i}{4}(\hat{\mathbf{b}}.\hat{\mathbf{A}})(\hat{\mathbf{b}}.\hat{\mathbf{B}}) - \frac{1}{8}(\hat{\mathbf{b}}.\hat{\mathbf{B}})^2 \right].$$

Next, we evaluate

$$\begin{aligned} \frac{e^{-i\lambda_{00}} a_0^2}{2\sqrt{L_0}} \int_{-\infty}^{\infty} \frac{e^{-in_0t} dt}{R^3} &= \frac{e^{-i\lambda_{00}} a_0^2 K}{2\sqrt{L_0} nq^3} \int_{-\infty}^{\infty} \frac{e^{-in_0t} d\sigma}{(1+\sigma^2)^2} \\ &= \frac{e^{-i\lambda_{00}} a_0^2 K^{\frac{3}{2}} e^{-\frac{2}{3}K} \sqrt{\pi}}{4\sqrt{L_0} nq^3} \end{aligned}$$

which is smaller by a factor $O(K)$. Finally, from eqn(A.7) the integral

$$\frac{-9a_0^2 i e^{-i\lambda_{00}}}{4\sqrt{L_0}} \int_{-\infty}^{\infty} \frac{e^{-in_0t}(\hat{\mathbf{a}}.\mathbf{R})(\hat{\mathbf{b}}.\mathbf{R}) dt}{R^5} = -\frac{3a_0^2 i e^{-i\lambda_{00}} K^{\frac{5}{2}} \sqrt{\pi} e^{-\frac{2}{3}K}}{4\sqrt{L_0} nq^3} \times$$

$$\left[(\hat{\mathbf{a}}.\hat{\mathbf{A}})(\hat{\mathbf{b}}.\hat{\mathbf{A}}) - i(\hat{\mathbf{a}}.\hat{\mathbf{A}})(\hat{\mathbf{b}}.\hat{\mathbf{B}}) - i(\hat{\mathbf{a}}.\hat{\mathbf{B}})(\hat{\mathbf{b}}.\hat{\mathbf{A}}) - (\hat{\mathbf{a}}.\hat{\mathbf{B}})(\hat{\mathbf{b}}.\hat{\mathbf{B}}) \right].$$

Hence, to leading order (neglecting the term $\sim K^{\frac{3}{2}}$)

$$\int_{-\infty}^{\infty} \frac{\partial c_{-1}}{\partial x} e^{-i\lambda_0} dt = \frac{-Gm_1m_2m_3}{M_{12}} \frac{a_0^2 e^{-i\lambda_{00}} K^{\frac{5}{2}} \sqrt{\pi} e^{-\frac{2K}{3}}}{\sqrt{L_0} n q^3} \Big[-\frac{5}{8}(\hat{\mathbf{a}}.\hat{\mathbf{A}})^2$$

$$+\frac{5i}{4}(\hat{\mathbf{a}}.\hat{\mathbf{A}})(\hat{\mathbf{a}}.\hat{\mathbf{B}}) + \frac{5}{8}(\hat{\mathbf{a}}.\hat{\mathbf{B}})^2 + \frac{1}{8}(\hat{\mathbf{b}}.\hat{\mathbf{A}})^2 - \frac{i}{4}(\hat{\mathbf{b}}.\hat{\mathbf{A}})(\hat{\mathbf{b}}.\hat{\mathbf{B}}) - \frac{1}{8}(\hat{\mathbf{b}}.\hat{\mathbf{B}})^2 - \frac{3i}{4}(\hat{\mathbf{a}}.\hat{\mathbf{A}})(\hat{\mathbf{b}}.\hat{\mathbf{A}})$$

$$-\frac{3}{4}(\hat{\mathbf{a}}.\hat{\mathbf{A}})(\hat{\mathbf{b}}.\hat{\mathbf{B}}) - \frac{3}{4}(\hat{\mathbf{a}}.\hat{\mathbf{B}})(\hat{\mathbf{b}}.\hat{\mathbf{A}}) + \frac{3i}{4}(\hat{\mathbf{a}}.\hat{\mathbf{B}})(\hat{\mathbf{b}}.\hat{\mathbf{B}}) \Big]. \qquad (2.33)$$

The next integral is

$$\int_{-\infty}^{\infty} \frac{\partial c_1}{\partial y} e^{i\lambda_0} dt = \frac{-Gm_1m_2m_3}{M_{12}} \Big(-\frac{9a_0^2 e^{i\lambda_{00}}}{4\sqrt{L_0}} \int_{-\infty}^{\infty} \frac{e^{in_0 t}(\hat{\mathbf{a}}.\mathbf{R})(\hat{\mathbf{b}}.\mathbf{R}) dt}{R^5}$$

$$-\frac{3ia_0^2 e^{i\lambda_{00}}}{8\sqrt{L_0}} \int_{-\infty}^{\infty} \frac{e^{in_0 t}(\hat{\mathbf{a}}.\mathbf{R})^2 dt}{R^5} + \frac{e^{i\lambda_{00}} 15ia_0^2}{8\sqrt{L_0}} \int_{-\infty}^{\infty} \frac{e^{in_0 t}(\hat{\mathbf{b}}.\mathbf{R})^2 dt}{R^5}$$

$$-\frac{e^{i\lambda_{00}} ia_0^2}{2\sqrt{L_0}} \int_{-\infty}^{\infty} \frac{e^{in_0 t} dt}{R^3} \Big).$$

¿From eqn(A.7) the integral

$$-\frac{9a_0^2 e^{i\lambda_{00}}}{4\sqrt{L_0}} \int_{-\infty}^{\infty} \frac{e^{in_0 t}(\hat{\mathbf{a}}.\mathbf{R})(\hat{\mathbf{b}}.\mathbf{R}) dt}{R^5} = \frac{a_0^2 e^{i\lambda_{00}} K^{\frac{5}{2}} \sqrt{\pi} e^{-\frac{2}{3}K}}{\sqrt{L_0} n q^3} \times$$

$$\Big[\frac{-3}{4}(\hat{\mathbf{a}}.\hat{\mathbf{A}})(\hat{\mathbf{b}}.\hat{\mathbf{A}}) + \frac{-3i}{4}(\hat{\mathbf{a}}.\hat{\mathbf{A}})(\hat{\mathbf{b}}.\hat{\mathbf{B}}) - \frac{3i}{4}(\hat{\mathbf{a}}.\hat{\mathbf{B}})(\hat{\mathbf{b}}.\hat{\mathbf{A}}) + \frac{3}{4}(\hat{\mathbf{a}}.\hat{\mathbf{B}})(\hat{\mathbf{b}}.\hat{\mathbf{B}}) \Big].$$

and

$$-\frac{3ia_0^2 e^{i\lambda_{00}}}{8\sqrt{L_0}} \int_{-\infty}^{\infty} \frac{e^{in_0 t}(\hat{\mathbf{a}}.\mathbf{R})^2 dt}{R^5} = \frac{a_0^2 e^{i\lambda_{00}} K^{\frac{5}{2}} \sqrt{\pi} e^{-\frac{2}{3}K}}{\sqrt{L_0} n q^3} \times$$

$$\Big[\frac{-i}{8}(\hat{\mathbf{a}}.\hat{\mathbf{A}})^2 + \frac{1}{4}(\hat{\mathbf{a}}.\hat{\mathbf{A}})(\hat{\mathbf{a}}.\hat{\mathbf{B}}) + \frac{i}{8}(\hat{\mathbf{a}}.\hat{\mathbf{B}})^2 \Big].$$

Similarly, it is found that

$$\frac{e^{i\lambda_{00}} 15ia_0^2}{8\sqrt{L_0}} \int_{-\infty}^{\infty} \frac{e^{in_0 t}(\hat{\mathbf{b}}.\mathbf{R})^2 dt}{R^5} = \frac{a_0^2 e^{i\lambda_{00}} K^{\frac{5}{2}} \sqrt{\pi} e^{-\frac{2}{3}K}}{\sqrt{L_0} n q^3} \times$$

$$\Big[\frac{5i}{8}(\hat{\mathbf{b}}.\hat{\mathbf{A}})^2 - \frac{5}{4}(\hat{\mathbf{b}}.\hat{\mathbf{A}})(\hat{\mathbf{b}}.\hat{\mathbf{B}}) - \frac{5i}{8}(\hat{\mathbf{b}}.\hat{\mathbf{B}})^2 \Big]$$

and the remaining integral

$$\frac{-e^{i\lambda_{00}} ia_0^2}{2\sqrt{L_0}} \int_{-\infty}^{\infty} \frac{e^{in_0 t} dt}{R^3}$$

can again be neglected.

Hence to leading order (neglecting terms $\sim K^{\frac{3}{2}}$)

$$\int_{-\infty}^{\infty} \frac{\partial c_1}{\partial y} e^{i\lambda_0} dt = \frac{-Gm_1m_2m_3}{M_{12}} \frac{a_0^2 e^{i\lambda_{00}} K^{\frac{5}{2}} \sqrt{\pi} e^{-\frac{2}{3}K}}{\sqrt{L_0} n q^3} \left[-\frac{3}{4}(\hat{\mathbf{a}}.\hat{\mathbf{A}})(\hat{\mathbf{b}}.\hat{\mathbf{A}}) \right.$$

$$-\frac{3i}{4}(\hat{\mathbf{a}}.\hat{\mathbf{A}})(\hat{\mathbf{b}}.\hat{\mathbf{B}}) - \frac{3i}{4}(\hat{\mathbf{a}}.\hat{\mathbf{B}})(\hat{\mathbf{b}}.\hat{\mathbf{A}}) + \frac{3}{4}(\hat{\mathbf{a}}.\hat{\mathbf{B}})(\hat{\mathbf{b}}.\hat{\mathbf{B}}) - \frac{i}{8}(\hat{\mathbf{a}}.\hat{\mathbf{A}})^2 + \frac{1}{4}(\hat{\mathbf{a}}.\hat{\mathbf{A}})(\hat{\mathbf{a}}.\hat{\mathbf{B}})$$

$$\left. +\frac{i}{8}(\hat{\mathbf{a}}.\hat{\mathbf{B}})^2 + \frac{5i}{8}(\hat{\mathbf{b}}.\hat{\mathbf{A}})^2 - \frac{5}{4}(\hat{\mathbf{b}}.\hat{\mathbf{A}})(\hat{\mathbf{b}}.\hat{\mathbf{B}}) - \frac{5i}{8}(\hat{\mathbf{b}}.\hat{\mathbf{B}})^2 \right]. \qquad (2.34)$$

The other integrals are computed by taking the complex conjugate of the expressions in eqns(2.34) and (2.33).

Since

$$\int_{-\infty}^{\infty} e^{-i\lambda_0} \frac{\partial c_{-1}}{\partial y} dt = \left(\int_{-\infty}^{\infty} e^{i\lambda_0} \frac{\partial c_1}{\partial y} dt \right)^*$$

it can therefore be deduced that

$$\int_{-\infty}^{\infty} e^{-i\lambda_0} \frac{\partial c_{-1}}{\partial y} dt = \frac{-Gm_1m_2m_3}{M_{12}} \frac{a_0^2 e^{-i\lambda_{00}} K^{\frac{5}{2}} \sqrt{\pi} e^{-\frac{2}{3}K}}{\sqrt{L_0} n q^3} \left[\frac{-3}{4}(\hat{\mathbf{a}}.\hat{\mathbf{A}})(\hat{\mathbf{b}}.\hat{\mathbf{A}}) \right.$$

$$+\frac{3i}{4}(\hat{\mathbf{a}}.\hat{\mathbf{A}})(\hat{\mathbf{b}}.\hat{\mathbf{B}}) + \frac{3i}{4}(\hat{\mathbf{a}}.\hat{\mathbf{B}})(\hat{\mathbf{b}}.\hat{\mathbf{A}}) + \frac{3}{4}(\hat{\mathbf{a}}.\hat{\mathbf{B}})(\hat{\mathbf{b}}.\hat{\mathbf{B}}) + \frac{i}{8}(\hat{\mathbf{a}}.\hat{\mathbf{A}})^2 + \frac{1}{4}(\hat{\mathbf{a}}.\hat{\mathbf{A}})(\hat{\mathbf{a}}.\hat{\mathbf{B}})$$

$$\left. -\frac{i}{8}(\hat{\mathbf{a}}.\hat{\mathbf{B}})^2 - \frac{5i}{8}(\hat{\mathbf{b}}.\hat{\mathbf{A}})^2 - \frac{5}{4}(\hat{\mathbf{b}}.\hat{\mathbf{A}})(\hat{\mathbf{b}}.\hat{\mathbf{B}}) + \frac{5i}{8}(\hat{\mathbf{b}}.\hat{\mathbf{B}})^2 \right]. \qquad (2.35)$$

Similarly,

$$\int_{-\infty}^{\infty} \frac{\partial c_1}{\partial x} e^{i\lambda_0} dt = \left(\int_{-\infty}^{\infty} \frac{\partial c_{-1}}{\partial x} e^{-i\lambda_0} dt \right)^*$$

and it can be deduced that

$$\int_{-\infty}^{\infty} \frac{\partial c_1}{\partial x} e^{i\lambda_0} dt = \frac{-Gm_1m_2m_3}{M_{12}} \frac{a_0^2 e^{i\lambda_{00}} K^{\frac{5}{2}} \sqrt{\pi} e^{-\frac{2K}{3}}}{\sqrt{L_0} n q^3} \left[-\frac{5}{8}(\hat{\mathbf{a}}.\hat{\mathbf{A}})^2 \right.$$

$$-\frac{5i}{4}(\hat{\mathbf{a}}.\hat{\mathbf{A}})(\hat{\mathbf{a}}.\hat{\mathbf{B}}) + \frac{5}{8}(\hat{\mathbf{a}}.\hat{\mathbf{B}})^2 + \frac{1}{8}(\hat{\mathbf{b}}.\hat{\mathbf{A}})^2 + \frac{i}{4}(\hat{\mathbf{b}}.\hat{\mathbf{A}})(\hat{\mathbf{b}}.\hat{\mathbf{B}}) - \frac{1}{8}(\hat{\mathbf{b}}.\hat{\mathbf{B}})^2$$

$$\left. +\frac{3i}{4}(\hat{\mathbf{a}}.\hat{\mathbf{A}})(\hat{\mathbf{b}}.\hat{\mathbf{A}}) - \frac{3}{4}(\hat{\mathbf{a}}.\hat{\mathbf{A}})(\hat{\mathbf{b}}.\hat{\mathbf{B}}) - \frac{3}{4}(\hat{\mathbf{a}}.\hat{\mathbf{B}})(\hat{\mathbf{b}}.\hat{\mathbf{A}}) - \frac{3i}{4}(\hat{\mathbf{a}}.\hat{\mathbf{B}})(\hat{\mathbf{b}}.\hat{\mathbf{B}}) \right]. \qquad (2.36)$$

To compute L_2 the results from eqns(2.36), (2.33), (2.34) and (2.35) are substituted into (2.32). The terms ($\sim K^4$) and lower powers may be neglected since it is assumed that K is large. It is then found that

$$L_2 = -\frac{G^2 m_1^2 m_2^2 m_3^2}{M_{12}^2} \frac{K^5 \pi e^{-\frac{4}{3}K} a_0^4}{L_0 n^2 q^6} \left[\frac{5}{32}(\hat{\mathbf{a}}.\hat{\mathbf{A}})^4 + \frac{5}{32}(\hat{\mathbf{a}}.\hat{\mathbf{B}})^4 + \frac{5}{32}(\hat{\mathbf{b}}.\hat{\mathbf{A}})^4 \right.$$

$$\left. +\frac{5}{32}(\hat{\mathbf{b}}.\hat{\mathbf{B}})^4 - \frac{9}{8}(\hat{\mathbf{a}}.\hat{\mathbf{A}})^2(\hat{\mathbf{a}}.\hat{\mathbf{B}})(\hat{\mathbf{b}}.\hat{\mathbf{A}}) + \frac{9}{8}(\hat{\mathbf{a}}.\hat{\mathbf{A}})(\hat{\mathbf{b}}.\hat{\mathbf{A}})^2(\hat{\mathbf{b}}.\hat{\mathbf{B}}) + \frac{5}{16}(\hat{\mathbf{a}}.\hat{\mathbf{A}})^2(\hat{\mathbf{b}}.\hat{\mathbf{A}})^2 \right.$$

$$-\frac{13}{4}(\hat{\mathbf{a}}.\hat{\mathbf{A}})(\hat{\mathbf{a}}.\hat{\mathbf{B}})(\hat{\mathbf{b}}.\hat{\mathbf{A}})(\hat{\mathbf{b}}.\hat{\mathbf{B}})+\frac{9}{8}(\hat{\mathbf{a}}.\hat{\mathbf{A}})^3(\hat{\mathbf{b}}.\hat{\mathbf{B}})+\frac{9}{8}(\hat{\mathbf{a}}.\hat{\mathbf{B}})^2(\hat{\mathbf{a}}.\hat{\mathbf{A}})(\hat{\mathbf{b}}.\hat{\mathbf{B}})$$
$$+\frac{9}{8}(\hat{\mathbf{b}}.\hat{\mathbf{B}})^3(\hat{\mathbf{a}}.\hat{\mathbf{A}})+\frac{31}{16}(\hat{\mathbf{a}}.\hat{\mathbf{A}})^2(\hat{\mathbf{b}}.\hat{\mathbf{B}})^2-\frac{9}{8}(\hat{\mathbf{a}}.\hat{\mathbf{B}})^3(\hat{\mathbf{b}}.\hat{\mathbf{A}})-\frac{9}{8}(\hat{\mathbf{a}}.\hat{\mathbf{B}})(\hat{\mathbf{b}}.\hat{\mathbf{A}})^3$$
$$-\frac{9}{8}(\hat{\mathbf{b}}.\hat{\mathbf{B}})^2(\hat{\mathbf{a}}.\hat{\mathbf{B}})(\hat{\mathbf{b}}.\hat{\mathbf{A}})+\frac{31}{16}(\hat{\mathbf{a}}.\hat{\mathbf{B}})^2(\hat{\mathbf{b}}.\hat{\mathbf{A}})^2+\frac{5}{16}(\hat{\mathbf{a}}.\hat{\mathbf{B}})^2(\hat{\mathbf{b}}.\hat{\mathbf{B}})^2$$
$$+\frac{5}{16}(\hat{\mathbf{a}}.\hat{\mathbf{A}})^2(\hat{\mathbf{a}}.\hat{\mathbf{B}})^2+\frac{5}{16}(\hat{\mathbf{b}}.\hat{\mathbf{A}})^2(\hat{\mathbf{b}}.\hat{\mathbf{B}})^2\Bigg]. \qquad (2.37)$$

Since the orbit of the binary is initially circular this result should be independent of the orientation of the $(\hat{\mathbf{A}},\hat{\mathbf{B}})$ axis and the $(\hat{\mathbf{a}},\hat{\mathbf{b}})$ axis. This may be checked by replacing

$$(\hat{\mathbf{a}}.\hat{\mathbf{A}})=\cos\theta \qquad (\hat{\mathbf{b}}.\hat{\mathbf{A}})=\sin\theta$$
$$(\hat{\mathbf{a}}.\hat{\mathbf{B}})=-\sin\theta \qquad (\hat{\mathbf{b}}.\hat{\mathbf{B}})=\cos\theta$$

The result in eqn(2.37) simplifies to give

$$L_2 \;=\; -\frac{G^2m_1^2m_2^2m_3^2}{M_{12}^2}\frac{K^5\pi e^{-\frac{4K}{3}}a_0^4}{L_0n^2q^6}(\frac{9}{2}).$$

The energy of a binary orbit is given by the formula (cf. Marchal 1990)

$$\varepsilon=-\frac{\mu^2m^3}{2L^2}$$

where

$$m=\frac{m_1m_2}{M_{12}} \quad \text{as before and} \quad \mu=GM_{12}.$$

To second order this means that

$$\begin{aligned}\delta\varepsilon_{mean} &= \frac{\mu^2m^3}{L_0^3}L_2\\ &= -\frac{\mu^2m^3}{L_0^3}\frac{K^5\pi e^{-\frac{4K}{3}}}{a_0^2L_0n^2}\left(\frac{18M_{12}^2}{M_{123}^2K^4}\right)\frac{G^2m_1^2m_2^2m_3^2}{M_{12}^2}\end{aligned}$$

using the fact that

$$\frac{a_0^6}{q^6}=\frac{4M_{12}^2}{M_{123}^2K^4}.$$

We also have

$$L_0=m\sqrt{\mu a_0} \quad \text{and} \quad \frac{\mu^2m^3}{L_0^4n^2}=\frac{a_0}{m\mu} \quad \text{and} \quad \frac{a_0^6}{q^6}=\frac{4M_{12}^2}{M_{123}^2K^4},$$

where we have used the definition of L in eqn(2.28) and eqn(2.10). Therefore

$$\delta\varepsilon_{mean} \;=\; -\frac{18Gm_1m_2m_3^2K\pi e^{-\frac{4K}{3}}}{a_0M_{123}^2}.$$

When $q = 4$, $a_0 = 1$, $G = m_1 = m_2 = m_3 = 1$ we find that $\delta\varepsilon_{mean} = -0.000259\ldots$. This contribution is added to the graph obtained analytically in fig(2.7). The mean value is now in much better agreement with the numerical results.

It might be of interest to extend this result by calculating $\delta\varepsilon_{mean}$ at higher angles of inclination. We would then have to consider the Delaunay variables h and H which were neglected in the coplanar case.

2.4.5 Summary

Analytical and numerical calculations show the energy change in a binary system in a variety of different cases when it is perturbed by the influence of a third star moving on a distant parabolic orbit. Although this chapter considers the least dramatic case in which the third star and binary *mildly* interact with each other it, nevertheless, forms an interesting extension to the paper by Heggie(1975).

Chapter 3

Chaotic Scattering

Hill's problem is a useful model for describing the motion of a star within a globular cluster (cf. sec 1.3). The rate at which stars escape from a globular cluster has important applications in astrophysics. The aim of this chapter is to investigate the dynamics of escaping orbits using, not Hill's problem, but a simplified *model problem* which was developed for other purposes in a paper by Hénon(1988). This model, which is easy to implement numerically and is amenable to analytic investigation, closely resembles the classical Hill problem but can be reduced to the study of a piecewise linear two dimensional mapping. The Hill problem contains many fine structures (which were observed in an earlier paper by Hénon and Petit 1986) and it turns out that the model problem exhibits similar structures.

The model problem may be used to clarify our understanding of the way in which different regions of phase space become mixed together. In Hill's problem certain regions correspond to orbits which remain tightly bound to the smaller primary, or, in application to star clusters, constrained within the interior of the cluster. Other regions are associated with escaping orbits. We shall see that a simple mechanism exists which governs the transport of phase space from one region to another. This mechanism is known as a *turnstile*. To make the transition a particle has to pass through the turnstile. One could picture this as follows.

Consider a ball bouncing (elastically) in a dark room whose only connec-

tion with the outside world is through a small window. The ball will continue bouncing off the walls until it finds the 'escape passage'. The room (by virtue of its walls) may be thought of as the constrained region and the window may be regarded as the turnstile through which the ball passes before escaping. A turnstile permits the transport of phase space in both directions. One could imagine a ball entering the room from outside - assuming that it is travelling on an appropriate trajectory. After a certain time (measured crudely in terms of the number of bounces) we suppose that the ball will eventually escape - re-entering the unconstrained region for a second time. The time required for this to happen is closely linked to the concept of a *residence time distribution* or *escape distribution.*

The model problem developed by Hénon lends itself well to the application of turnstile dynamics. In section (3.2) a mathematical description of the model is presented which introduces such concepts as the *invariant manifolds.* These manifolds create partial barriers to the transport of phase space and form the boundary line between the separate regions. It turns out that these manifolds play a fundamental role in understanding how phase space is entrained and detrained from the constrained region. They intersect many times resulting in a complicated geometrical structure known as a *homoclinic tangle.* This structure, which stretches and deforms elements of phase space, was mentioned in chapter one and will be referred to again later. Analytical and computational techniques are employed in sections (3.10) and (3.11) to compute the rate of transport or flux of phase space between the separate regions. From this an escape distribution can be calculated. The numerical approach in determining the distribution of escape times is described in a paper by Rom-Kedar, Leonard and Wiggins (1988). The technique employed is efficient and dramatically reduces the computational effort compared to a "brute force" method which the authors also describe.

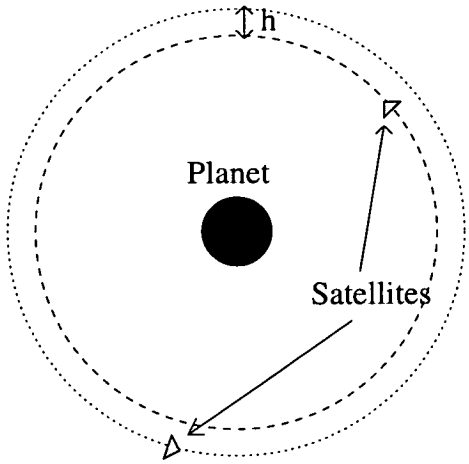

Figure 3.1: Satellite Encounters : the satellites move on initially circular orbits.

3.1 Background to the model

Hénon and Petit (1986) observed the phenomenon of chaotic scattering in satellite encounters. They considered the gravitational interaction of two small satellites moving on initially nearly circular coplanar orbits around a planet. These authors showed (using rotating axes and an appropriate change of scale) that, when the two satellites are close together, this problem is equivalent to the classical *Hill's Problem.* A one parameter family of orbits may be considered by varying the *impact parameter* h, which characterises the radial separation between the initially circular orbits - see fig.(3.1). This gives rise to a one parameter family of solutions to Hill's problem. In a typical orbit the two bodies approach each other, interact for a while and then separate.

Numerical studies have revealed that this family of orbits has an intricate structure. One finds that within a finite interval of h the solution changes continuously. This is referred to as the *interval of continuity.* At each end of this interval there is a value of h which gives rise to a sudden change in the shape of the solution. This value of h is called a *transition value* - see fig(3.2).

It has been observed that between any two such intervals there is always a finite intervening space. So an interval of continuity of behaviour exists on one side of the transition value but not on the other. A study of the intervening space presents a similar picture. Intervals of continuity are discovered which

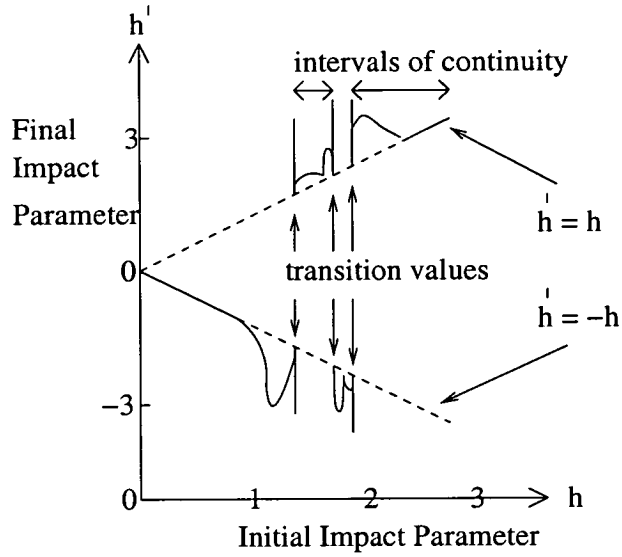

Figure 3.2: This function illustrates the typical behaviour of the final impact parameter as a function of the initial impact parameter. The transition zones correspond to regions of violent change in the behaviour of the system.

h' may be viewed in the following way. For times sufficiently long after the satellites' closest encounter the satellites become so far apart that their mutual gravitational attraction becomes negligible. Each satellite then describes Keplerian motion about the planet. These orbits are, however, no longer circular and h' may be regarded as the *average* radial separation. There are two possible ways in which the two satellites move away from each other. This gives rise to both positive and negative values of h'. (A more precise explanation of this is given in Hénon and Petit (1986).)

Notice that $|h'| \geq |h|$. The authors show that the radial separation of the two satellites can only increase under the effect of the encounter. This is due to the assumption that the orbits are initially circular; if arbitrary initial orbits were allowed the radial separation could decrease as well as increase.

do not touch the previous ones, nor each other, and which are separated by a larger number of smaller intervening spaces. This repeats on a smaller and smaller scale suggesting a self-similar structure. The transition values therefore form a cantor-like set.

Hénon and Petit (1986) accurately located many of these transition values. Each value is associated with an orbit which is asymptotic to a periodic solution to Hill's problem. (Viewed on a Poincare surface this periodic solution gives rise to a fixed point - say p.) If h is slightly larger than the transition value we obtain a continuous family of orbits which escape to infinity (i.e. along one branch of the *unstable invariant manifold* of p). This explains the interval of continuity on one side of the transition value.

On the other hand, if h is slightly less than the transition value the result is a discontinuous family. These latter orbits are considerably more complex and explain the absence of continuity on the other side of the transition value.

It should be remarked that the asymptotic orbits referred to here are those which emanate from the Lagrangian point L_2 (Hénon,1969).

Other problems (referred to in Hénon (1988)) have been discovered which exhibit similar behaviour: classical collision between an atom and a diatomic molecule, scattering of a particle by a two-dimensional potential, collisions of vortex pairs, scattering of an electron by a magnetic dipole, a billiard formed by three circular disks. In all these problems two objects approach each other from a great distance. There is an interaction phase followed by separation, as described in chapter two. In such contexts, this behaviour is often referred to as *irregular* or *chaotic* scattering.

3.2 Hénon's Model Problem using Billiards

Certain difficulties arise in the study of Hill's problem : (i) Numerical integration of the differential equations of motion is time-consuming. (ii) The relevant periodic orbits have large eigenvalues which make them very unstable. For this

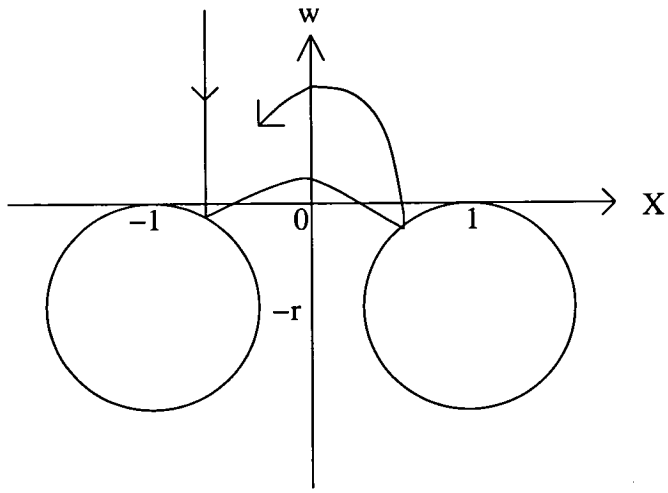

Figure 3.3: The inclined billiard

reason, the orbits are sensitive to small changes in the initial value h. High accuracy integration is required and even then very few levels of the self-similar hierarchical structure can be observed.

To overcome these difficuties and in order to study the transition values in greater depth Hénon(1988) devised the following model problem using billiards. The problem mimics the behaviour of Hill's problem and turns out to be useful for our purposes in understanding the escape phenomenon.

We suppose that a point particle, subject to a constant acceleration g (in the negative Y direction), bounces elastically on two fixed circular disks. The disks have radius r and their centres are at $(-1, -r)$ and $(1, -r)$. For most initial conditions the particle will escape after a certain number of bounces, falling down through the space between the bodies or on either side.

A one-parameter family of orbits can be defined by assuming that the particle is dropped from rest at (h, Y_0). Y_0 is a positive constant which fixes the energy and h is a variable. (In Hill's problem "fixing the energy" is equivalent to choosing a fixed value for the Hamiltonian - see sec(4.3.3).) Since these orbits are analogous to those investigated by Hénon and Petit (1986) it is expected that this family will display the same type of structures. We might therefore expect intervals of h in which the orbit changes continuously and critical values of h at which a transition in behaviour is observed. For $h = 1$ the particle will

bounce ad infinitum on the right disk. This is an unstable periodic orbit. (In the case of Hill's problem this orbit corresponds to the Lyapounov orbit around the Lagrangian point L_2 (cf. sec. 1.3.1).) If h lies either to the left or right of this point (i.e. $h = 1 - \delta$ or $h = 1 + \delta$ where δ is small and positive) a different kind of motion is observed. In the latter case the particle 'escapes' and never returns. (In Hill's problem a similar situation occurs. Escape can occur at either the left or right of the cluster and the two Lyapounov orbits are found to play a crucial role in this process.) In the former case the motion is less clear. The particle is found to bounce initially to the left of $x = 1$ and a complex interplay involving the two disks is possible. (In Hill's problem this corresponds to a star which is temporarily constrained in the cluster - see sec. 1.5.) So $h = 1$ is associated with a transition. A similar periodic orbit is observed at $h = -1$. In general, transitions are present at values of h which lead to solutions which asymptotically approach one of these periodic orbits.

A convenient way of studying this problem is to introduce an explicit mapping. Using a two dimensional surface of section we may record, at each bounce, a point with coordinates X and W, where W is the transverse component of the velocity of the particle. (i.e. the projection of the velocity on the tangent to the disk.) Clearly this mapping will not be defined after the particle has 'escaped'.

Sections (3.3) to (3.8), which summarise the theory developed by Hénon, are followed by two original sections (3.9) and (3.11) on escape distributions. Section (3.10) summarises a piece of dynamical systems theory needed in section (3.11).

3.3 The large r limit

Locating the position at which the next bounce occurs involves calculating the intersection of a parabola and a circle. This is found to be inconvenient to compute numerically. This difficulty can be overcome by making r large. In this case the two disks are seen to overlap.

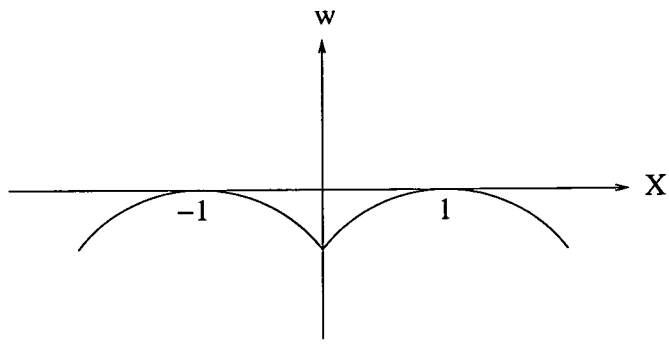

Figure 3.4: The large r limit

Let (X_j, Y_j) be the position of the particle on the j'th rebound. The values of X_j of interest are of order unity:

$$X_j = O(1). \tag{3.1}$$

We may therefore approximate the circumference of the disks by parabolas :

$$Y_j \approx -\frac{(X_j - s_j)^2}{2r}, \tag{3.2}$$

with

$$s_j = \text{sign } X_j. \tag{3.3}$$

¿From now on, the sign $\approx$ is used in the following sense: $\mathcal{E} \approx \mathcal{F}$ implies that $\mathcal{E} = \mathcal{F}[1 + O(r^{-2})]$ where $\mathcal{E}$ and $\mathcal{F}$ are any expressions. One obvious advantage which emerges from this approximation is that the mapping is now always defined and invertible at infinitely large values of time. The particle will bounce indefinitely on the surface both for $t \to +\infty$ and $t \to -\infty$.

The angle between the tangent to the disk/parabola and the horizontal is

$$\theta_j \approx \frac{s_j - X_j}{r}. \tag{3.4}$$

For $X_j = O(1)$, both Y_j and θ_j are small:

$$Y_j = O(r^{-1}), \quad \theta_j = O(r^{-1}). \tag{3.5}$$

The order of the the velocity components U_j, V_j before rebound j can be estimated. The variation of $\frac{U_j}{V_j}$ in a rebound is of order θ_j. The time interval between two consecutive rebounds is of order $\frac{V_j}{g}$; therefore the variation of X_j

from one rebound to the next is of order $\frac{U_j V_j}{g}$. It is of interest to consider mappings in which the variation of every quantity is of the same order as the quantity itself. This gives the two relations

$$\frac{U_j}{V_j} = O(r^{-1}), \qquad \frac{U_j V_j}{g} = O(1), \tag{3.6}$$

from which we deduce that

$$U_j = O(g^{\frac{1}{2}} r^{-\frac{1}{2}}), \qquad V_j = O(g^{\frac{1}{2}} r^{\frac{1}{2}}). \tag{3.7}$$

This implies that $U_j \ll V_j$ and we conclude that the particle velocity is nearly vertical.

The constant total energy (sum of potential and kinetic) is

$$E = gY_j + \frac{1}{2}(U_j^2 + V_j^2). \tag{3.8}$$

¿From eqns(3.5) and (3.7) we obtain

$$E = O(gr) \tag{3.9}$$

and

$$V_j \approx -\sqrt{2E}. \tag{3.10}$$

U_j, V_j are related to the transverse velocity W_j and the normal velocity R_j by

$$W_j = U_j \cos\theta_j + V_j \sin\theta_j, \qquad R_j = -U_j \sin\theta_j + V_j \cos\theta_j. \tag{3.11}$$

Using eqns(3.5) and (3.7), we obtain

$$W_j = O(g^{\frac{1}{2}} r^{-\frac{1}{2}}), \qquad R_j = O(g^{\frac{1}{2}} r^{\frac{1}{2}}), \tag{3.12}$$

and the relations (3.11) reduce to

$$W_j \approx U_j - \sqrt{2E}\theta_j, \qquad R_j \approx V_j \approx -\sqrt{2E}. \tag{3.13}$$

As the collision is elastic

$$W_j' = W_j, \qquad R_j' = -R_j. \tag{3.14}$$

After the rebound (described by the primed quantities U_j', V_j', W_j', R_j') we therefore obtain the relations (similar to eqn(3.13))

$$W_j' = U_j' + \sqrt{2E}\theta_j, \qquad R_j' \approx V_j' \approx \sqrt{2E}. \tag{3.15}$$

The time elapsed between rebounds j and $j+1$ is

$$T = \frac{V'_j - V_{j+1}}{g} \approx \frac{2\sqrt{2E}}{g}, \tag{3.16}$$

and we have

$$X_{j+1} \approx X_j + \frac{2\sqrt{2E}}{g} U'_j, \quad U_{j+1} = U'_j. \tag{3.17}$$

(These equations are approximate and no attempt is made to calculate *exactly* where the $(j+1)$th bounce occurs.) ¿From eqns(3.4),(3.13),(3.15),(3.14) and (3.17), we obtain the mapping from (X_j, W_j) to (X_{j+1}, W_{j+1}) :

$$X_{j+1} \approx X_j + \frac{2\sqrt{2E}}{g} W_j + \frac{4E}{gr}(X_j - s_j), \tag{3.18}$$

$$W_{j+1} \approx W_j + \frac{\sqrt{2E}}{r}(X_j - s_j + X_{j+1} - s_{j+1}). \tag{3.19}$$

In the limit $r \longrightarrow \infty$ the sign $\approx$ may be replaced by $=$ and eqns (3.18) and (3.19) become strict equalities.

3.4 Dimensionless form

Many parameters may be eliminated by reducing this mapping to a standard, dimensionless form. This is achieved through the introduction of a positive dimensionless parameter ψ defined by

$$\cosh\psi = 1 + \frac{4E}{gr}, \quad \sinh\psi = \sqrt{\frac{4E}{gr}(2 + \frac{4E}{gr})}, \tag{3.20}$$

and by effecting the change of variable

$$W_j = w_j \sqrt{\frac{g}{2r}(2 + \frac{4E}{gr})} = \frac{w_j g}{2\sqrt{2E}} \sinh\psi. \tag{3.21}$$

Note that ψ is related to the energy of the particle. Eqns (3.18) and (3.19) then reduce to

$$X_{j+1} = X_j \cosh\psi + w_j \sinh\psi - s_j(\cosh\psi - 1), \tag{3.22}$$

$$w_{j+1} = X_j \sinh\psi + w_j \cosh\psi - (s_j \cosh\psi + s_{j+1}) \tanh\frac{\psi}{2}. \tag{3.23}$$

The only remaining parameter is ψ. This parameter is of great importance as it has a strong bearing on the motion of the particle. It cannot be eliminated

as it is related to the eigenvalues of the fixed points. Eqns(3.22) and (3.23) form a piecewise linear mapping, which we will designate by F. It will be convenient to define

$$x_j = X_j - s_j. \tag{3.24}$$

The equations can then be written as

$$x_{j+1} = x_j \cosh\psi + w_j \sinh\psi + (s_j - s_{j+1}), \tag{3.25}$$

$$w_{j+1} = x_j \sinh\psi + w_j \cosh\psi + (s_j - s_{j+1}) \tanh\frac{\psi}{2}. \tag{3.26}$$

3.5 Properties

3.5.1 Equations for the iterated mapping

By applying eqn(3.25) repeatedly, we obtain explicit equations for F^n:

$$x_n = x_0 \cosh n\psi + w_0 \sinh n\psi$$
$$+\frac{1}{\sinh\psi}\Sigma_{j=1}^{n}\{\sinh[(n-j+1)\psi] - \sinh[(n-j)\psi]\}(s_{j-1} - s_j), \tag{3.27}$$

$$w_n = x_0 \sinh n\psi + w_0 \cosh n\psi$$
$$+\frac{1}{\sinh\psi}\Sigma_{j=1}^{n}\{\cosh[(n-j+1)\psi] - \cosh[(n-j)\psi]\}(s_{j-1} - s_j). \tag{3.28}$$

Using difference formulas, we can also write this as

$$x_n = x_0 \cosh n\psi + w_0 \sinh n\psi + \frac{1}{\cosh\frac{\psi}{2}}\Sigma_{j=1}^{n} \cosh[(n-j+\frac{1}{2})\psi](s_{j-1} - s_j), \tag{3.29}$$

$$w_n = x_0 \sinh n\psi + w_0 \cosh n\psi + \frac{1}{\cosh\frac{\psi}{2}}\Sigma_{j=1}^{n} \sinh[(n-j+\frac{1}{2})\psi](s_{j-1} - s_j). \tag{3.30}$$

These equations are also true for $n = 0$ and $n < 0$ provided we use the following generalised definition of a sum

$$\sum_{j=a+1}^{j=b} f(j) = (\sum_{j=c}^{j=b} - \sum_{j=c}^{j=a}) f(j) \tag{3.31}$$

where c is an integer which satisfies $c \leq \min(a, b)$. The following useful equations may be derived from eqns(3.29) and (3.30) :

$$x_n + w_n = e^{n\psi}\{(x_0 + w_0) + \frac{2e^{\psi}}{e^{\psi}+1}\sum_{j=1}^{n} e^{-j\psi}(s_{j-1} - s_j)\}, \tag{3.32}$$

$$x_n - w_n = e^{-n\psi}\{(x_0 - w_0) + \frac{2e^{-\psi}}{e^{-\psi}+1}\sum_{j=1}^{n} e^{j\psi}(s_{j-1} - s_j)\}, \tag{3.33}$$

or, separating the s_j :

$$x_n + w_n = e^{n\psi}\{(x_0 + w_0) + \frac{2}{e^{\psi}+1}[s_0 - (e^{\psi}-1)\sum_{j=1}^{n-1} e^{-j\psi}s_j - e^{(1-n)\psi}s_n]\}, \tag{3.34}$$

$$x_n - w_n = e^{-n\psi}\{(x_0 - w_0) + \frac{2}{e^{-\psi}+1}[s_0 + (1-e^{-\psi})\sum_{j=1}^{n-1} e^{j\psi}s_j - e^{(n-1)\psi}s_n]\}. \tag{3.35}$$

3.5.2 Fixed Points

When successive rebounds take place on the same disk, eqns(3.25) and (3.26) reduce to the simple form

$$x_{j+1} = x_j \cosh\psi + w_j \sinh\psi, \qquad w_{j+1} = x_j \sinh\psi + w_j \cosh\psi. \tag{3.36}$$

This is a linear mapping, with the fixed point $x = w = 0$. Going back to X, we find that this actually corresponds to two fixed points, depending on which disk is involved:

$$X = 1, \qquad w = 0, \qquad s = 1; \tag{3.37}$$

$$X = -1, \qquad w = 0, \qquad s = -1. \tag{3.38}$$

¿From eqn(3.36) we derive

$$x_{j+1} + w_{j+1} = (x_j + w_j)e^{\psi}, \qquad x_{j+1} - w_{j+1} = (x_j - w_j)e^{-\psi}, \tag{3.39}$$

showing that the eigenvalues of each fixed point are

$$e^{\psi}, \qquad e^{-\psi}. \tag{3.40}$$

Therefore the fixed points are unstable. The associated eigenvectors are given by

$$w = x, \qquad w = -x \tag{3.41}$$

and are shown in fig(3.5). It appears from this figure that the unstable manifolds of the left(right) fixed point joins continuously to the stable manifold of right(left) fixed point.. However, this is not the case. The manifolds break into a number of discontinous sections - see fig(3.18).

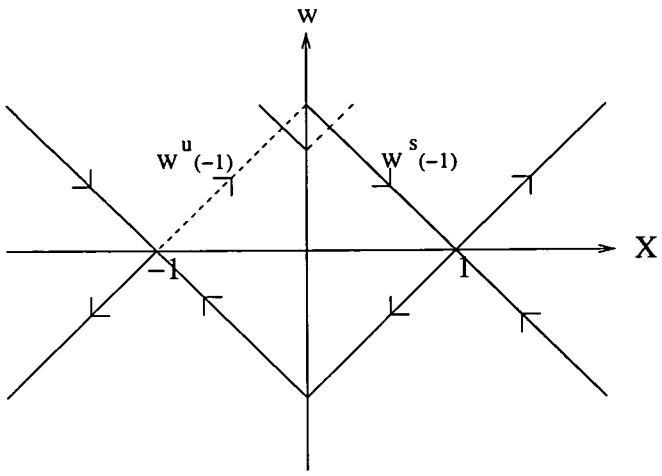

Figure 3.5: Fixed points and invariant manifolds. The unstable manifold of the left fixed point, $W^u(-1)$, is shown as a dashed line segment. Notice how the manifold breaks up into discontinous sections, the first of which is shown here. A more detailed explanation of this feature of the manifold will be given later.

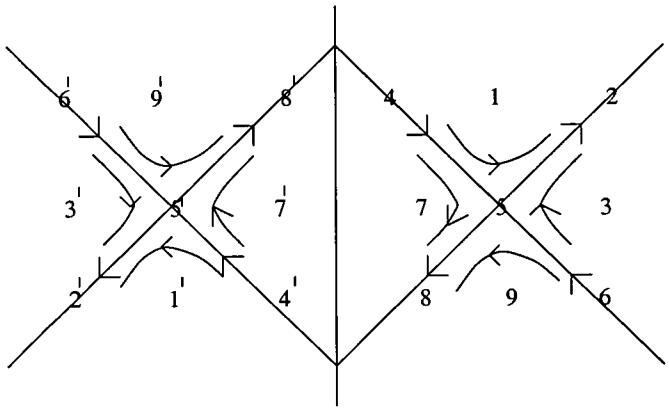

Figure 3.6: Different regions in the surface of section. The arrows indicate the motion of phase space.

3.5.3 Regions in the surface of section

It is useful to divide the (X, w) plane up into 18 regions identified in fig(3.6) by numbers 1 to 9 and $1'$ to $9'$. They are distinguished according to the following conditions:

(i) $X < 0 (s = -1)$ or $X \geq 0 (s = +1)$ [1];

(ii) $x + w$ negative, zero or positive;

(iii) $x - w$ negative, zero or positive.

Note that this implies that regions 1,4,7,8,9 contain the line $X = 0$. Regions 5 and 5′ reduce to single points and correspond to the right and left fixed points respectively. The regions corresponding to different branches of the invariant manifolds (namely regions $2, 4, 6, 8, 2', 4', 6', 8'$) are 1 dimensional. The following lemmas help to explain the movement of phase space in the (X, w) plane between the different regions. (P_j is the point with coordinates (X_j, w_j).)

Lemma 1 If $s_{j+1} = s_j$ then P_{j+1} is in the same region as P_j.

Lemma 2 Regions 1 to 6 are mapped into themselves by F.

Lemma 3 Regions 1′ to 6′ are mapped into themselves by F.

Lemma 4 Regions 2,3,5,6,8,9 are mapped into themselves by F^{-1}.

Lemma 5 Regions $2', 3', 5', 6', 8', 9'$ are mapped into themselves by F^{-1}.

Lemma 6 Regions $7, 8, 9$ map either into themselves or into one of the regions $1', 4', 7'$. Moreover they always map into $1', 4'$ or $7'$ after a finite number of iterations.

Lemma 7 Regions $7', 8', 9'$ map either into themselves or into one of the regions $1, 4, 7$. Moreover they always map into 1,4 or 7 after a finite number of iterations.

3.5.4 Asymptotic behaviour

The following theorem can be deduced using the above lemmas.

Theorem 1. For $j \to +\infty$, any orbit falls after a finite number of iterations into one of the following five asymptotic regimes :

1) right-escaping orbit: the points stay in one of the regions 1,2 or 3; $X_j \to +\infty$, $w \to +\infty$.

[1]This assignment might appear arbitrary. However it is used in Lemma 13 to show an exceptional case concerning bounded orbits when $e^{\psi} = 3$.

2) right-asymptotic orbit : the points stay in one of the regions 4,5 or 6; $X_j \to +1$, $w_j \to 0$.

3) left-escaping orbit : the points stay in one of the regions 1′, 2′ or 3′; $X_j \to -\infty$, $w_j \to -\infty$.

4) left-asymptotic orbit : the points stay in one of the regions 4′, 5′ or 6′; $X_j \to -1$, $w_j \to 0$.

5) oscillating orbit : the points visit alternatively regions 7 and 7′.

A similar theorem can be proved for $j \to -\infty$.

An important consequence is

Theorem 2. If an orbit is not escaping for $j \to +\infty$ (resp. $j \to -\infty$), then X_j and w_j are bounded for $j \to +\infty$ (resp. $j \to -\infty$).

This means that if the orbit falls into categories (2), (4) or (5) it will remain forever bounded.

3.5.5 Computation of X and w from the S sequence

The following results will be required later. A given orbit may be associated with the doubly-infinite sequence

$$S : \ldots s_{-2}, s_{-1}, s_0, s_1, s_2, \ldots \tag{3.42}$$

Lemma 8. If an orbit is bounded for $j \to +\infty$, then $X_j + w_j$ can be expressed as a definite function of the s_k for $k \geq j$:

$$X_j + w_j = \frac{e^{\psi} - 1}{e^{\psi} + 1}[s_j + 2 \sum_{k=j+1}^{+\infty} e^{(j-k)\psi} s_k]. \tag{3.43}$$

Proof. We let $n \to \infty$ in eqn(3.34). Since $x_n + w_n$ is bounded, the quantity between the braces in the right-hand member must vanish in the limit. Extracting $x_0 + w_0$, we obtain the above formula for $j = 0$. A simple translation of the indices gives the formula for arbitrary j.

Similarly, from eqn(3.35)

Lemma 9. If an orbit is bounded for $j \to -\infty$, then $X_j - w_j$ can be expressed as a definite function of the s_k for $k \leq j$:

$$X_j - w_j = \frac{1-e^{-\psi}}{e^{-\psi}+1}[s_j + 2\sum_{k=-\infty}^{j-1} e^{(k-j)\psi} s_k]. \tag{3.44}$$

Combining eqns(3.43) and (3.44), we obtain

Lemma 10. If an orbit is bounded in both directions, then X_j and w_j are definite functions of the sequence S:

$$X_j = \frac{e^{\psi}-1}{e^{\psi}+1}[s_j + \sum_{k=1}^{+\infty} e^{-k\psi}(s_{j+k} + s_{j-k})], \tag{3.45}$$

$$w_j = \frac{e^{\psi}-1}{e^{\psi}+1}[\sum_{k=1}^{+\infty} e^{-k\psi}(s_{j+k} - s_{j-k})]. \tag{3.46}$$

A consequence of this is

Lemma 11 To a given sequence S there corresponds at most one orbit bounded in both directions.

We may now prove

Lemma 12. If

$$e^{\psi} > 3, \tag{3.47}$$

then to any given sequence S there corresponds exactly one orbit bounded in both directions.

Proof. For a given sequence, we can compute the numbers X_j and w_j given by eqns (3.45) and (3.46). The orbit defined by X_j and w_j will correspond to S if all X_j have the correct sign s_j. We have

$$\frac{s_{j-k}}{s_j} \geq -1, \quad \frac{s_{j+k}}{s_j} \geq -1, \tag{3.48}$$

therefore

$$\frac{X_j}{s_j} \geq \frac{e^{\psi}-1}{e^{\psi}+1}[1 - 2\sum_{k=1}^{+\infty} e^{-k\psi}], \tag{3.49}$$

or

$$\frac{X_j}{s_j} \geq \frac{e^{\psi}-3}{e^{\psi}+1} > 0. \tag{3.50}$$

The case $e^{\psi} = 3$ is covered by

Lemma 13. If

$$e^{\psi} = 3, \tag{3.51}$$

then to any given sequence S there corresponds exactly one orbit bounded in both directions, with one exception: if the sequence has the particular form $s_j = -1$ for some j, $s_k = +1$ for $k \neq j$, then there exists no orbit bounded in both directions which corresponds to it.

Proof. The equality in eqn(3.49) is realised only if $s_k/s_j = -1$ for all $k \neq j$. In that case eqn(3.45) gives $X_j = 0$. If $s_j = +1$, the value of X_j still agrees with s_j. But if $s_j = -1$, there is a contradiction and the orbit defined by X_j and w_j does not correspond to S.

3.6 The h-orbits

A one-parameter family of orbits may be defined by the condition that two successive bounces have the same X-coordinate. We suppose that the particle is released from rest at position (h, Y_0); Y_0 is a constant and h is a variable parameter. We then have

$$X_0 = X_1 = h, \tag{3.52}$$

where X_0 is the coordinate of the last rebound before $t = 0$ and X_1 is the coordinate of the first rebound after $t = 0$. (Note that this type of behaviour is generally not permissible if we do not consider the large r limit- see section(3.3).) Clearly this implies that $s_0 = s_1$ and from eqn(3.25)

$$w_0 = -(h - s_0)\tanh\frac{\psi}{2}, \qquad w_1 = (h - s_0)\tanh\frac{\psi}{2}, \tag{3.53}$$

with

$$s_0 = \text{sign}(h). \tag{3.54}$$

In the phase space of the dynamical system the points (X_0, w_0) and (X_1, w_1) are symmetrical with respect to the X-axis. It can be shown, that for any j,

$$X_j = X_{1-j}, \quad s_j = s_{1-j}, \quad w_j = -w_{1-j}, \tag{3.55}$$

i.e. the points (X_j, w_j) and (X_{1-j}, w_{1-j}) are symmetrical about the X axis. This follows from the symmetry of the orbit with respect to $t = 0$.

The application of lemmas 12 and 13 will be required later. So from this point onwards we shall assume that the parameter ψ satisfies

$$e^{\psi} \geq 3. \tag{3.56}$$

If the motion of the particle can be described in terms of this one-parameter family (with ψ satisfying eqn(3.56)) its orbit is called an *h-orbit.*

We can write

$$x_0 = (h - s_0)\frac{\cosh(-\psi/2)}{\cosh(-\psi/2)}, \qquad w_0 = (h - s_0)\frac{\sinh(-\psi/2)}{\cosh(-\psi/2)}, \tag{3.57}$$

and from eqns(3.29) and (3.30) we obtain explicit expressions for x_n and w_n :

$$x_n = \frac{1}{\cosh\frac{\psi}{2}}\{\cosh[(n-\frac{1}{2})\psi](h-s_1)+\Sigma_{j=2}^{n}\cosh[(n-j+\frac{1}{2})\psi](s_{j-1}-s_j)\}, \tag{3.58}$$

$$w_n = \frac{1}{\cosh\frac{\psi}{2}}\{\sinh[(n-\frac{1}{2})\psi](h-s_1)+\Sigma_{j=2}^{n}\sinh[(n-j+\frac{1}{2})\psi](s_{j-1}-s_j)\}. \tag{3.59}$$

Separating the s_j, we also have

$$x_n = h\frac{\cosh[(n-\frac{1}{2})\psi]}{\cosh\frac{\psi}{2}} - 2\tanh\frac{\psi}{2}\Sigma_{j=1}^{n-1}s_j\sinh[(n-j)\psi] - s_n, \tag{3.60}$$

$$w_n = h\frac{\sinh[(n-\frac{1}{2})\psi]}{\cosh\frac{\psi}{2}} - 2\tanh\frac{\psi}{2}\Sigma_{j=1}^{n-1}s_j\cosh[(n-j)\psi] - s_n\tanh\frac{\psi}{2}. \tag{3.61}$$

These equations may be rewritten as

$$X_n = \frac{h\cosh[(n-\frac{1}{2})\psi]}{\cosh\frac{\psi}{2}} - 2\tanh\frac{\psi}{2}\Sigma_{j=1}^{n-1}s_j\sinh[(n-j)\psi], \tag{3.62}$$

$$w_n = \frac{h\sinh[(n-\frac{1}{2})\psi]}{\cosh\frac{\psi}{2}} - 2\tanh\frac{\psi}{2}\Sigma_{j=1}^{n-1}s_j\sinh[(n-j)\psi] - s_n\tanh\frac{\psi}{2}. \tag{3.63}$$

3.7 Symbolic Representation of an h-orbit

It is possible to associate a sequence of binary digits to a given h-orbit.

$$D : d_1, d_2, \ldots, \tag{3.64}$$

with

$$d_j = \begin{cases} 0 & \text{if } s_j=-1, \\ 1 & \text{if } s_j=1. \end{cases} \tag{3.65}$$

where $j = 1, 2 \ldots$. This means that $d_j = 0$ each time the particle bounces on the left disk and $d_j = 1$ for each bounce on the right disk. The D sequence is seen to differ from the S sequence in the choice of symbols. Also the d_j are only defined for $j > 0$.

A number A may be defined by its binary representation:

$$A = 0.d_1 d_2 d_3 \ldots = \sum_{j=1}^{\infty} 2^{-j} d_j. \tag{3.66}$$

This number is of relevance because it is closely linked to the properties of the h-orbit. Note that

$$0 \leq A \leq 1. \tag{3.67}$$

There is not strictly a one-to-one correspondence between the sequence D and the number A. It is true that for each sequence D, there corresponds a unique value of A. However, for each value of A in the interval (3.67) there may correspond either one or two sequences. There are two possible cases which should be distinguished:

1) A is the form

$$k \times 2^{-p} \tag{3.68}$$

where k and p are integers. In this case A is referred to as a *round number* and this case must be divided into three subcases.

a) If $0 < A < 1$, then there exists one representation (3.68) of A for which k is odd and $p > 0$. Two different sequences correspond to A:

$$0.d_1 d_2 \ldots d_{p-1} 0\bar{1} \quad \text{and} \quad 0.d_1 d_2 \ldots d_{p-1} 1\bar{0}. \tag{3.69}$$

Following the standard convention the overline indicates a recurring digit.

b) If $A = 0$ only one corresponding sequence exists :

$$0.\bar{0} \tag{3.70}$$

c) If $A = 1$ only one corresponding sequence exists :

$$0.\bar{1} \tag{3.71}$$

Sequences which contain only a finite number of zeroes such as the first of eqn(3.69) and eqn(3.71) are referred to as *1-ending sequences.* Similarly, sequences which contain only a finite number of 1's such as the second of eqn(3.69) or eqn(3.70) are referred to as *0-ending sequences.*

2) A is not of the form in eqn(3.68). It is referred to as a *non-round number.* In this case only one corresponding D sequence exists. The sequence is neither 0-ending or 1-ending, containing an infinite number of 0's and and an infinite number of 1's. It is referred to as an *oscillating sequence.*

The h-orbits which are right escaping or right asymptotic correspond to round values of A and sequences which are *1-ending.* Orbits which are left-escaping or left asymptotic correspond to round values of A and sequences which are *0-ending.* Orbits which never escape correspond to non-round values of A and sequences which are oscillating.

3.8 Relation between A and h

Since the h-orbit changes continuously within an interval of continuity the sequence of rebounds remains the same throughout the whole of this interval. This means that the value of A is constant. If A is plotted as a function of h (for a fixed value of ψ) a fractal picture is generated. This has the appearance of a *Devil's staircase* consisting of a large number of horizontal segments as shown in fig(3.7). Each segment corresponds to an interval of continuity. A popular review of the Devil's staircase may be found in Bak(1986).

A number of theorems relating to this fractal have been proved by Hénon.

Theorem 3. A is a non-decreasing function of h.

Proof. Consider two different orbits, corresponding to h and h', with the property that $A < A'$. Let us assume that the two D sequences agree up to the $(p\text{-}1)$'th digit. i.e. $d_1 = d'_1$, $d_2 = d'_2$,...,$d_{p-1} = d'_{p-1}$ and $d_p = 0, d'_p = 1 (p \geq 1)$. From eqn(3.60) we then have

$$X'_p - X_p = \frac{\cosh[(p - \frac{1}{2})\psi]}{\cosh \psi/2}(h' - h). \tag{3.72}$$

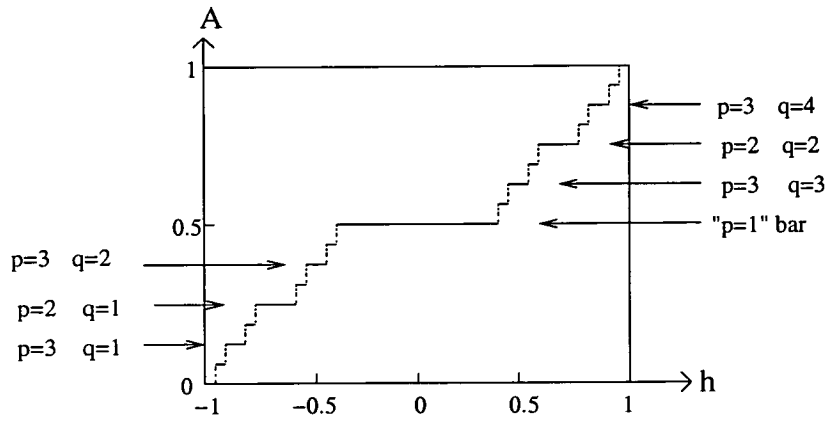

Figure 3.7: The typical form the fractal assumes when $e^{\psi} \geq 3$ (q is an integer which distinguishes bars of the same p-value - it is referred to in sec(3.9)).

Since $X'_p \geq 0$ and $X_p < 0$, it follows that

$$h' > h. \tag{3.73}$$

Conversely, therefore, if $h' < h$ then $A' \leq A$.

Though $A > A'$ implies that $h > h'$ it is *not* true that $A = A'$ implies that $h = h'$. It turns out that there are whole intervals of h which correspond to the same value of A.

We now consider the problem from a different angle and investigate which values of h correspond to a given sequence D or to a given value A.

3.8.1 Non-round A

Consider the case of a non-round A which is associated with an oscillating sequence D. If a corresponding h-orbit exists it will be oscillating and hence bounded by Theorem 2. Suppose, in addition, that eqn(3.56) is satisfied thus permitting the application of lemmas 12 and 13. Then the following theorem holds :

Theorem 4 To any given non-round A there corresponds exactly one h-orbit.

The exceptional case mentioned in lemma 13 does not arise in the case of h-orbits so the theorem holds in the marginal case when $e^{\psi} = 3$.

The value of h can be shown to be (from eqn(3.43) with $j = 0$ and eqn(3.53))

$$h = (e^{\psi} - 1) \sum_{j=1}^{+\infty} e^{-j\psi} s_j. \tag{3.74}$$

3.8.2 Round A, $0 < A < 1$

We now consider the case in which A is a round number in the interval $0 < A < 1$. From eqn(3.69) we see that there are two sequences which correspond to this. The h-orbits, if they exist, will be either asymptotic or escaping.

Asymptotic Orbits

Consider a 0-ending or 1-ending sequence which gives rise to an orbit which is bounded. (This implies that we are dealing with either a left or right asymptotic orbit. After a finite number of iterations the orbit must therefore lie on the stable manifold of one of the two fixed points.) We find a very similar result to the above theorem:

Lemma 14. To any given 0-ending or 1-ending sequence there corresponds exactly one asymptotic h-orbit.

An expression for h may be calculated from eqn(3.74) (since the asymptotic orbits are bounded) using any sequence in which s_1 to s_p is arbitrary and $s_j = -s_p$ for $j > p$. h is given by

$$h = (e^{\psi} - 1) \sum_{j=1}^{p-1} e^{-j\psi} s_j + (e^{\psi} - 2) e^{-p\psi} s_p. \tag{3.75}$$

Theorem 4 and lemma 14 imply the existence of at least one h-orbit for any A. Loosely speaking this means that there can be no "spaces" between the bars. The following theorem may be proved using this result and theorem 3.

Theorem 5. Let $A : [-1, 1] \rightarrow [0, 1]$ be onto and monotonically increasing (not strictly). Then A is continuous.

Proof [2]

We show that that the preimage of a closed interval is closed. Let $[y_1, y_2] \subset [0, 1]$ and $X = A^{-1}([y_1, y_2])$. Our aim is therefore to show that X is closed. If we set

$$x_1 = inf\{x | x \in X\}$$

[2]This proof was suggested by Dr T. Gilbert, University of Edinburgh.

this is equivalent to showing that $x_1 \in X$. Suppose (towards a contradiction) that $x_1 \notin X$. Then $x_1 < x \ \forall\, x \in X$ which implies that $A(x_1) \leq A(x), \ \forall \ x \in X$ and so $A(x_1) \leq y_1$. But $x_1 \notin X$ which means that $A(x_1) \neq y_1$ and so $A(x_1) < y_1$. Suppose that $A(x_1) = y_0$ where $y_0 < y_1$ and consider $\bar{y} = (y_0 + y_1)/2$. Since A is onto then there exists $\bar{x}$ such that $A(\bar{x}) = \bar{y}$. Now $y_0 < \bar{y}$ implies that $x_1 < \bar{x}$ since A is a monotonically increasing function and $\bar{y} < y_1$ implies that $\bar{x} < x \ \ \forall\, x \in X$. This gives a contradiction since $x_1 = inf\{x|x \in X\}$. Hence $x_1 \in X$. A similar argument shows that $sup\{x|x \in X\} \in X$. X is therefore a closed interval and A is continuous.

Escaping Orbits

We consider escaping h-orbits represented symbolically by sequences which are 0-ending or 1-ending. These yield round values of A in the open interval (0,1).

Suppose that we consider a single value of A with the two distinct representations given in eqn(3.69). A right asymptotic orbit can be identified with the 1-ending sequence and the value of h which gives rise to this is found from eqn(3.75):

$$h_- = (e^{\psi} - 1) \sum_{j=1}^{p-1} e^{-j\psi} s_j - (e^{\psi} - 2) e^{-p\psi}. \tag{3.76}$$

The value of h corresponding to the left asymptotic orbit is calculated in similar fashion:

$$h_+ = (e^{\psi} - 1) \sum_{j=1}^{p-1} e^{-j\psi} s_j + (e^{\psi} - 2) e^{-p\psi}. \tag{3.77}$$

This means that

$$h_+ - h_- = 2(e^{\psi} - 2) e^{-p\psi} > 0. \tag{3.78}$$

Since the function $A(h)$ is non-decreasing by theorem 3 it must therefore remain constant throughout the whole interval $h_- \leq h \leq h_+$. This explains why the fractal is composed of an infinite number of horizontal plateaus or bars. Each bar is associated with a round value of A. For a given bar the only bound orbits are asymptotic and are found at $h = h_-$ and $h = h_+$. The open interval (h_-, h_+) consists entirely of escaping orbits.

The sum of all the horizontal bars in fig(3.7) can be shown to be equal to

the length of the base of the fractal. Each bar (which shall be referred to as a *p-bar*) is defined by a sequence of $p-1$ binary digits. In particular, for a 0-ending sequence or 1-ending sequence, there are $p-1$ digits $(s_j, j = 1 \ldots p-1)$ which correspond to the value of $A(h_-)$ or $A(h_+)$. (More will be said about these digits in the following section which deals with escaping orbits.) Since all possible binary sequences are permissible (for $e^{\psi} \geq 3$) this means that there are 2^{p-1} bars for each value of p.

$$\sum_{all\ p\ bars} (h_+ - h_-) = \sum_{p=1}^{\infty} 2^{p-1} 2(e^{\psi} - 2)e^{-p\psi} = 2.$$

This is the expected result since it is the length of the interval (-1,1).

3.9 Escape Distributions I

We shall investigate the time it takes for h-orbits satisfying $e^{\psi} \geq 3$ to escape from the system. The time to escape, for a given value of h, is the smallest integer k such that $|X_n| > 1$ for all $n > k$. In particular we would like to know which values of h (i.e. which sub-intervals of (-1,1)) correspond to orbits which escape after at least k bounces (say) within the constrained region $(-1 \leq X \leq 1)$. By summing up the lengths of these sub-intervals it is possible to produce an escape distribution.

The concept of a horizontal bar (or plateau) was discussed in the previous section and it was mentioned that at each end of every bar there were right and left asymptotic orbits corresponding to $h = h_-$ and $h = h_+$. Clearly these orbits take infinitely many bounces to escape. If we move away from these extremes and consider $h = h_- + \delta$ or $h = h_+ - \delta$ we find orbits which escape after a finite number of bounces. If δ is very small then the time to escape is very long (more precisely, $k \to \infty$ as $\delta \to 0$) but for larger values of δ the escape time becomes shorter. For values of h in the interval (h_-, h_+) (for a given p-bar) the time to escape never falls below p. This is due to the sequence of $p-1$ binary digits,

$$s_1, s_2, \ldots, s_{p-1}, s_p, -s_p, -s_p, \ldots$$

(mentioned in the previous section) associated with the value of $A(h_-)$ or $A(h_+)$.

The first term corresponding to possible escape is the $p+1$th term in the sequence. This means that the orbit must remain bound for at least p bounces and the condition $X_n > 1$ or $X_n < -1$ can only be satisfied for $n \geq p+1$.

If we wish to find those intervals of h which correspond to orbits which remain bound for at least k bounces we require to sum together the full lengths of the horizontal bars for which $p \geq k$. Only partial contributions will be required from the bars with $p < k$. This is because some values of h near the centre of these bars lead to orbits which escape too rapidly (i.e. in under k bounces). The former calculation is straightforward since a formula exists for the length of each bar. Adding the latter contribution the whole calculation may be performed as follows:

Step (i) Finding an expression for the time to escape, k, as a function of δ. This expression may be inverted to yield δ as a function of k. It is necessary to treat either end of each bar separately. We refer to δ_r or δ_l depending on which end is being considered. The total partial contribution from each bar is given by $\delta_r + \delta_l$.

Step (ii) Summing together the partial contributions (of which there are 2^{p-1}) from all the p-bars for each $p < k$.

Step (iii) Considering the contributions from all bars with $p \geq k$.

Steps (ii) and (iii) can be carried out by introducing a double sum. We begin with

Step (i) :

We calculate an expression for $k(\delta)$ by considering the values of h which lead to left and right asymptotic orbits. In both cases the particle will take infinitely long to escape.

¿From eqn(3.77) the left asymptotic orbits for a p-bar occur at

$$h = h_+ = (e^{\psi} - 1) \sum_{j=1}^{p-1} e^{-j\psi} s_j + (e^{\psi} - 2) e^{-p\psi} \tag{3.79}$$

where s_j is any sequence satisfying $s_p = 1$ and $s_j = -1$ for all $j > p$. (Note the change of notation.) Substituting this into eqn(3.62) gives

$$X_n = [(e^{\psi} - 1) \sum_{j=1}^{p-1} e^{-j\psi} s_j + (e^{\psi} - 2) e^{-p\psi}] \frac{1}{2} (e^{n\psi} e^{-\frac{1}{2}\psi} + e^{-n\psi} e^{\frac{1}{2}\psi}) / \cosh \frac{\psi}{2}$$

$$-2\tanh\frac{\psi}{2}\{\sum_{j=1}^{n-1}s_j\frac{1}{2}(e^{n\psi}e^{-j\psi}-e^{-n\psi}e^{j\psi})\}.$$

On expanding this gives, for $n \geq p+1$,

$$X_n = \frac{1}{2\cosh\frac{\psi}{2}}\{e^{-\frac{1}{2}\psi}(e^{\psi}-1)e^{n\psi}\sum_{j=1}^{p-1}e^{-j\psi}s_j + e^{\frac{1}{2}\psi}e^{-n\psi}(e^{\psi}-1)\sum_{j=1}^{p-1}e^{-j\psi}s_j$$

$$+e^{-\frac{1}{2}\psi}(e^{\psi}-2)e^{n\psi}e^{-p\psi} + e^{\frac{1}{2}\psi}(e^{\psi}-2)e^{-n\psi}e^{-p\psi}\}$$

$$-2\tanh\frac{\psi}{2}\{\sum_{j=1}^{p-1}\frac{1}{2}e^{n\psi}e^{-j\psi}s_j - \frac{1}{2}\sum_{j=p+1}^{n-1}e^{n\psi}e^{-j\psi} + \frac{1}{2}e^{n\psi}e^{-p\psi}$$

$$-\sum_{j=1}^{p-1}\frac{1}{2}s_je^{-n\psi}e^{j\psi} - \frac{1}{2}e^{-n\psi}e^{p\psi} + \frac{1}{2}e^{-n\psi}\sum_{j=p+1}^{n-1}e^{j\psi}\}$$

where we have used the fact that $s_p = 1$ and $s_l = -1$ for all $l \geq p+1$. This gives

$$X_n = e^{n\psi}\frac{e^{\psi}-1}{e^{\psi}+1}\sum_{j=1}^{p-1}e^{-j\psi}s_j + \frac{e^{-n\psi}e^{\psi}(e^{\psi}-1)}{e^{\psi}+1}\sum_{j=1}^{p-1}e^{-j\psi}s_j + \frac{e^{\psi}-2}{e^{\psi}+1}e^{n\psi}e^{-p\psi}$$

$$+e^{-n\psi}\frac{e^{\psi}(e^{\psi}-2)e^{-p\psi}}{e^{\psi}+1} - e^{n\psi}\frac{e^{\psi}-1}{e^{\psi}+1}\Sigma_{j=1}^{p-1}e^{-j\psi}s_j$$

$$+(\frac{e^{\psi}-1}{e^{\psi}+1})[e^{n\psi}\frac{e^{-(p+1)\psi}(1-e^{-(n-p-1)\psi})}{1-e^{-\psi}} - e^{n\psi}e^{-p\psi}$$

$$+e^{-n\psi}\sum_{j=1}^{p-1}e^{j\psi}s_j + e^{-n\psi}(\frac{e^{\psi}-1}{e^{\psi}+1})e^{p\psi} - \frac{e^{-n\psi}e^{(p+1)\psi}(1-e^{(n-p-1)\psi})}{1-e^{\psi}}].$$

This simplifies to give

$$X_n = -1 + e^{-n\psi}L_l, \qquad n \geq p+1$$

where

$$L_l = [\frac{e^{\psi}(e^{\psi}-1)}{e^{\psi}+1}\sum_{j=1}^{p-1}e^{-j\psi}s_j + \frac{e^{\psi}(e^{\psi}-2)e^{-p\psi}}{e^{\psi}+1}$$

$$+\tanh\frac{\psi}{2}\{\sum_{j=1}^{p-1}s_je^{j\psi}+e^{p\psi}\} + \frac{e^{(p+1)\psi}}{e^{\psi}+1}].$$

Following the above approach we may obtain a similar expression for right asymptotic orbits. In this case (cf.eqn(3.76))

$$h = h_- = (e^{\psi}-1)\sum_{j=1}^{p-1}e^{-j\psi}s_j - (e^{\psi}-2)e^{-p\psi}$$

and we find that

$$X_n = 1 - e^{-n\psi} L_r$$

where

$$L_r = [\frac{-e^{\psi}(e^{\psi}-1)}{e^{\psi}+1} \sum_{j=1}^{p-1} e^{-j\psi} s_j + \frac{e^{\psi}(e^{\psi}-2)e^{-p\psi}}{e^{\psi}+1}$$

$$- \tanh \frac{\psi}{2} \{ \sum_{j=1}^{p-1} s_j e^{j\psi} - e^{p\psi} \} + \frac{e^{(p+1)\psi}}{e^{\psi}+1}].$$

Now suppose that $h = h_- + \delta_r$ and that the s_j's are the same as in eqn(3.79) (i.e. we are looking at the *same* bar). From eqn(3.62) we would have

$$X'_n = (h_- + \delta_r) \frac{\cosh[(n-\frac{1}{2})\psi]}{\cosh \frac{\psi}{2}} - 2 \tanh \frac{\psi}{2} \sum_{j=1}^{n-1} s_j \sinh[(n-j)\psi]. \qquad (3.80)$$

Then from eqn(3.80) and eqn(3.62) we have

$$X'_n = X_n + \delta_r \frac{\cosh[(n-\frac{1}{2})\psi]}{\cosh \frac{\psi}{2}}$$

and so

$$X'_n = 1 - e^{-n\psi} L_r + \delta_r \frac{\cosh[(n-\frac{1}{2})\psi]}{\cosh \frac{\psi}{2}}. \qquad (3.81)$$

To find the time of escape we are interested in the number of bounces, k, before the particle escapes over the right hill. We find that (solving $X'_k = 1$ and rearranging for δ)

$$\delta_r = \frac{2e^{\frac{\psi}{2}} \cosh(\frac{\psi}{2}) L_r}{e^{2k\psi} + e^{\psi}}.$$

This completes step (i).

Step (ii)

In order to talk about a particular bar two subscripts must be introduced to L_r and L_l. The first subscript p is the integer associated with the bar, indicating the number of digits which occurred in the sequence before the repetition of either zeros or ones. The second subscript q distinguishes between bars of the same p-value.

In the case of bars with $p < k$ we must evaluate

$$\sum_{p=1}^{k-1} \sum_{q=1}^{2^{p-1}} \{ (\delta_l)_{pq} + (\delta_r)_{pq} \}$$

where

$$(\delta_l)_{pq} = \frac{2e^{\frac{\psi}{2}}\cosh(\frac{\psi}{2})(L_l)_{pq}}{e^{2k\psi}+e^{\psi}}, \qquad 1 \le p \le k-1 \tag{3.82}$$

and

$$(\delta_r)_{pq} = \frac{2e^{\frac{\psi}{2}}\cosh(\frac{\psi}{2})(L_r)_{pq}}{e^{2k\psi}+e^{\psi}}, \qquad 1 \le p \le k-1. \tag{3.83}$$

Here we use expressions for L_r and L_l given earlier, e.g.

$$(L_r)_{pq} = [-\frac{e^{\psi}(e^{\psi}-1)}{e^{\psi}+1}\sum_{j=1}^{p-1} e^{-j\psi}s_{qj} + \frac{e^{\psi}(e^{\psi}-2)e^{-p\psi}}{e^{\psi}+1}$$

$$-\tanh\frac{\psi}{2}\{\sum_{j=1}^{p-1} s_{qj}e^{j\psi} - e^{p\psi}\} + \frac{e^{(p+1)\psi}}{e^{\psi}+1}].$$

Note that

$$\sum_{q=1}^{2^{p-1}}(L_r)_{pq} = 2^{p-1}[\frac{e^{\psi}(e^{\psi}-2)e^{-p\psi}}{e^{\psi}+1} + \tanh(\frac{\psi}{2})e^{p\psi} + \frac{e^{(p+1)\psi}}{e^{\psi}+1}]$$

$$-\sum_{q=1}^{2^{p-1}}\sum_{j=1}^{p-1}(e^{\psi}\tanh\frac{\psi}{2}e^{-j\psi}s_{qj} + \tanh(\frac{\psi}{2})s_{qj}e^{j\psi}).$$

The last term can be shown to be zero because, for given j, $s_{qj} = \pm 1$ in equal numbers of bars. Suppose, for example, $p = 3$ then

$$\sum_{q=1}^{4}\sum_{j=1}^{2} e^{-j\psi}s_{qj} = e^{-\psi}s_{11} + e^{-2\psi}s_{12} + e^{-\psi}s_{21} + e^{-2\psi}s_{22}$$

$$+e^{-\psi}s_{31} + e^{-2\psi}s_{32} + e^{-\psi}s_{41} + e^{-2\psi}s_{42}.$$

There is a 1-1 correspondence between the set $\{(s_{i1}, s_{i2}), i = 1..4\}$ and the set $\{(1,-1),(1,1),(-1,1),(-1,-1)\}$. This means that

$$e^{-\psi}(s_{11} + s_{21} + s_{31} + s_{41}) = 0$$

and

$$e^{-2\psi}(s_{12} + s_{22} + s_{32} + s_{42}) = 0.$$

This argument may be generalised for any integer value of p. Hence

$$\sum_{q=1}^{2^{p-1}}\sum_{j=1}^{p-1} e^{-j\psi}s_{qj} = 0$$

and

$$\sum_{q=1}^{2^{p-1}}\sum_{j=1}^{p-1} e^{j\psi}s_{qj} = 0. \tag{3.84}$$

Discarding these terms we then have

$$\sum_{p=1}^{k-1}\sum_{q=1}^{2^{p-1}}(L_r)_{pq} = \sum_{p=1}^{k-1} 2^{p-1}[\frac{e^{\psi}(e^{\psi}-2)e^{-p\psi}}{e^{\psi}+1} + \tanh(\frac{\psi}{2})e^{p\psi} + \frac{e^{(p+1)\psi}}{e^{\psi}+1}]$$

which gives

$$\sum_{p=1}^{k-1}\sum_{q=1}^{2^{p-1}}(L_r)_{pq} = \frac{e^{\psi}(e^{\psi}-2)}{e^{\psi}+1}[\frac{e^{-\psi}(1-(2e^{-\psi})^{k-1})}{1-2e^{-\psi}}]$$

$$+\tanh\frac{\psi}{2}[\frac{e^{\psi}(1-(2e^{\psi})^{k-1})}{1-2e^{\psi}}] + \frac{1}{e^{\psi}+1}[\frac{e^{2\psi}(1-(2e^{\psi})^{k-1})}{(1-2e^{\psi})}]$$

$$= \frac{e^{\psi}2^{k-1}(e^{(k-1)\psi}-e^{-(k-1)\psi})}{e^{\psi}+1}.$$

Hence by eqn(3.83)

$$\sum_{p=1}^{k-1}\sum_{q=1}^{2^{p-1}}(\delta_r)_{pq} = \frac{e^{\psi}2^{k-1}(e^{(k-1)\psi}-e^{-(k-1)\psi})}{e^{2k\psi}+e^{\psi}}.$$

There is an equal contribution from right-escapers, and

$$\sum_{p=1}^{k-1}\sum_{q=1}^{2^{p-1}}\{(\delta_l)_{pq}+(\delta_r)_{pq}\} = \frac{e^{\psi}2^{k}(e^{(k-1)\psi}-e^{-(k-1)\psi})}{e^{2k\psi}+e^{\psi}}.$$

Step (iii)

We must add to this the contribution from the bars with $p \geq k$. ¿From eqn(3.78) the length of each p-bar is given by

$$h_+ - h_- = 2(e^{\psi}-2)e^{-p\psi}.$$

The contribution from the bars with $p \geq k$ is given by

$$\sum_{p=k}^{\infty} 2^{p-1}2(e^{\psi}-2)e^{-p\psi} = \frac{2^k e^{-k\psi}(e^{\psi}-2)}{1-2e^{-\psi}}.$$

Hence the fraction of h-orbits, $Esc(k)$, in the interval $(-1,1)$ which escape after at least k bounces is found by adding together the two contributions (i.e. for $p \geq k$ and $p < k$) and dividing by 2.

$$Esc(k) = \frac{1}{2}\{\frac{e^{\psi}2^{k}(e^{(k-1)\psi}-e^{-(k-1)\psi})}{e^{2k\psi}+e^{\psi}} + \frac{2^k e^{-k\psi}(e^{\psi}-2)}{1-2e^{-\psi}}\}$$

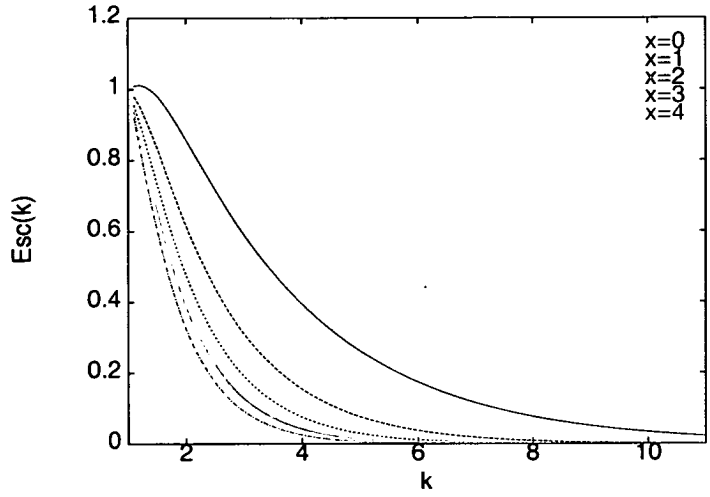

Figure 3.8: $Esc(k)$ against k, $\psi = \ln(3+x), x = 0..4$

$$= 2^{k-1}\frac{\cosh\frac{\psi}{2}}{\cosh((k-\frac{1}{2})\psi)}. \tag{3.85}$$

In fig.(3.8) we plot $Esc(k)$ against k for various ψ. In general terms a larger value of ψ increases the number of fast-escapers causing $Esc(k)$ to decrease more sharply. This is to be expected intuitively since increasing the value of ψ is equivalent to dropping the particle from a greater height. In more mathematical terms if we were to examine fig(3.7) for various ψ we would see that the $p = 1$ bar tends to occupy a larger fraction of the interval (-1,1) as ψ increases. This means that the higher order p-bars which are associated with slow escapers play a less significant role. A plot of $\ln(Esc(k))$ against k is shown in fig(3.9).

The results above have parallels with other studies of escape probabilities. Contopoulos and Kaufmann(1992) have studied escape probabilities in the potential

$$V = \frac{1}{2}(x^2 + y^2) - \epsilon x^2 y^2.$$

This potential may represent the central parts of a galaxy. They consider a fixed energy and various values for ϵ.

Escape distributions in Hamiltonian systems have also been studied in other areas of mathematical astronomy. For example, Kandrup et al. (2000) investigate the statistical properties of orbits escaping from Hamiltonian systems of the form

$$H = H_0 + \epsilon H_1.$$

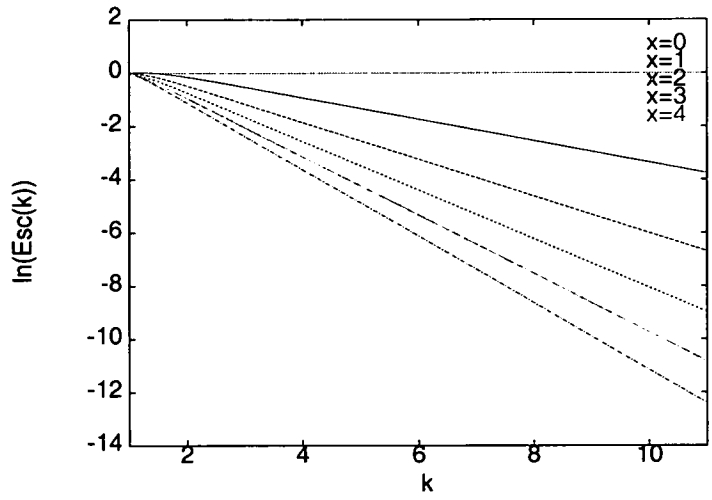

Figure 3.9: ln(Esc(k)) against k, $\psi = \ln(3+x), x = 0..4$ (Only integer values of k should be considered, and so values of $Esc(k)$, which can occur at fractional values of k, are of no significance.)

H_0 is integrable and ϵH_1 is a non-integrable correction.

In these problems a critical value of ϵ exists (say ϵ_0) such for $\epsilon < \epsilon_0$ escape is impossible. The authors show that for higher energies the probability, P, of escape at time t, computed for an arbitrary orbit ensemble decays towards zero exponentially with t. The rate of decay is related to ϵ.

A similar relationship is found to exist in Hénon's problem in the function $Esc(k)$ - although there are some differences. In Hénon's problem time is measured *discretely* in terms of the number of bounces for which the particle remains bound between -1 and 1 (not in terms of a *continuous* variable t). Also, $Esc(k)$ does not give the probability that an arbitrarily chosen h-orbit will escape on the kth bounce - it is the probability that it will escape on *or beyond* the kth bounce. However a common feature in our model and in the models described above is that the exponential decay factor is a function of the energy. In Hénon's model this is clear from fig(3.8). Notice that as $k \to \infty$, $Esc(k)$ decays at a rate which depends on the value of ψ. This decay factor is investigated in the following lemma.

Lemma 15

$$\frac{Esc(k)}{Esc(k-1)} \to \frac{2}{e^{\psi}} \quad \text{as} \quad k \to \infty.$$

Proof

Notice that

$$\frac{Esc(k)}{Esc(k-1)} = \frac{2\cosh(k-\frac{3}{2})\psi}{\cosh(k-\frac{1}{2})\psi} \rightarrow 2e^{-\psi}$$

as $k \rightarrow \infty$.

3.9.1 Numerical Approach

The above theory used to derive the escape distribution is valid only for $e^{\psi} \geq 3$. If $e^{\psi} < 3$ it is possible to construct sequences for which there exists no corresponding h-orbits. (More details may be found in Hénon (1988).) This causes gaps to start appearing between the horizontal bars in fig(3.7) and destroys the continuity of the "devil's staircase". If we tried to repeat the above proof we would be unable to show eqn(3.84). The cancellation of this term was permissible only since we assumed that all possible sequences were to be included. This problem can be overcome by using a numerical technique.

A numerical approach may be used to calculate the escape distribution. This is useful for examining the case in which $e^{\psi} < 3$ and also provides a means of testing the above analytical theory for $e^{\psi} \geq 3$. The technique is described as follows:

We begin by dividing the interval (-1,1) of h into a large number of equally spaced parts. Let us suppose there are N parts each of width $\Delta = 2/N$. We consider the following set of initial conditions for h-orbits in the interval (-1,1)

$$Q = \left\{ (X_{0k} = -1 + k\Delta, w_{0k} = -[X_{0k} - s_0]\tanh\frac{\psi}{2}) \ , \quad k = 1 \ldots N \right\}.$$

The initial X coordinates are distributed uniformly in the interval (-1,1) and the corresponding values for w are calculated from eqn(3.53). Applying the formulae derived earlier these h-orbits are evolved forward in time, i.e. using the iterative scheme

$$X_{j+1} = (X_j - s_j)\cosh\psi + w_j \sinh\psi + s_j$$

and

$$w_{j+1} = (X_j - s_j)\sinh\psi + w_j \cosh\psi + (s_j - s_{j+1})\tanh\frac{\psi}{2}$$

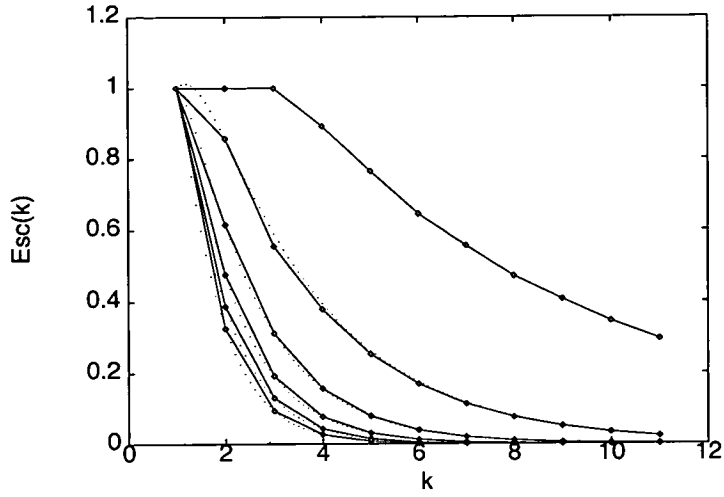

Figure 3.10: Numerical results showing $Esc(k)$ against k, $e^{\psi} = 2, 3..7$ compared with the analytical results in fig(3.8).

(cf. eqns. 3.22, 3.23).

For each h-orbit the minimum number of iterations, k, required to satisfy $|X_k| > 1$ is found, i.e. the time to escape is computed for all h-orbits in the set Q. We then determine what fraction of the h-orbits in Q escape on the first bounce, on the second bounce and so on. In this way an escape distribution can be built up.

If we take $N = 50000$, fig(3.10) shows the numerical results for different values of ψ and values of k up to 11. For comparison we superimpose the analytical results from fig(3.8). The numerical results are in close agreement with the analytical theory. Note that the top curve (obtained for $e^{\psi} = 2$) in fig(3.10) stands alone. Fig.(3.11) provides a better comparison by plotting $\ln(Esc(k))$ against k. For $k > 7$ the numerical results seem to lose accuracy. This occurs when $Esc(k) \approx \frac{1}{N}$, at which point the set of h orbits is too coarsely sampled. This ends the story for h-orbits. We will return to escape distributions in sec(3.10.2) which deals with a more general class of orbits.

3.10 Chaotic Transport

The h-orbits represent a 1-dimensional family of orbits. The h-orbits are analogous to a family of so-called *orthogonal* orbits in Hill's problem which are

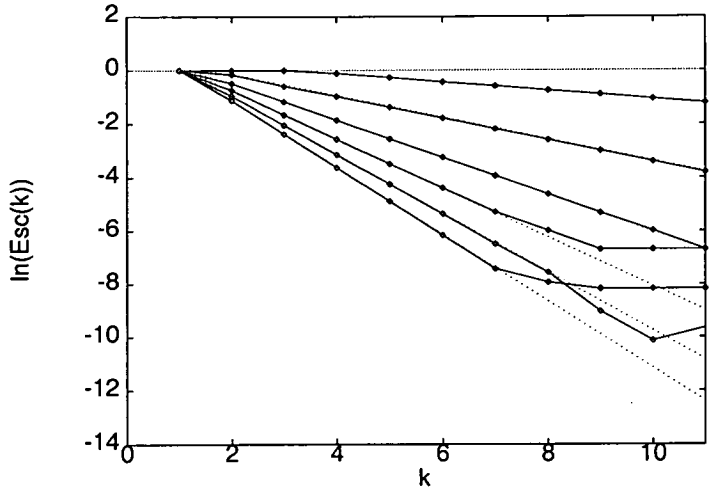

Figure 3.11: Numerical results showing $\ln(Esc(k))$ against k, $e^{\psi} = 2, 3..7$ compared with the analytical results in fig(3.9).

investigated in sec(4.5.2). To develop a more complete picture it would be of interest to derive an escape distribution for orbits with more general initial conditions. This can be achieved by examining the transport of phase space across a suitably defined boundary.

The model problem developed by Hénon contains structures that arise frequently in the study of dynamical systems. Much progress in understanding how these structures may be applied to problems involving phase space transport has been made by Stephen Wiggins. For example, a paper by Rom-Kedar, Leonard and Wiggins (1988) (also mentioned in Wiggins (1992)) investigates the flow field induced by a pair of point vortices using techniques from dynamical systems. Hyperbolic fixed points (denoted by p_1 and p_2 in fig(3.12)) arise in this problem, and the authors use the stable and unstable manifolds of these fixed points to form two separate regions R_1 and R_2. The fixed points are symmetrically located about the origin with the stable and unstable manifolds as shown. We see that there is a general similarity between this system and Hénon's model problem in fig(3.5). Region R_1 can be thought of as containing fluid which has become trapped in the neighbourhood of the vortices. Region R_2 contains fluid which is unconstrained and is referred to as the "free flow region".

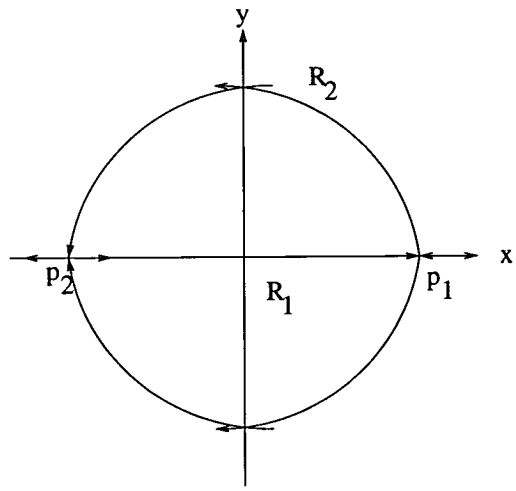

Figure 3.12: Geometry of the stable and unstable manifolds of p_1 and p_2 in the case of a pair of point vortices (after Rom-Kedar et al. 1988).

In order to describe the transport of fluid between the separate regions we need to set up a suitable mathematical framework. The following theory (which is described in detail in Wiggins (1992)) establishes the necessary definitions and theorems, which we then apply from the latter part of sec(3.10.2).

3.10.1 Mathematical Framework

Consider a mapping

$$f : \mathcal{M} \to \mathcal{M}$$

where $\mathcal{M}$ is a differentiable, orientable, 2-dimensional manifold. We will also assume that f is area-preserving and orientation-preserving. These assumptions are in keeping with the definition of the mapping in Hénon's model (except for differentiability). Let $p_i, i = 1, 2$ be two saddle-type hyperbolic fixed points for f. We denote the stable and unstable manifolds of p_i by $W^s(p_i)$ and $W^u(p_i)$ respectively. Fig(3.13) is a useful illustration.

Definition

A point $q \in \mathcal{M}$ is called a heteroclinic point if $q \in W^s(p_j) \cap W^u(p_i)$ for some p_i, p_j, if $i \neq j$. If $i = j$, then q is called a homoclinic point.

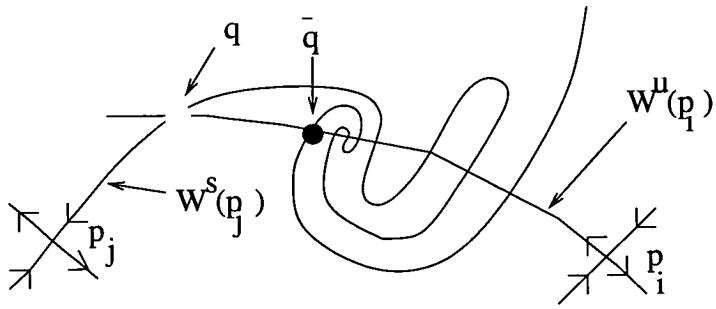

Figure 3.13: Two hyperbolic fixed points showing their stable and unstable manifolds; q is a pip, $\bar{q}$ is not a pip.

Suppose that $S[p_j, q]$ denotes the segment of $W^s(p_j)$ with endpoints p_j and q and $U[p_i, q]$ denotes the segment of $W^u(p_i)$ with endpoints at q and p_i.

Definition

Suppose that $q \in W^s(p_j) \cap W^u(p_i)$ (where p_i may equal p_j). Then q is called a primary intersection point (pip) if $S[p_j, q]$ intersects $U[p_i, q]$ only at the point q (and p_i, if $i = j$) - see fig(3.13).

Definition

Suppose that $q_0, q_1 \in W^s(p_j)$ and that q_0 is closer than q_1 to p_j in the sense of the arclength along $W^s(p_j)$. Then we say that $q_0 <_s q_1$. Similarly, suppose that $q_0, q_1 \in W^u(p_i)$ and that q_1 is closer than q_0 to p_i in the sense of arclength along $W^u(p_i)$. Then we say that $q_1 <_u q_0$.

Definition

Let $q_0, q_1 \in W^s(p_j) \cap W^u(p_i)$ be two adjacent pips, i.e. there are no other pips on $U[q_1, q_0]$ and $S[q_1, q_0]$, the segments of $W^u(p_i)$ and $W^s(p_j)$ connecting q_0 and q_1. Then we refer to the region interior to $U[q_1, q_0] \cup S[q_1, q_0]$ as a lobe - see fig(3.14).

Transport across a Boundary

Suppose $W^s(p_j)$ and $W^u(p_i)$ intersect at the pip q. We should like to discuss the motion of points from region R_1 to region R_2 across the boundary line which is defined by $\mathcal{B} \equiv S[p_j, q] \cup U[p_i, q]$ (see fig(3.15); R_1 and R_2 which lie on either side of $\mathcal{B}$, are used for descriptive purposes only).

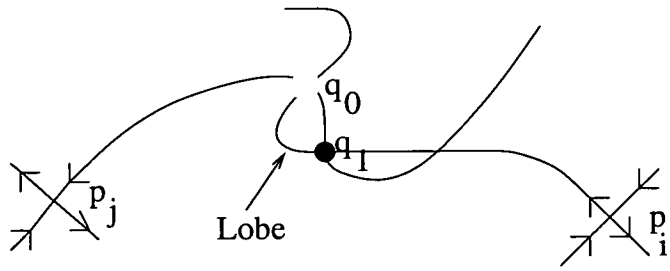

Figure 3.14: The definition of a lobe

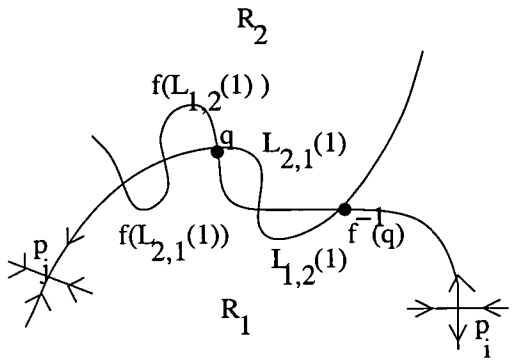

Figure 3.15: Transport between different regions.

Fig(3.15) shows the preimage of q and other points on the stable manifold. Notice that $S[f^{-1}(q), q] \cup U[f^{-1}(q), q]$ forms the boundary of precisely two lobes; one in R_1 labelled $L_{1,2}(1)$, and the other in R_2, labelled, $L_{2,1}(1)$. If these lobes are evolved forward by the iterative function f we see that the lobe $L_{1,2}(1)$ has moved from R_1 into R_2 and that the lobe $L_{2,1}(1)$ has moved from R_2 into R_1. So the only points which can move from region R_1 into R_2 crossing $\mathcal{B}$ are those in $L_{1,2}(1)$. Similarly $L_{2,1}(1)$ contains the points which move from R_2 into R_1 under one iteration. The two lobes $L_{1,2}(1)$ and $L_{2,1}(1)$ have been called a *turnstile* by R.S. MacKay et al(1984).

3.10.2 Turnstile Dynamics

Working within the above mathematical framework Rom-Kedar et al. describe the motion of fluid between regions R_1 and R_2 in fig(3.12). These authors have extended the stable and unstable manifolds in the upper half plane of fig(3.12)

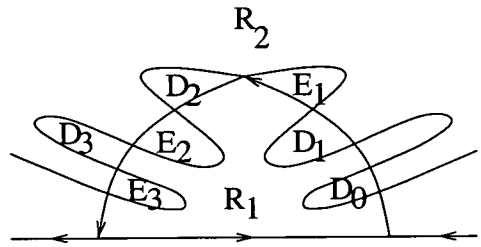

Figure 3.16: The lobe structure.

to reveal more of the structure of the lobes which are shown in fig(3.16). The lobes are labelled E_i and D_i.

We assume that the motion of fluid is governed by a mapping T with the property that

$$T(E_i) = E_{i+1}, \quad T(D_i) = D_{i+1}.$$

Notice that the lobes E_i fall within region R_2 for $i \leq 1$ and within region R_1 for $i > 1$. (The motion of fluid into R_1 is referred to as *entrainment* .) Similarly lobes D_i remain within region R_2 for $i > 0$ and within region R_1 for $i \leq 0$. (The motion of fluid out of R_1 is referred to as *detrainment*.) Lobes D_1 and E_1 form the turnstile. Transport of fluid between R_1 and R_2 is governed by the turnstile.

We return to Hénon's model problem and follow a similar approach to that adopted by Rom-Kedar. Phase space may be separated into two regions as shown in fig(3.17). This partition closely resembles that of fig(3.12).

It is possible to extend the unstable manifold of the left fixed point beyond the point (0,1) in the (X, w) plane (cf. fig(3.16)). The manifold is found to break up into an infinite sequence of disconnected segments as shown in fig(3.18) and fig(3.19). The lobes D_1 and D_1' act as escape lobes, and are responsible for detraining phase space from R_1. They appear as small triangular sections. The lobes E_1 and E_1' are incoming lobes and contain phase space which will enter R_1 on the next iteration of the mapping. The amount of phase space detrained from region R_1 during one iteration of the mapping is equivalent to the combined area of lobes D_1 and D_1'. Setting $D = D_1 \cup D_1'$ we may

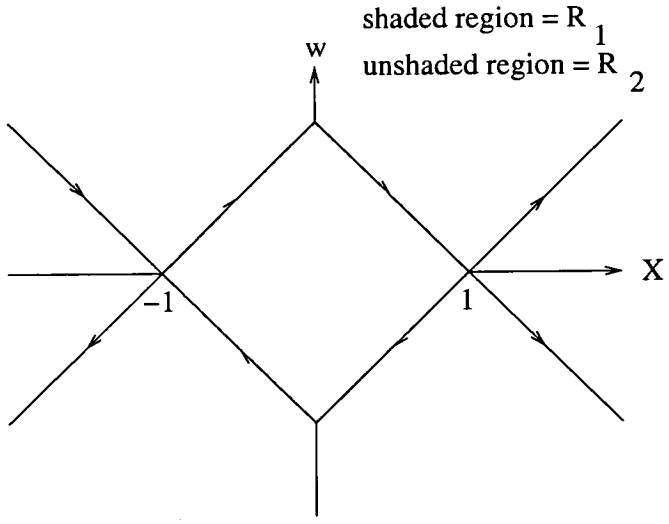

Figure 3.17: The regions R_1 and R_2.

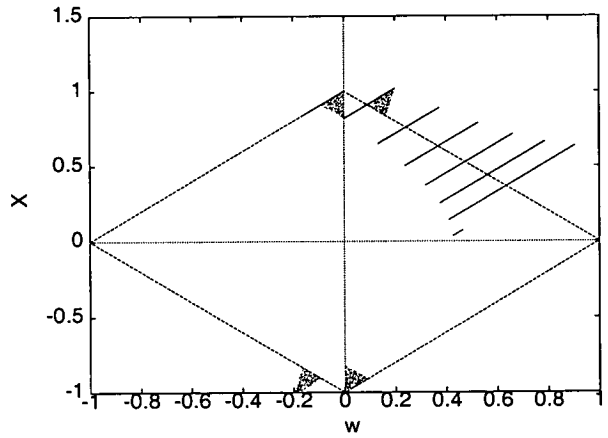

Figure 3.18: Continuation of the left unstable manifold for $e^{\psi} = 1.2$. The lobe at the top left (which we could refer to as an *escape lobe*) is the preimage of the lobe at the top right. It contains phase space which will leave region R_1 and pass into R_2 on the next iteration of the mapping. Another escape lobe exists at the bottom right.

refer to this region as *lobe D* and denote its area by $\mu(D)$. Similarly we may set $E = E_1 \cup E_1'$ and refer to this region as *lobe E*. (The area of these lobes and their precise location in the (X, w) plane is determined in the following section.)

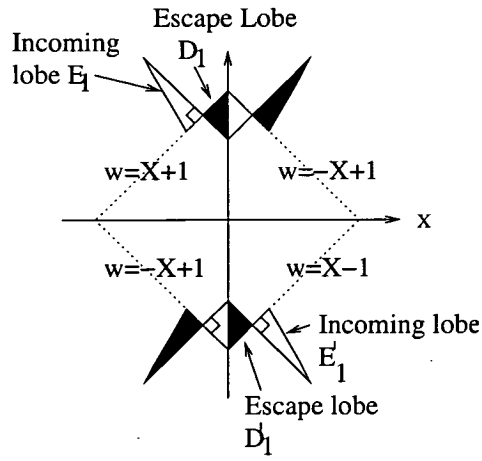

Figure 3.19: The incoming and escape lobes shown schematically.

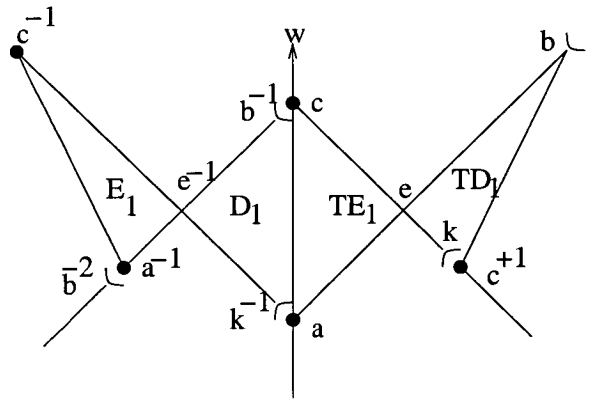

Figure 3.20: Lobes D_1 and E_1 in more detail.

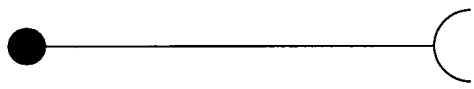

Figure 3.21: This shows a line segment which is closed at its left end point and open at the right end point - see fig(3.20).

3.11 Escape Distributions II

In this section we compute escape distributions analogous to fig(3.10). We should like to know the rate at which phase space, initially in region R_1, escapes into region R_2.

A crude method would be to place an array of grid points across region R_1 measuring the fraction of points still remaining after k (say) iterations. The results of such calculations are presented later in sec(3.11.5). A more efficient method (described in Rom-Kedar, Leonard and Wiggins(1988)) based on turnstile dynamics is to measure how long it takes for phase space, *initially in the incoming lobes*, to escape from R_1. This reduces the amount of computation required since the phase space enclosed within the lobe is much less than the area of region R_1 (assuming ψ is small). We begin by calculating the area of the lobe sections.

3.11.1 Area of the lobe

The area of the lobe sections may be determined analytically as a function of ψ. Fig(3.20) gives a more detailed description of lobes D_1 and E_1. Care must be taken in dealing with the mapping of points near the discontinuity and for this reason we have introduced the simplifying notation described in fig(4.9). Fig (3.21) shows a line segment which is closed at its left end point and open at the right end point.

We begin by calculating the position vectors $\mathbf{a}, \mathbf{e}, \mathbf{b}$ and $\mathbf{k}$ in fig(3.19) :

$$\mathbf{a} = (0, 1 - 2\tanh\frac{\psi}{2}) \tag{3.86}$$

$$\mathbf{e} = (\tanh\frac{\psi}{2}, 1 - \tanh\frac{\psi}{2}) \tag{3.87}$$

$$\mathbf{b} = (e^{\psi} - 1, e^{\psi} - 2\tanh\frac{\psi}{2}) \tag{3.88}$$

$$\mathbf{k} = (1 - e^{-\psi}, e^{-\psi}). \tag{3.89}$$

We shall describe the components of these vectors using the notation $\mathbf{a} = (a_X, a_w)$ etc. It is easily seen that $(\mathbf{k} - \mathbf{e})$ is perpendicular to $(\mathbf{b} - \mathbf{e})$. This

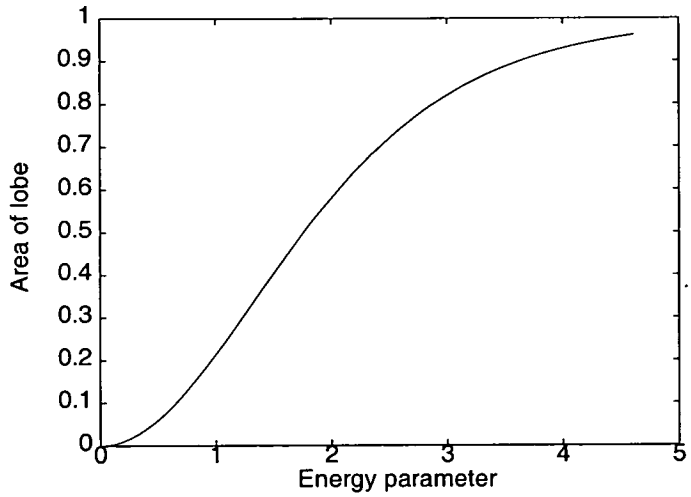

Figure 3.22: Area of lobe, $\mu(D_1)$, against the energy parameter ψ.

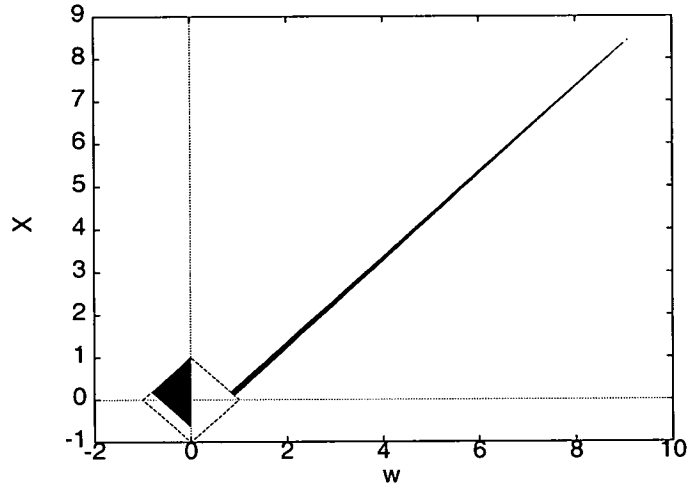

Figure 3.23: The escape lobe D_1 and its image for large ψ.

means that the lobe takes the form of a right angled triangle whose area $\mu(D_1)$ is given by

$$\mu(D_1) = \frac{1}{2}|\mathbf{k} - \mathbf{e}|.|\mathbf{b} - \mathbf{e}| \tag{3.90}$$

Since the mapping is area-preserving this means that all images or preimages of the lobe will have the same area. Fig.(3.22) shows $\mu(D_1)$ as a function of ψ. As $\psi \to \infty$, $\mu(D_1) \to 1$. This is seen by observing that for large ψ the escape lobe will contain nearly all phase space in region R_1 satisfying $X < 0$. Fig(3.23) shows the escape lobe for large ψ.

3.11.2 Escape rates

We now describe the scheme developed by Rom-Kedar for calculating escape distributions and show how it can be applied to Hénon's model problem.

We begin by considering phase space initially in lobe E. (Recall that $E = E_1' \cup E_1$ - see fig(3.19).) After one iteration of the mapping lobe E enters region R_1. However, at some later time, on (say) the $(k-1)$th iteration of the mapping, a portion of the 'image of E' may be found in lobe D and will therefore escape on the next iteration. We define e_k to be that portion, i.e.

e_k = measure of phase space initially in lobe E that escapes region R_1 on the kth iteration.

Clearly,

$$e_k = \mu(T^{k-1}E \cap D), \quad k = 1, 2, \ldots \tag{3.91}$$

and

$$e_k = 0, \quad k \leq 0.$$

where $T^{k-1}E$ is the region obtained by $k-1$ iterations of lobe E.

Instead of evolving lobe E forwards until it intersects lobe D, one could apply the inverse mapping to lobe D since the mapping is area preserving. With this in mind an alternative expression for eqn(3.91) is given by

$$e_k = \mu(E \cap T^{-k+1}D), \quad k = 1, 2, \ldots \tag{3.92}$$

Fig(3.24) illustrates the geometry associated with (3.91). (For simplicity we show only lobe E_1.) Notice that a more general expression exists :

$$e_k = \mu(T^{k+m-1}E \cap T^m D), \quad m = 0, \pm 1, \pm 2, \ldots$$

In fig(3.25) we illustrate the case $m = 0$ by displaying the sets $T^{k-1}E_1 \cap D_1$ for several values of $k - 1 \geq 14$. These sections have been calculated analytically.

We now consider the escape distribution for region R_1 and define escape portions as follows:

Let r_{1k} = area of phase space initially in region R_1 that escapes on the kth iteration of the mapping.

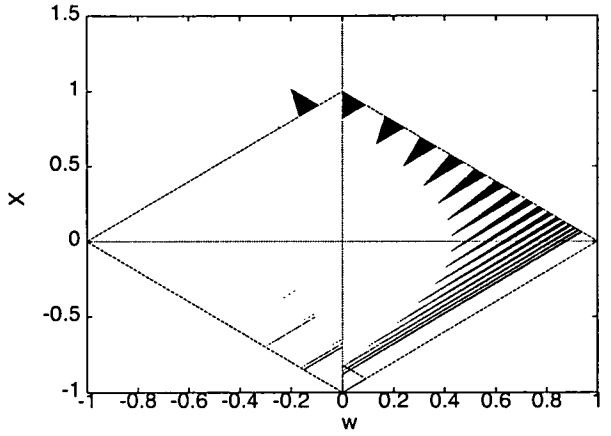

Figure 3.24: The incoming lobe E_1 and $T^{k-1}(E_1)$ for $k = 2, \ldots 17$ ($e^{\psi} = 1.2$). Note that $T^{k-1}(E_1) \cap D_1' = \emptyset$ for $k < 15$. The portions of phase space entering D_1' will escape from region R_1. A similar situation arises in the case of lobe E_1'.

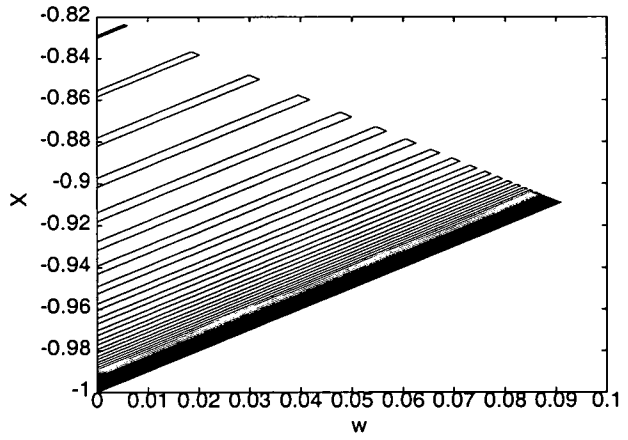

Figure 3.25: An enlargement of fig(3.24) showing $T^{k-1}(E_1) \cap D_1'$ for $k = 15, 16 \ldots$. These results have been obtained analytically - see subsec(3.11.3) - but do not show the full picture. It is possible for phase space to "jump" the escape lobe on its first passage through R_1 but to escape via D_1 or D_1' at some future stage. These contributions are not shown here.

It is clear that the phase space escaping region R_1 on the kth iteration must have been in the lobe $T^{-k+1}D$ at the start. However, not all of $T^{-k+1}D$ was initially in region R_1 since portions of $T^{-k+1}D$ may intersect $T^{-l}E$, $0 \leq l \leq k-2$ and should not be counted. Integer values of l exceeding $k-2$ need not be considered since

$$\mu(D \cap E) = \emptyset$$

and hence

$$\mu(T^{-k+1}D \cap T^{-l}E) = \emptyset, \quad \text{for} \quad l \geq k-1. \tag{3.93}$$

With this in mind it follows that $r_{1k} = \mu(D)$ when $k = 1$ and

$$r_{1k} = \mu(T^{-k+1}D) - \sum_{l=0}^{k-2} \mu(T^{-k+1}D \cap T^{-l}E), \quad k \geq 2 \tag{3.94}$$

where the sum in eqn(3.94) represents the phase space in $T^{-k+1}D$ that is also in some $T^{-l}E$ for $0 \leq l \leq k-2$. Since the mapping is area-preserving we have

$$\begin{aligned} \mu(T^{-k+1}D) &= \mu(D) \\ &= \mu(E) \end{aligned} \tag{3.95}$$

and from eqn(3.92) and the equation following it we have

$$e_{k-l} = \mu(T^{-k+1}D \cap T^{-l}E). \tag{3.96}$$

Using eqns(3.96) and (3.95) allows us to simplify eqn(3.94) as follows:

$$r_{1k} = \mu(E) - \sum_{l=0}^{k-2} e_{k-l}, \quad k \geq 2 \tag{3.97}$$

or (since $e_1 = 0$ from (3.93) and (3.96))

$$r_{1k} = \mu(E) - \sum_{l=1}^{k} e_l. \tag{3.98}$$

To calculate r_{1k} it is therefore only necessary to consider the dynamics of lobe E, namely the e_k.

We may now calculate an expression for the escape distribution in terms of the e_k. Let

$Esc(k)$ = amount of phase space initially in R_1 which remains in R_1 after k iterations of the mapping.

Clearly,

$$Esc(k) = Esc(k-1) - r_{1k} \tag{3.99}$$

or,

$$Esc(k) = \mu(R_1) - \sum_{i=1}^{k} r_{1i}. \tag{3.100}$$

Using (3.98) we obtain

$$Esc(k) = \mu(R_1) - k\mu(E) + \sum_{i=1}^{k}(k-i+1)e_i. \tag{3.101}$$

This escape distribution is more general than the previous one for h-orbits. However, they are related in the sense that the initial conditions for h-orbits represent a 1-dimensional subset of region R_1. Notice that the initial conditions for h-orbits which escape in 1 iteration lie in lobes D_1 and D_1'.

3.11.3 Analytical results

An approximate escape distribution which is valid for small values of k may be calculated analytically from eqn(3.101).

The volume of phase space originally in R_1 which initially escapes into R_2 is given by the combined area, $\mu(E)$, of the escape lobes. After a critical number of iterations we find phase space leaving region R_1 which originated in region R_2. A careful examination of fig(3.24) shows how this situation arises. After 14 iterations it is possible for phase space in the incoming lobe E_1 to escape region R_1 via the escape lobe D_1'. There is therefore an integer M (say), depending on the value of ψ, such that

$$e_k = 0 \quad \text{for} \quad 0 \leq k < M$$

and

$$e_k \neq 0 \quad \text{for} \quad k \geq M.$$

If k is strictly less than M we may replace eqn(3.101) by the linear expression

$$Esc(k) = \mu(R_1) - k\mu(E). \tag{3.102}$$

For $k \geq M$ the summation term in eqn(3.101) is no longer equal to zero and must be taken into consideration. This means that

$$Esc(k) = \begin{cases} \mu(R_1) - k\mu(E) & \text{if} \quad 1 \leq k < M, \\ \mu(R_1) - k\mu(E) + \sum_{i=M}^{k}(k-i+1)e_i & \text{if} \quad k \geq M. \end{cases} \tag{3.103}$$

We apply eqn(3.103) by calculating analytic expressions for M and (approximate) expressions for the e_k as a function of ψ. (The other quantities are known : $\mu(R_1) = 2$ and we use the results of the previous subsection for $\mu(E)$.)

Approximation of e_k for some $k \geq M$.

The e_k may be determined by computing *twice* the area of the sections $T^{k-1}E_1 \cap (D_1 \cup D_1')$ in fig(3.25). This is because

$$\begin{aligned} \mu(T^{k-1}E_1 \cap (D_1 \cup D_1')) &= \frac{1}{2}\mu(T^{k-1}(E_1 \cup E_1') \cap (D_1 \cup D_1')) \\ &= \frac{1}{2}\mu(T^{k-1}E \cap D) \\ &= \frac{1}{2}e_k. \end{aligned}$$

The area of these sections may be determined by calculating the position vectors $\mathbf{s}, \mathbf{p}, \mathbf{q}, \mathbf{r}$ in fig(3.26).

We start by calculating the equation of the line l_2. This line has gradient 1 and passes through the point with position vector $T^n\mathbf{e}$ for some $n \geq k-2$. The line l_1 is formed by applying the forward mapping $(n-1)$ times to the line segment joining $T(\mathbf{a})$ and $\mathbf{k}$ (cf. fig(3.19)). As the line segment becomes discontinuous for $X < 0$ only the (connected) section for which $X \geq 0$ will be considered. For any $n \geq k-2$ these lines will intersect lobe D_1' as shown in fig(3.26).

The next step is to find where lines l_1 and l_2 intersect the line l_3 and the line $X = 0$. Expressions for the position vectors $\mathbf{s}, \mathbf{p}, \mathbf{q}, \mathbf{r}$ may then be obtained. The position vectors $T^{n-1}\mathbf{k}$ and $T^n\mathbf{e}$ may be calculated using the iterative form of the mapping (using eqns(3.89) and (3.87)) :

$$\begin{aligned} T^{n-1}\mathbf{k} &= (k_X^{n-1}, k_w^{n-1}) \\ &= (e^{-(n-1)\psi}(k_X - 1) + 1, e^{-(n-1)\psi}(1 - k_X)) \\ &= (1 - e^{-n\psi}, e^{-n\psi}) \end{aligned} \tag{3.104}$$

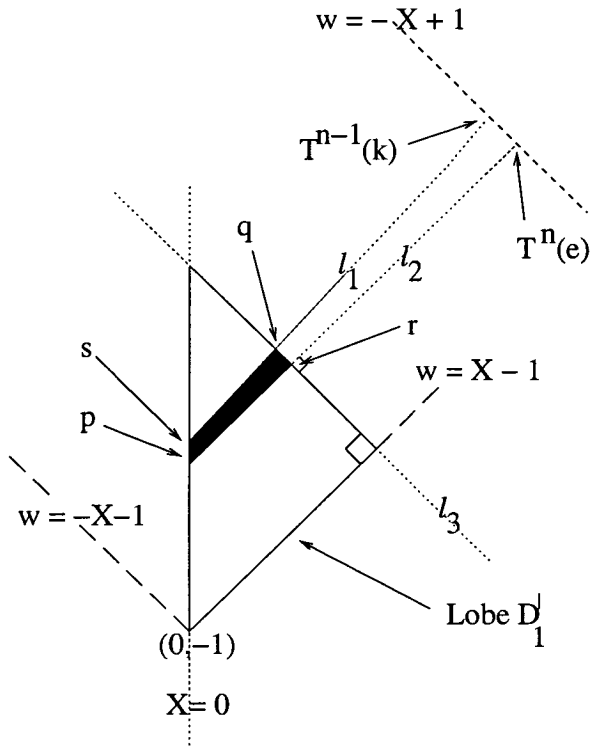

Figure 3.26: $T^{k-1}(E_1) \cap D_1'$ for some $k \geq M$.

$$\begin{aligned} T^n\mathbf{e} &= (e_X^n, e_w^n) \\ &= (e^{-n\psi}(e_X - 1) + 1, e^{-n\psi}(1 - e_X)) \\ &= (e^{-n\psi}(\tanh\frac{\psi}{2} - 1) + 1, e^{-n\psi}(1 - \tanh\frac{\psi}{2})). \end{aligned} \tag{3.105}$$

Two sets of points (parametrised by the integer n) are obtained all of whose members lie on the stable manifold of the right fixed point. A useful observation is that $T^{n-1}\mathbf{k}, T^n\mathbf{e} \longrightarrow (1,0)$ as $n \longrightarrow \infty$.

From (3.105) the equation of line l_2 is given by

$$w = X - 2e^{-n\psi}(e_X - 1) - 1. \tag{3.106}$$

The gradient of the section of line l_1 lying in the region $X \geq 0$ is found by calculating the vector joining $T^n\mathbf{a}$ and $T^{n-1}\mathbf{k}$. Assuming that $T^n\mathbf{a}$ lies in this region it can be shown that

$$m_{l_1} = \coth(n\psi).$$

It is not legitimate to calculate m_{l_1} in this way when $T^n\mathbf{a}$ lies in the region $X < 0$ due to the discontinuities in the line segment. It is, however, this particular case

in which we are interested and it can be shown that the expression for m_{l_1} for the segment $\mathbf{q}-\mathbf{s}$ is still valid even when $T^n\mathbf{a} \in \{X < 0\}$ since we are only interested in the region $X \geq 0$.

The equation of line l_1 is therefore (applying eqn(3.104))

$$w = e^{-n\psi} + \coth n\psi(X - 1 + e^{-n\psi}). \tag{3.107}$$

Line l_3 passes through the point $(0, 2\tanh\frac{\psi}{2} - 1)$ and has gradient -1. Its equation is therefore

$$w = -X + 2\tanh\frac{\psi}{2} - 1.$$

The position vectors are calculated as follows.

$\mathbf{s} = (s_X, s_w)$ is found by setting $X = 0$ in eqn(3.107) :

$$(s_X, s_w) = (0, -\coth n\psi(-1 + e^{-n\psi}) + e^{-n\psi}).$$

$\mathbf{q} = (q_X, q_w)$ is the point at which line l_1 intersects line l_3 :

$$\begin{aligned} q_X &= \frac{2\tanh\frac{\psi}{2} - 1 - e^{-n\psi} - m_{l_1}(e^{-n\psi} - 1)}{m_{l_1} + 1} \\ q_w &= -q_X + 2\tanh\frac{\psi}{2} - 1. \end{aligned}$$

$\mathbf{p}$ is calculated by finding the point at which l_2 cuts $X = 0$:

$$\mathbf{p} = (p_X, p_w) = (0, -2e^{-n\psi}(e_X - 1) - 1).$$

To calculate $\mathbf{r}$ we need the point at which line l_2 intersects line l_3 :

$$\mathbf{r} = (r_X, r_w) = (\tanh\frac{\psi}{2} + e^{-n\psi}(e_X - 1), \tanh\frac{\psi}{2} - e^{-n\psi}(e_X - 1) - 1).$$

Having established the vectors $\mathbf{p}, \mathbf{q}, \mathbf{r}, \mathbf{s}$ analytically as a function of ψ the e_k may be found by calculating (twice) the area of the resulting quadrilateral. The simplest way to do this is to perform a clockwise rotation of $\frac{\pi}{4}$ about the origin and compute the area of the regions L_1, L_2 and L_3 as shown in fig(3.27). These regions take the form of a rectangle and two right angled triangles.

Calculation of M as a function of ψ.

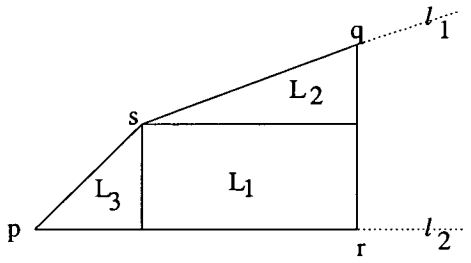

Figure 3.27: The quadrilateral formed by the points with position vectors $\mathbf{p}, \mathbf{s}, \mathbf{q}, \mathbf{r}$.

We should like to know the maximum number of iterations, M, for which the linear approximation in eqn(3.102) is valid. A correction (represented by the summation term in eqn(3.103)) is required when the line l_2 intersects lobe D_1'. M is therefore the smallest integer such that

$$-e^{-(M-2)\psi}(e_X - 1) < \tanh\frac{\psi}{2}$$

or,

$$M > 2 - \frac{1}{\psi}\ln\{\frac{\tanh\frac{\psi}{2}}{1 - e_X}\}. \tag{3.108}$$

When $\psi = \ln(1.2)$ we find that the right hand side of eqn(3.108) is 14.629. We therefore set $M = 15$. A second correction is required when phase space, initially in the incoming lobe E_1, escapes from R_1 via lobe D_1. This situation occurs after about 30 iterations as illustrated in figs(3.28), (3.11.3). An alternative method for arriving at eqn(3.108) would have been to consider the lowest value of n such that $T^n\mathbf{a}$ lies in the region $X < 0$.

The Escape Distribution

In fig(3.30) we present escape distributions based on the above calculations. The two lower curves are calculated from the linear approximation in eqns(3.102) and (3.103) where we set $\psi = \ln 1.2$ for illustration. It is a difficult to compute the e_k analytically for large k due to the stretching of the lobe boundaries. The upper curve in fig(3.30) is generated numerically using a technique developed by Rom-Kedar et al.(1988) which we now describe.

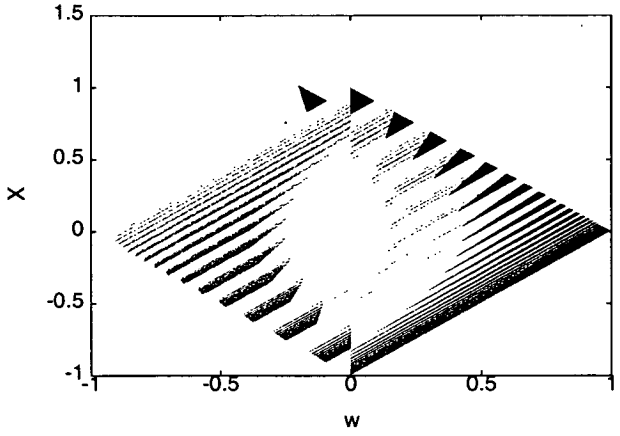

Figure 3.28: The incoming lobe E_1 and $T^n E_1, n = 1, 2 \ldots$

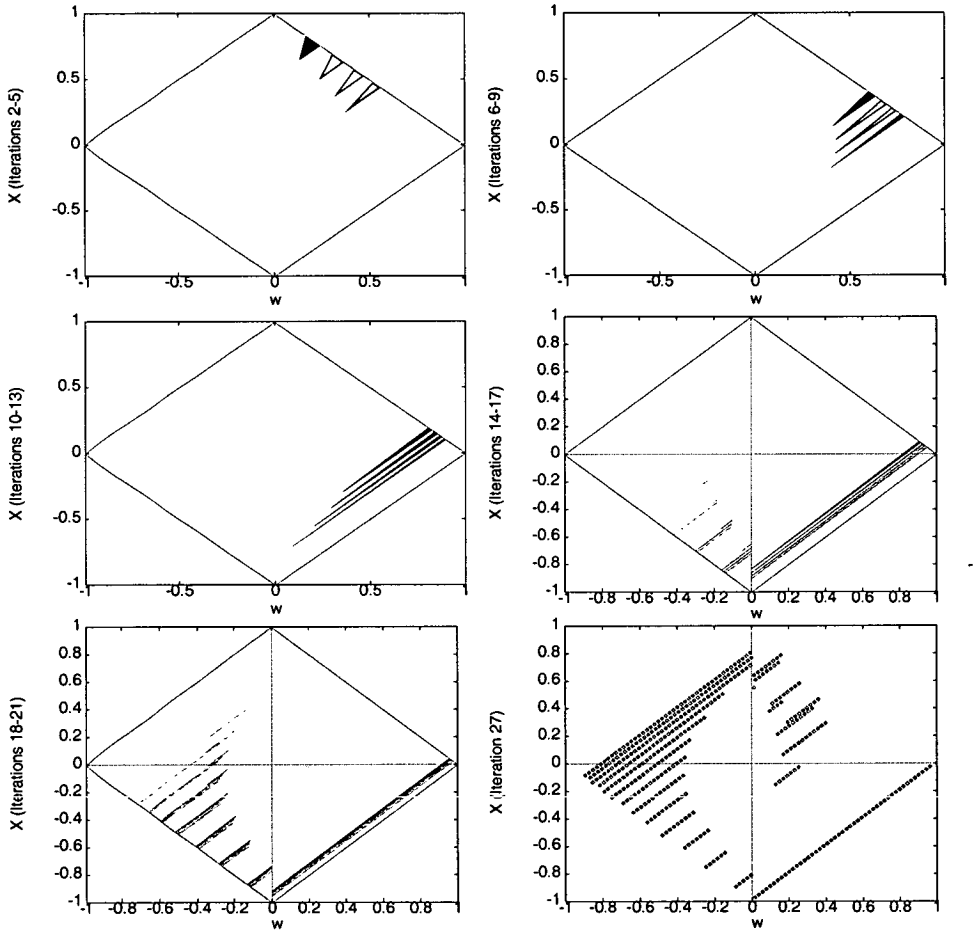

Figure 3.29: A more detailed illustration showing how the lobes undergo stretching. This shows $T^2 E_1 \ldots T^5 E_1, T^6 E_1 \ldots T^9 E_1$ down to $T^{18} E_1 \ldots T^{21} E_1$. The last graph (bottom right) shows $T^{27} E_1$. After 27 iterations phase space originating in lobe E_1 is seen to escape from lobe D_1.

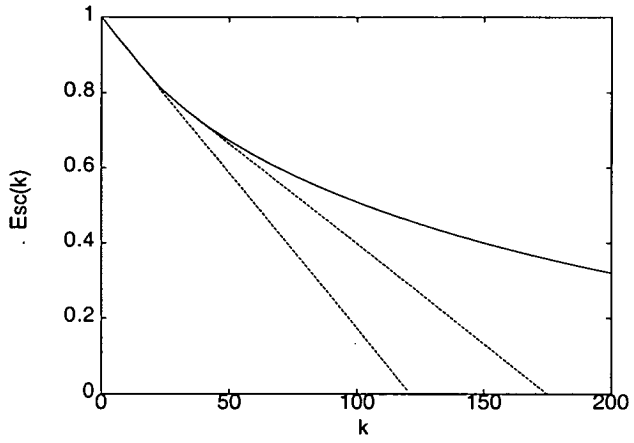

Figure 3.30: The escape distribution based on turnstile dynamics (ie. eqn. (3.101)) compared with the graphs obtained from the linear approximation in eqns(3.102) and (3.103).

3.11.4 Numerical results

The e_k may be determined numerically by placing a grid of points over lobe E_1 and then measuring the fraction of points which escape on the kth iteration. We examine the case in which $\psi = \ln(1.2)$. A grid of mesh width (0.00036×0.00036) containing 63256 points is placed across lobe E_1. (A small gap of 0.00018 is introduced between the boundary of the lobe and the grid points.) If $G(k)$ is the number of grid points leaving region R_1 on the k'th iteration of the mapping then

$$e_k = 2\left(\frac{G(k)}{63256}\right)\mu(D_1').$$

Having calculated the e_k numerically we apply eqn(3.103) directly. Fig(3.30) shows $Esc(k)$ against k and compares the escape distribution generated numerically (upper curve) with the analytical approximations based on eqns(3.102) and (3.103). The analytical approximations agree with the numerical results for small values of k.

For small k the values of e_k obtained from the numerical calculation may be compared with the values obtained from the analytical theory - see fig(3.31). Notice that the e_k are initially zero. This occurs during the time when incoming phase space has not yet reached the escape lobes. When phase space which originated in region R_2 finally begins to escape from lobes D_1 and D_1' the

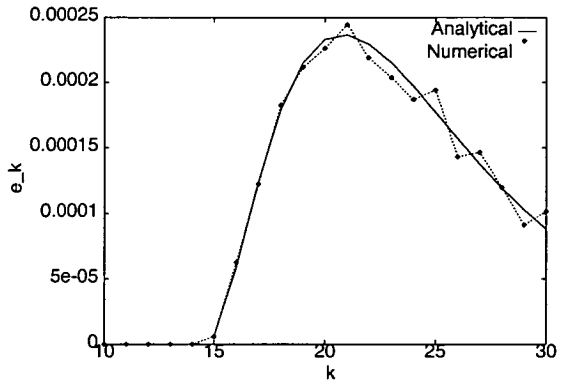

Figure 3.31: e_k against k, comparing the analytical theory with the numerical results.

values of e_k begin to increase. The shape of the graph should be compared with fig(3.25) which indicates that a value of k exists for which e_k is a maximum.

3.11.5 "Brute force" calculation

A straightforward but less elegant method for computing the escape distribution is to fill region R_1 with a large number of points chosen randomly. $Esc(k)$ is (approximately) the fraction of points still remaining after k iterations. Fig(3.32) shows $Esc(k)$ against k and compares the escape distributions obtained from the brute force calculation with the results using turnstile dynamics. (The results from the brute force calculation were obtained by randomly filling region R_1 with 49928 points.) For small k a good match is obtained.

3.12 Summary

We have investigated the escape time distributions for two classes of orbits. The 1-dimensional family of h-orbits was a good starting point and paved the way for a study of orbits with more general initial conditions [3]. In the former case it was possible to use the symbolic representation of the orbit to link the escape

[3] As mentioned earlier the initial conditions for h-orbits represent a 1-dimensional subset of region R_1. It seems possible that the analytical theory, based on the escape distribution for h-orbits, could be extended to cover the case with more general initial conditions. This would form a closer link between secs(3.9) and (3.11).

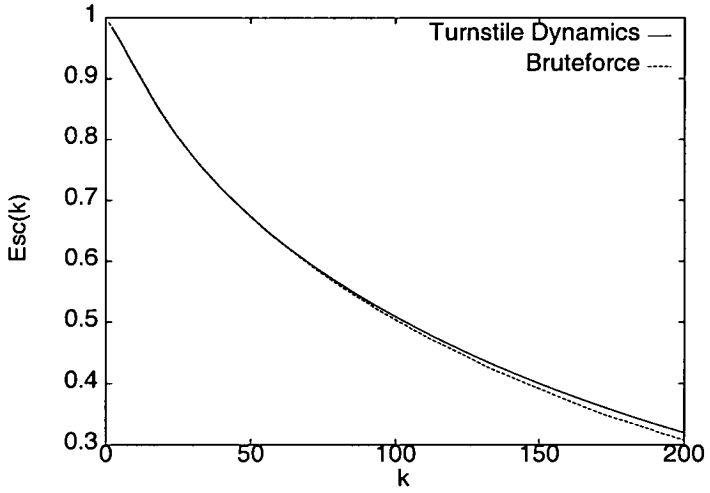

Figure 3.32: Escape distributions comparing the brute force calculation with the results obtained from turnstile dynamics.

time with the initial conditions. In the latter case the mechanism governing the flux of escaping orbits is that of the turnstile. Of critical importance are the manifolds of the left and right fixed points which break up into a series of disconnected segments. The segments intersect each other transversally and form a *tangle*. Within this tangle there are two infinite families of lobes. Any given lobe generates all other lobes in the same family using the forward or inverse mapping.

One lobe in particular will be entrained each time the mapping is applied and, in the other family, there is a lobe that will be detrained. Since the mapping is area-preserving all lobes enclose the same amount of phase space and it this amount that is entrained and detrained during each iteration. Lobes within a given family do not intersect each other. However lobes from one family intersect members from the other family. The areas of intersection may be used to build up an escape distribution. The area formed by the intersecting lobes is most easily computed by tracking a uniform array of grid points placed initially over the lobe due to be entrained on the next iteration of the mapping.

Chapter 4

Globular Clusters and Hill's Problem

4.1 Introduction

The evolution of a star cluster is one of the central problems in stellar dynamics. The aim of this chapter is to investigate the rate at which stars escape from a star cluster. The time scale of escape from star clusters has been investigated by Fukushige and Heggie(2000) and the present study, which extends the work of Christou(1994), aims to deepen our present understanding of this subject. In the following section we describe the problem and outline certain assumptions which are made. Secs(4.2) to (4.4) largely follow the approach of Christou(1994) though the numerical results are completely new. The rest of the chapter is original except where stated otherwise.

The equations describing the motion of a star within a globular cluster are derived using Lagrangian and Hamiltonian methods, and investigated numerically. With given initial conditions, a typical trajectory is analysed by plotting the points at which the orbit intersects a suitably defined surface. In this way, it is possible to visualise the stable and unstable manifolds of the Lyapounov orbits which occur on either side of the cluster.

4.2 Formulation of the problem

It was mentioned in chapter one that the motion of a star within a globular cluster could be described approximately by Hill's equations or some variant of these. In the subsequent derivation, which follows the approach of Chandrasekhar (1942), the galaxy and the cluster are replaced by two point masses M_g and M_c respectively. We assume that the cluster moves in a circular orbit of radius R around the centre of the galaxy with constant angular velocity ω. The mass of the cluster with respect to the galaxy is assumed to be small. Similarly the star's mass is considered to be negligible compared to that of the cluster. We shall focus our attention on the case in which all three bodies lie in the same plane. (The non-coplanar case will be considered later.)

The coordinate system (X_r, Y_r) rotates with angular velocity ω (with respect to the inertial frame (X_i, Y_i)) and is centred on the galaxy as shown in fig(4.1)[1]. At $t = 0$ it is assumed that $X_i = X_r$ and $Y_i = Y_r$. A simple translation relates the coordinate system (ξ, η) to (X_r, Y_r) :

$$X_r = R + \xi, \quad Y_r = \eta.$$

If $\mathbf{r}_r$ and $\mathbf{r}_i$ are the position vectors of the star with respect to the rotating and inertial frames the following relationship holds :

$$\dot{\mathbf{r}}_i = \dot{\mathbf{r}}_r + \boldsymbol{\omega} \times \mathbf{r}_r. \tag{4.1}$$

In the inertial frame of reference the Lagrangian is given by

$$\mathcal{L} = \frac{1}{2}|\dot{\mathbf{r}}_i|^2 - V_g - V_c \tag{4.2}$$

where V_c and V_g are the gravitational potentials due to the cluster and the galaxy. V_g is given by

$$V_g = -\frac{GM_g}{\sqrt{X_r^2 + Y_r^2}} \tag{4.3}$$

where G is the Gravitational Constant and (X_r, Y_r) are the coordinates of the star in the rotating frame. We seek an expression for eqn(4.3) in terms of the

[1]Strictly, this frame is not inertial, as the galaxy rotates about the centre of mass of the entire system, but the resulting error in the final equations of motion is negligible, because the mass of the cluster is assumed to be small

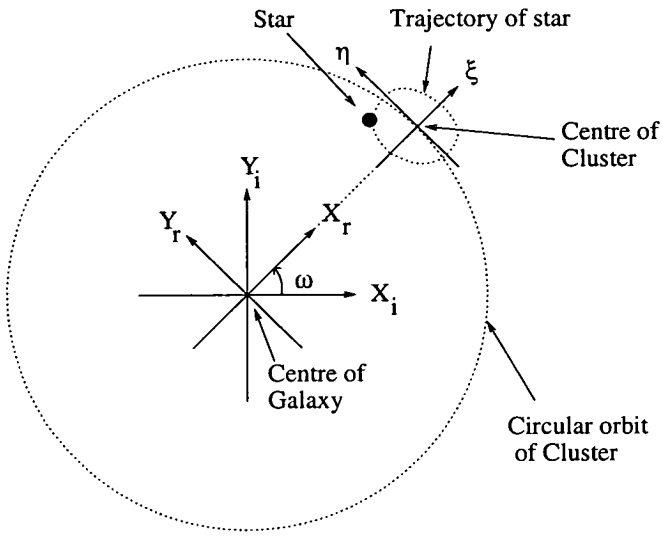

Figure 4.1: The rotating coordinate system.

variables ξ and η. The denominator of eqn(4.3) may be expanded in the form of Taylor's series around the point $X_r = R$, $Y_r = 0$. To second order (omitting the constant term) we find that

$$V_g \approx \omega^2 R\xi - \omega^2\xi^2 + \frac{1}{2}\omega^2\eta^2 \tag{4.4}$$

To arrive at this expression we have assumed Kepler's third law for the two body motion of the cluster about the galaxy. i.e.

$$\omega^2 R^3 \approx GM_g.$$

The Lagrangian may be expressed in terms of ξ and η by substituting the expression in eqn(4.1) for $\dot{\mathbf{r}}_i$ into eqn(4.2). We find that

$$\mathcal{L} = \frac{1}{2}((\dot{\xi} - \eta\omega)^2 + ((\xi + R)\omega + \dot{\eta})^2)$$

$$-\omega^2 R\xi + \omega^2\xi^2 - \frac{1}{2}\omega^2\eta^2 - V_c. \tag{4.5}$$

4.2.1 Hamiltonian Formulation

In the Hamiltonian formulation it is conventional to denote the position variables by q_1, $q_2 \ldots$ and their conjugate momenta by p_1, $p_2 \ldots$. In keeping with

this convention we temporarily denote ξ and η (which we choose as the generalised coordinates) by q_1 and q_2. The p_i are given by

$$p_i = \frac{\partial \mathcal{L}}{\partial \dot{q}_i}, \quad i = 1, 2 \ldots \tag{4.6}$$

¿From eqn(4.6) and eqn(4.5) it is possible to find an expression for the $\dot{q}_i$ in terms of p_i and q_i. We find that

$$p_1 = \frac{\partial \mathcal{L}}{\partial \dot{q}_1} = \dot{q}_1 - q_2\omega$$

$$p_2 = \frac{\partial \mathcal{L}}{\partial \dot{q}_2} = \dot{q}_2 + (q_1 + R)\omega$$

The Hamiltonian, which will be required later, is given (generally) by

$$\mathcal{H} = \sum_{i=1}^{2} p_i \dot{q}_i - \mathcal{L} \tag{4.7}$$

and in our particular case we find that

$$\mathcal{H} = \frac{1}{2}(p_1 + \omega q_2)^2 + \frac{1}{2}(p_2 - \omega(q_1 + R))^2 - \frac{3}{2}\omega^2 q_1^2 + V_c \tag{4.8}$$

where

$$V_c = \frac{GM_c}{r}.$$

(Another constant term has been dropped.)

Lagrange's equations, which are given by

$$\frac{d}{dt}\left(\frac{\partial \mathcal{L}}{\partial \dot{q}_i}\right) = \frac{\partial \mathcal{L}}{\partial q_i}, \quad i = 1, 2, \tag{4.9}$$

yield the following differential equations

$$\ddot{q}_1 - 2\omega\dot{q}_2 - 3\omega^2 q_1 = -\frac{GM_c q_1}{r^3}$$

$$\ddot{q}_2 + 2\omega\dot{q}_1 = -\frac{GM_c q_2}{r^3}. \tag{4.10}$$

These equations describe the motion of the star. The distance from the star to the centre of the cluster is denoted by r.

A more convenient form for these equations exists when distance and time are rescaled. The rescaled variables $\bar{\tau}$, $\bar{q}_i$ and $\bar{r}$ are introduced via the following equations :

$$\bar{\tau} = \omega t, \quad \frac{\omega^2 r^3}{GM_c} = \bar{r}^3, \quad \frac{\omega^2 q_i^3}{GM_c} = \bar{q}_i^3, \quad i = 1, 2.$$

Introducing the original notation and dropping the bars, we see that eqn(4.10) is transformed to give Hill's Equations (see chapter one) :

$$\ddot{\xi} - 2\dot{\eta} - 3\xi = -\frac{\xi}{r^3}$$

$$\ddot{\eta} + 2\dot{\xi} = -\frac{\eta}{r^3}. \tag{4.11}$$

The coordinates (ξ, η) are known as *Hill's coordinates.* Hill's Equations may also be expressed in the following form

$$\ddot{\xi} - 2\dot{\eta} = \Omega_\xi$$

$$\ddot{\eta} + 2\dot{\xi} = \Omega_\eta \tag{4.12}$$

where

$$\Omega = \frac{3}{2}\xi^2 + \frac{1}{r}. \tag{4.13}$$

4.3 Analytical Theory

4.3.1 Equilibrium Points

Two fixed points exist at either side of the cluster at which the resultant force on a test particle is zero. In the rotating frame the force due to the galaxy is cancelled by the force due to the cluster and the centrifugal force. The fixed points are essentially the Lagrangian points L_1 and L_2 of the restricted problem - see chapter one. The coordinates (ξ_0, η_0) of these fixed points are found by setting $\dot{\xi} = \dot{\eta} = 0$ in eqn(4.11). This means that

$$3\xi_0 = \frac{\xi_0}{r^3} = \frac{\xi_0}{(\xi_0^2 + \eta_0^2)^{\frac{3}{2}}}$$

$$0 = \frac{\eta_0}{r^3}.$$

For $\xi_0 > 0$ these equations solve to give

$$(\xi_0, \eta_0) = ((\frac{1}{3})^{\frac{1}{3}}, 0).$$

This will be referred to as the right fixed point. The left fixed point occurs at $(-(\frac{1}{3})^{\frac{1}{3}}, 0)$.

4.3.2 Linearisation around the Equilibrium Points

In order to study the motion near any of these equilibrium points the function Ω in eqn(4.13) may be expanded around (ξ_0, η_0) giving (Szebehely 1967)

$$\Omega = \Omega(\xi_0,\eta_0) + \Omega_\xi(\xi_0,\eta_0)(\xi-\xi_0) + \Omega_\eta(\xi_0,\eta_0)(\eta-\eta_0) + \frac{1}{2!}\Omega_{\xi\xi}(\xi_0,\eta_0)(\xi-\xi_0)^2$$

$$+\Omega_{\xi\eta}(\xi_0,\eta_0)(\xi-\xi_0)(\eta-\eta_0) + \frac{1}{2!}\Omega_{\eta\eta}(\xi_0,\eta_0)(\eta-\eta_0)^2 + \mathcal{O}(3).$$

The differential equations of motion in eqn(4.12) then become

$$\ddot{\xi} - 2\dot{\eta} = \Omega_{\xi\xi}(\xi_0,\eta_0)(\xi-\xi_0) + \Omega_{\xi\eta}(\xi_0,\eta_0)\eta + \mathcal{O}(2),$$

$$\ddot{\eta} + 2\dot{\xi} = \Omega_{\xi\eta}(\xi_0,\eta_0)(\xi-\xi_0) + \Omega_{\eta\eta}(\xi_0,\eta_0)\eta + \mathcal{O}(2). \tag{4.14}$$

¿From eqn(4.13) it is easy to compute $\Omega_{\xi\xi}$, $\Omega_{\eta\eta}$ and $\Omega_{\xi\eta}$. We find that

$$\Omega_{\xi\xi} = 3 + \frac{2\xi^2-\eta^2}{r^5}, \quad \Omega_{\eta\eta} = \frac{2\eta^2-\xi^2}{r^5}, \quad \Omega_{\xi\eta} = \frac{3\xi\eta}{r^5}.$$

This means that

$$\Omega_{\xi\xi}(\xi_0,\eta_0) = 9, \quad \Omega_{\eta\eta} = -3, \quad \Omega_{\xi\eta} = 0.$$

The linearised equations in the neighbourhood of the equilibrium points (also known as the *variational equations*) are therefore given by

$$\ddot{\xi} - 2\dot{\eta} = 9(\xi-\xi_0)$$

$$\ddot{\eta} + 2\dot{\xi} = -3\eta. \tag{4.15}$$

The new variables $x_1 = \xi - \xi_0$, $x_2 = \dot{\xi}$, $x_3 = \eta$, $x_4 = \dot{\eta}$ may be introduced in eqns.(4.15) to reduce the system from a set of two second order differential equations to a set of four first order equations. We therefore obtain

$$\begin{aligned} \dot{x_1} &= x_2 \\ \dot{x_2} &= 9x_1 + 2x_4 \\ \dot{x_3} &= x_4 \\ \dot{x_4} &= -2x_2 - 3x_3. \end{aligned} \tag{4.16}$$

We try a solution to eqn(4.15) as a sum of terms of the form :

$$\xi = \xi_0 + ae^{kt}, \quad \eta = be^{kt}$$

This expression is then substituted into eqn(4.15) to form the characteristic equations

$$(k^2 - 9)a - 2kb = 0$$

$$2ka + (k^2 + 3)b = 0. \tag{4.17}$$

From this equation we may calculate the eigenvalues, k, and eigenvectors, (a, b), of the system. Non-trivial eigenvectors are obtained when the determinant of this 2×2 system is zero. This means that the eigenvalues satisfy the polynomial equation

$$k^4 - 2k^2 - 27 = 0.$$

This polynomial has four roots; two real and two imaginary (cf. Marchal 1990). The real roots are given by

$$k = \pm(1 + 2\sqrt{7})^{\frac{1}{2}} \text{ or } k = \pm k_1 \text{ where } k_1 = 2.50828679\ldots$$

and the imaginary roots are given by

$$k = \pm i(2\sqrt{7} - 1)^{\frac{1}{2}} \text{ or } k = \pm ik_2 \text{ where } k_2 = 2.07159422\ldots.$$

The eigenvectors are found by substituting the eigenvalues $(\pm k_i, \ i = 1, 2)$ into eqn(4.17). We find that when

$$k = \pm k_1, \quad \frac{b}{a} = \mp\frac{4 - \sqrt{7}}{\sqrt{1 + 2\sqrt{7}}} = \mp 0.53990983\ldots$$

and when

$$k = \pm k_2 i, \quad \frac{b}{a} = \pm\frac{4 + \sqrt{7}}{\sqrt{2\sqrt{7} - 1}} = \pm 3.208037192i \text{ (approx)}. \tag{4.18}$$

Taking

$$a_1 = a_2 = 1, \quad b_1 = -\frac{4 - \sqrt{7}}{\sqrt{1 + 2\sqrt{7}}} \text{ and } b_2 = \frac{4 + \sqrt{7}}{\sqrt{2\sqrt{7} - 1}}$$

the general solution to eqn(4.15) is given by

$$\begin{aligned}
\xi &= \xi_0 + c_1 e^{k_1 t} + c_2 e^{-k_1 t} + A\cos(k_2 t - \alpha) \\
\dot{\xi} &= c_1 k_1 e^{k_1 t} - c_2 k_1 e^{-k_1 t} - A k_2 \sin(k_2 t - \alpha) \\
\eta &= c_1 b_1 e^{k_1 t} - c_2 b_1 e^{-k_1 t} - A b_2 \sin(k_2 t - \alpha) \\
\dot{\eta} &= c_1 k_1 b_1 e^{k_1 t} + c_2 k_1 b_1 e^{-k_1 t} - A k_2 b_2 \cos(k_2 t - \alpha). \qquad (4.19)
\end{aligned}$$

In these equations c_1, c_2, A, α are arbitrary constants defined by the initial conditions.

4.3.3 The limiting curves.

Attention will be focussed on the region surrounding the right fixed point (ξ_0, η_0). Taking (ξ_0, η_0) as the origin Hill's equations may be rewritten with respect to this point by replacing ξ by $\xi + \xi_0$ in eqn(4.11). We therefore consider the following system :

$$\begin{aligned}
\ddot{\xi} - 2\dot{\eta} - 3(\xi + \xi_0) &= -\frac{(\xi + \xi_0)}{r^3} \\
\ddot{\eta} + 2\dot{\xi} &= -\frac{\eta}{r^3} \qquad (4.20)
\end{aligned}$$

where $r = \sqrt{(\xi + \xi_0)^2 + \eta^2}$. Initial conditions are chosen on the surface $\eta = 0$. For a given value of the Hamiltonian, we need only specify ξ_{init} and $\dot{\xi}_{init}$ as the value of $\dot{\eta}_{init}$ is determined from the Hamiltonian (expressed in terms of ξ, $\dot{\xi}$, $\dot{\eta}$ with $\eta = 0$). From eqn(4.8) (after scaling) we find that

$$H = \frac{1}{2}(\dot{\xi}^2 + \dot{\eta}^2) - \frac{3}{2}(\xi + \xi_0)^2 - \frac{1}{|\xi + \xi_0|} \qquad (4.21)$$

This equation imposes restrictions on the regions of phase space to which the star has access (see chapter one). These restrictions show the limit of the accessible region and may be thought of as *limiting curves (lc)* in $(\xi, \dot{\xi})$ space - see fig.(4.2). On one side of the curve $\dot{\eta}$ is imaginary. Motion is only permissible on the other side (for which $\dot{\eta}$ is real) or if the particle lies *on* the curve $\dot{\eta} = 0$.

If the value of the Hamiltonian is less than some critical threshold H_{crit} the star can not escape and remains constrained within a closed lc around the centre of the cluster. If $H > H_{crit}$ the lc's open out giving way to an escape channel.

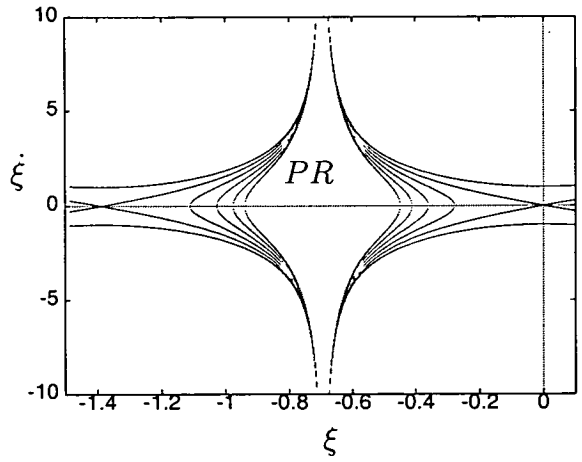

Figure 4.2: The limiting curves in $(\xi, \dot{\xi})$ space. The permissible region (PR) indicates the side of the curve for which $\dot{\eta}$ is real.

The value of H_{crit} may be computed by setting $\xi = \dot{\xi} = \dot{\eta} = 0$ in eqn(4.21). We find that

$$H_{crit} = -\frac{3}{2}(\xi_0)^2 - \frac{1}{|\xi_0|} = -\frac{3^{\frac{4}{3}}}{2} = -2.16337435546111\ldots$$

4.3.4 An approximate relationship between A and $H - H_{crit}$

It was pointed out earlier that two equilibrium points exist on either side of the cluster which are characterised by the fact that if a test particle is placed at rest (i.e. $\dot{\xi} = \dot{\eta} = 0$) at these points it will remain there indefinitely. These equilibria occur when $H = H_{crit}$. Among the set of solutions emanating from the equilibrium point (when H increases beyond H_{crit}) is a family of periodic orbits called *Lyapounov Orbits.* The Lyapounov orbits in Hill's problem are discussed in Spirig and Waldvogel(1991).

The solution to the linearised system indicates the approximate behaviour of orbits near the equilibrium points. The main components of the solution in eqn(4.19) are the periodic parts which correspond to the Lyapounov orbit and the exponentially increasing and decreasing terms, which correspond to the unstable and stable manifolds of this orbit.

The Lyapounov orbit (which is confined to the hypersurface $H = cons$)

gives rise to a fixed point on the surface of section defined by $\eta = 0$. When the orbit is combined with the component associated with the unstable manifold we obtain a line segment, parametrised with coordinates $(\xi, \dot{\xi})$. (This shall be shown later.) The position of the fixed point may be determined approximately from an inspection of eqns. (4.19). Our attention is restricted to the periodic term and we disregard the influence of the stable and unstable manifolds by setting $c_1 = c_2 = 0$. The condition $\eta = 0$ is satisfied by allowing

$$t = \frac{\alpha + 2\pi}{k_2}.$$

Bearing in mind the shift of origin of ξ we find that

$$\xi = A, \quad \dot{\xi} = 0, \quad \eta = 0.$$

If we insist that $\dot{\eta} > 0$ the sign of A will be negative and this implies that the fixed point will lie to the left of the equilibrium point. It moves further to the left as the value of the Hamiltonian increases.

An approximate relationship exists between A and $H - H_{crit}$. It may be found by expanding $H - H_{crit}$ about the fixed point and then substituting the expression for the Lyapounov orbit in eqn(4.19) (setting $c_1 = c_2 = 0$ and $t = \frac{\alpha+2\pi}{k_2}$). Thus,

$$\begin{aligned} H - H_{crit} &= \left\{ \frac{1}{2}(\dot{\xi}^2 + \dot{\eta}^2) - \frac{3}{2}(\xi + \xi_0)^2 - \frac{1}{|\xi + \xi_0|} \right\} + \frac{3}{2}\xi_0^2 + \frac{1}{|\xi_0|} \quad \text{by eqn(4.21)} \\ &= \frac{1}{2}(\dot{\xi}^2 + \dot{\eta}^2) - \frac{9}{2!}\xi^2. \end{aligned} \tag{4.22}$$

and so

$$\begin{aligned} 2(H - H_{crit}) &\approx A^2 k_2^2 b_2^2 - 9A^2 \\ &\approx 35.16601049A^2. \end{aligned} \tag{4.23}$$

It must be stressed that this relationship is only approximately true within the vicinity of the fixed point. As H increases beyond H_{crit} the Lyapounov orbit begins to deviate from the solution in eqn(4.19). This means that it is only legitimate to calculate the fixed point on the surface of section using eqn(4.23) when A is reasonably small.

4.4 Numerical Investigation

The analysis of sec(4.3.2) is valid only in the vicinity of the Lagrangian point. Elsewhere numerical methods may be used, i.e. the equations of motion governing the star are integrated numerically. This yields the orbital trajectories in phase space. A typical orbit may, however, be analysed by recording the points, in $(\xi, \dot{\xi})$ space, at which the orbit intersects the surface $\eta = 0$ in the positive direction, i.e. with $\dot{\eta} > 0$. (Since the orbit lies on the hypersurface $H = cons$, $\dot{\eta}$ is determined from the Hamiltonian.) Hénon(1970) refers to this as a *positive crossing*. A periodic orbit, for example, would manifest itself as a fixed point on the surface. In general, a four dimensional trajectory is now represented by a set of points in the $(\xi, \dot{\xi})$ plane and the results can be represented in a much more compact manner. This approach reveals the most interesting properties of the trajectory.

Two NAG library routines, D02BHF and D02BDF are used throughout this study. The first integrates the equations of motion forward in time thereby enabling the star's trajectory to be plotted in phase space. The second integrates the equations until some condition is satisfied. Using this latter subroutine it is possible to construct a set of iterates on the Poincaré surface $\eta = 0$.

4.4.1 The stable and unstable manifolds.

It was mentioned in chapter 1 that two tube-like structures, responsible for the entrainment and detrainment of phase space, were attached to either side of the cluster. The surfaces of these structures, which are of fundamental importance in understanding the escape phenomenon, are equivalent to (parts of) the stable and unstable manifolds of the Lyapounov orbits. The solution to the linearised system eqn(4.19), with $c_2 = 0$, consists of two time-dependent components, an exponential term and an oscillatory term. The combined influence of these terms mean that trajectories which join the Lyapounov orbit on the stable manifold will spiral in $(\xi, \dot{\xi}, \eta)$ space. The "tube" may be envisaged by allowing the phase angle to vary. Fig(4.6) shows the (right) stable manifold of the Lyapounov

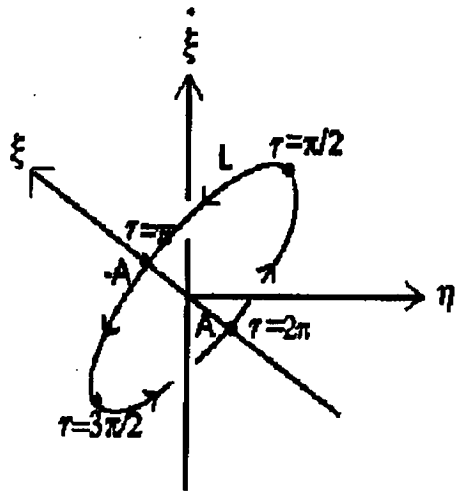

Figure 4.3: The Lyapounov orbit in $(\xi, \dot{\xi}, \eta)$ space.

orbit (at a fixed value of H) in $(\xi, \dot{\xi}, \eta)$ space. The manifold takes the form of a tubular surface (cf. fig 1.7), S, whose appearance in $(\xi, \dot{\xi}, \eta)$ space near the Lyapounov orbit L, can be inferred from the linearisation in eqns(4.19). We can then use this to explain the line segments (which arise from the intersection of the stable and unstable manifolds with the surface of section $\eta = 0$) in fig(??). The following analysis, which focuses on the unstable manifold, can be easily extended to deal with the unstable manifold.

For L, the Lyapounov orbit itself, we set $c_1 = c_2 = 0$ in eqns(4.19). Writing $\tau = k_2 t - \alpha$, L is the parametrised ellipse

$$\begin{pmatrix} \xi \\ \dot{\xi} \\ \eta \end{pmatrix} = A \begin{pmatrix} \cos\tau \\ -k_2 \sin\tau \\ -b_2 \sin\tau \end{pmatrix}, \quad \text{where} \quad 0 \leq \tau < 2\pi,$$

which lies in the plane $\eta = (b_2/k_2)\dot{\xi}$. This is illustrated in fig(4.3), in which the ξ-axis is to be viewed as coming towards the reader, and we recall that $A < 0$. For future purposes, we have elected to view the ellipse from "below" the plane $\dot{\xi} = 0$.

In this space, the unstable manifold is locally the parametrised surface

$$S: \begin{pmatrix} \xi \\ \dot{\xi} \\ \eta \end{pmatrix} = c_1 e^{k_1 t} \begin{pmatrix} 1 \\ k_1 \\ b_1 \end{pmatrix} + A \begin{pmatrix} \cos\tau \\ -k_2 \sin\tau \\ -b_2 \sin\tau \end{pmatrix}, \tag{4.24}$$

where $\tau = k_2 t - \alpha$. Since the surface S is obtained by varying t and α independently, it may equally be viewed as varying t and τ independently, so that near the Lyapounov orbit, the unstable manifold emanates from each point of the orbit in the direction

$$\begin{pmatrix} 1 \\ k_1 \\ b_1 \end{pmatrix},$$

and we recall that $k_1 \approx 2.51$ and $b_1 \approx -0.54$. We observe that this has a negative η component, so that for the portion of L lying in $\eta > 0 (< 0)$, the adjacent part of S extending towards the plane $\eta = 0$ corresponds to $c_1 > 0 (< 0)$. $c_1 > 0$ corresponds to the left unstable manifold of L and $c_1 < 0$ to the right. We consider the latter only in explaining (one of) the curves shown in fig(4.7), and we note that for this portion of L, τ lies in the interval $(\pi, 2\pi)$. Then, adjoining line segments parallel to $-(1, k_1, b_1)^t$ to each point of L lying in $\eta < 0$ gives the surface illustrated in fig(4.4) which is shown extended as far as the plane $\eta = 0$; the curve of intersection of the surface with $\eta = 0$ is termed Γ.

The section Γ where the surface meets $\eta = 0$ may be calculated by setting $\eta = 0$ in eqn(4.24). Then for each τ, the corresponding t value satisfies

$$b_1 c_1 e^{k_1 t} - A b_2 \sin\tau = 0,$$

so that

$$c_1 e^{k_1 t} = \frac{b_2 A}{b_1} \sin\tau \tag{4.25}$$

and hence the section is

$$S: \begin{pmatrix} \xi \\ \dot{\xi} \end{pmatrix} = A \begin{pmatrix} \frac{b_2}{b_1} \sin\tau + \cos\tau \\ \frac{k_1 b_2}{b_1} \sin\tau - k_2 \sin\tau \end{pmatrix}, \quad \pi < \tau < 2\pi,$$

which would describe an ellipse if τ ran over the whole interval $[0, 2\pi)$. Eqn(4.25) and (4.19) also show that on Γ

$$\dot{\eta} = A b_2 (k_1 \sin\tau - k_2 \cos\tau).$$

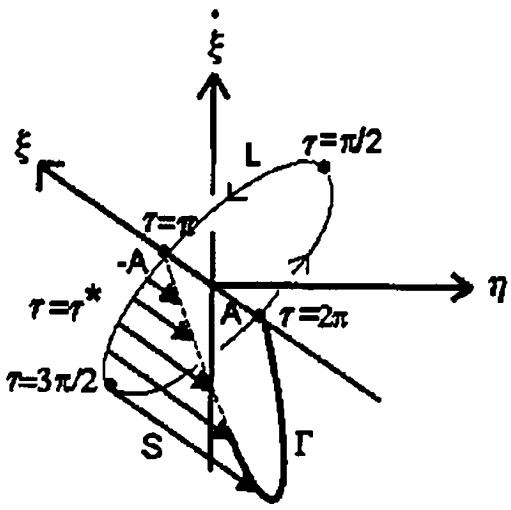

Figure 4.4: Part of the right unstable manifold of L, extending from L to the plane $\eta = 0$, which it intersects in the curve Γ.

(A little care is needed here: $\dot{\eta}$ is the rate of change of η along an orbit; it is not the partial derivative with respect to t, at constant τ, of the expression for η in eqn(4.24) because τ depends on t.) Since $Ab_2 < 0$

$$\dot{\eta} > 0 \iff k_1 \sin\tau - k_2 \cos\tau < 0.$$

Since $\pi < \tau < 2\pi$ on Γ, it then follows that $\dot{\eta} > 0$ on that part of Γ for which

$$\tau^* < \tau < 2\pi,$$

where

$$\tau^* = \pi + \arctan(k_2/k_1).$$

In fig(4.4) the portion of Γ for which $\tau \in (\tau^*, 2\pi)$ is shown solid, and the remainder broken. This corresponds precisely with the section shown in fig(4.7). The point of Γ with $\tau = \tau^*$ has $\dot{\eta} = 0$ and at such a point an orbit touches the limiting. Thus this point of Γ touches the limiting curve, again as shown in fig(4.7).

If the right unstable manifold is extended further in $(\xi, \dot{\xi}, \eta)$ space, then it yields a surface which is shown schematically in fig(4.5). In contrast with the

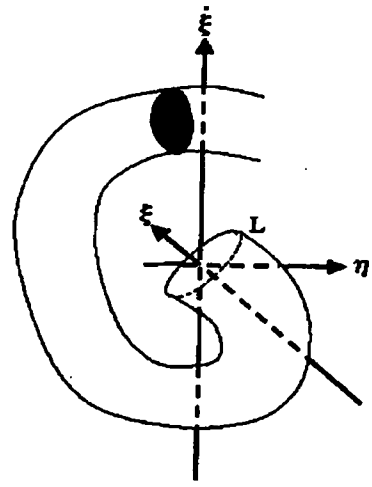

Figure 4.5: Schematic representation of the first Poincaré section of the unstable manifold of L with $\dot{\eta} > 0$.

section, Γ, shown in fig(4.7) it is the intersection of the *whole* tube with $\eta = 0$ (and with $\dot{\eta} > 0$) that is shown in fig(4.5) and in the figures following fig(4.7).

The right unstable manifold may be generated numerically by choosing a set of points (with $\dot{\eta} > 0$) on the line segment Γ and then evolving these points forward in time. When $\tau \approx 2\pi$, Γ takes the form of a straight line whose parametrisation is given as follows:

$$\xi = A(\frac{b_2\tau}{b_1} + 1) \tag{4.26}$$

$$\dot{\xi} = \tau(\frac{k_1 b_2}{b_1} - k_2) \tag{4.27}$$

This is the parametric form of a line in $(\xi, \dot{\xi})$ space. A set of initial conditions on a segment of this line near the fixed point $(\xi = A, \dot{\xi} = 0, \eta = 0)$ may be chosen by varying the value of τ. Eqns(4.27) and (4.26) are useful for numerical purposes.

Determination of A

As before we consider the Lyapounov orbit emanating from the Lagrangian point on the right of the cluster. The Lyapounov orbit manifests itelf as a fixed

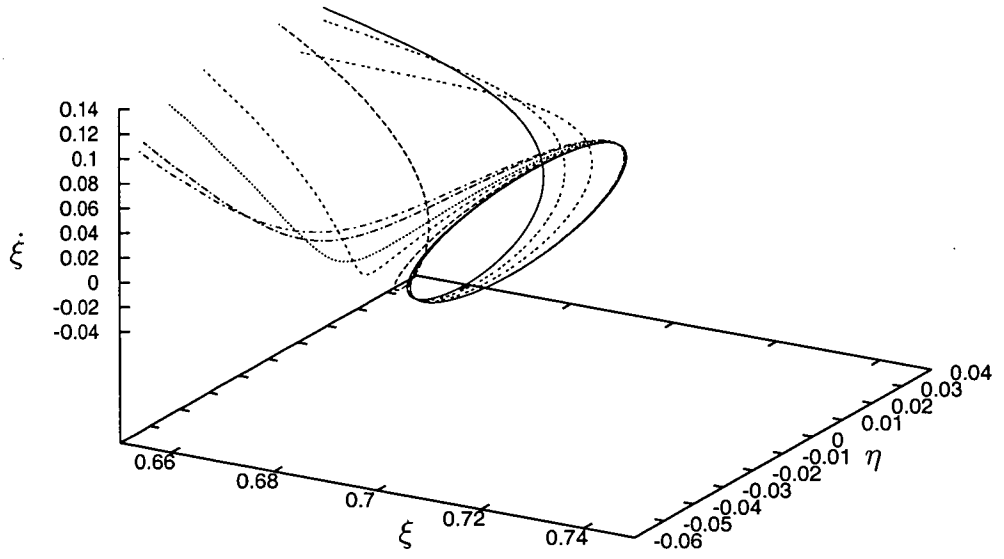

Figure 4.6: This shows a one-parameter family of orbits approaching the Lyapounov orbit (at different "phases"). In phase space the set of all such orbits (at a fixed value of H) forms a tubular surface. Shown here are the final section of several orbits in coordinates ξ, $\dot{\xi}$, η where the centre of the cluster is assumed to lie at the origin (after Fukushige and Heggie 2000).

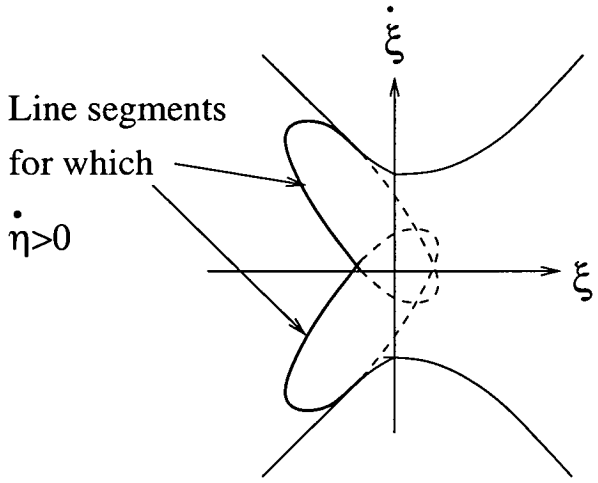

Figure 4.7: This shows (schematically) the projection of the (right) stable and unstable manifold near the Lagrangian point. Each projection gives rise to an ellipse in $(\xi, \dot{\xi})$ space. However, we focus attention on the the bold continuous line segments which satisfy $\dot{\eta} > 0$. The "tube" is generated numerically by choosing points on these segments. (The figure also shows where the limiting curves lie in relationship to the line segments.)

point on the surface of section $\eta = 0$. We now *define* A to be the ξ-coordinate of the fixed point, at $\xi = A$, $\dot{\xi} = 0$ approximately. The fixed point lies on the left of the Lagrangian point, shown schematically in fig(4.8). In this case $A < 0$ and is determined from eqn(4.23).

For a given value of $H(> H_{crit})$, A may be determined approximately from eqn(4.23). To determine A precisely a small corrective term is required. The sign of this corrective term may be established by integrating the orbit with initial conditions

$$\xi = A, \quad \dot{\xi} = 0, \quad \eta = 0.$$

(Note that $\dot{\eta}$ is determined from eqn(4.21) and that the origin is assumed to be at the Lagrangian point on the right of the cluster.) If the approximation lies to the right of the true fixed point the particle will be swept along an escaping trajectory. If it lies to the left of the fixed point the particle will be carried towards the centre of the cluster - see fig(4.8). In the former case a negative correction is required; the latter case requires a positive correction. A bisection

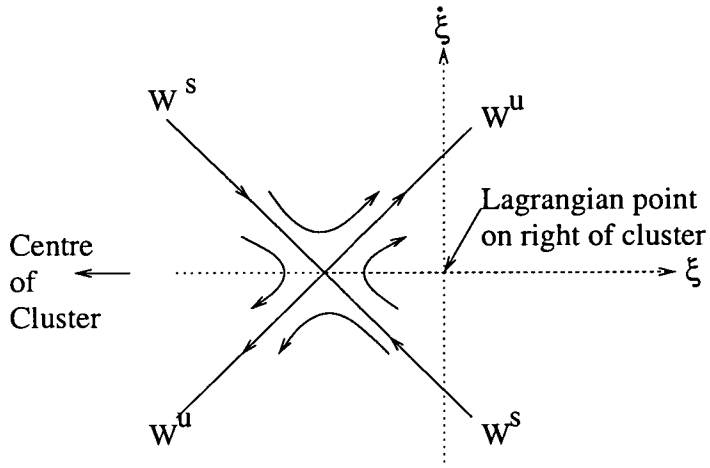

Figure 4.8: The region around the fixed point in the surface of section $\eta = 0$, $\dot{\eta} > 0$. The line segment is used to generate initial conditions for the right unstable manifold.

algorithm can be implemented to determine A to a given accuracy.

Numerical results

Figs(4.10) and (4.11) show the *left* unstable manifold (i.e. the unstable manifold of the left Lagrangian point at $\xi = -2\xi_0$) as it intersects the surface of section $\eta = 0, \dot{\eta} > 0$. Figs(4.12) and (4.13) show the right unstable manifold, ie. the unstable manifold of the fixed point near $\xi = 0$. The corresponding *stable* manifolds are shown in figs(4.14) and (4.15). These plots were obtained by reflecting figs(4.10) and (4.12) in the line $\dot{\xi} = 0$. This is legitimate since eqns(4.11) have the obvious symmetry $\xi \rightarrow \xi$, $\eta \rightarrow -\eta$, $t \rightarrow -t$ which implies that $\dot{\eta} \rightarrow \dot{\eta}$ and $\dot{\xi} \rightarrow -\dot{\xi}$.

These rather complicated diagrams, which bear little resemblance to any conventional homoclinic tangle (cf. fig 1.5), require some explanation.

As expected, near the fixed points (close to $\xi = -2\xi_0$ and $\xi = 0$) the manifolds appear as line segments on the surface of section. Let us focus attention on the region around $\xi = 0$ in figs(4.12) and (4.15). The line segments in this region are shown in more detail in fig(4.9).

Notice that at some distance from the fixed point the line segments begin

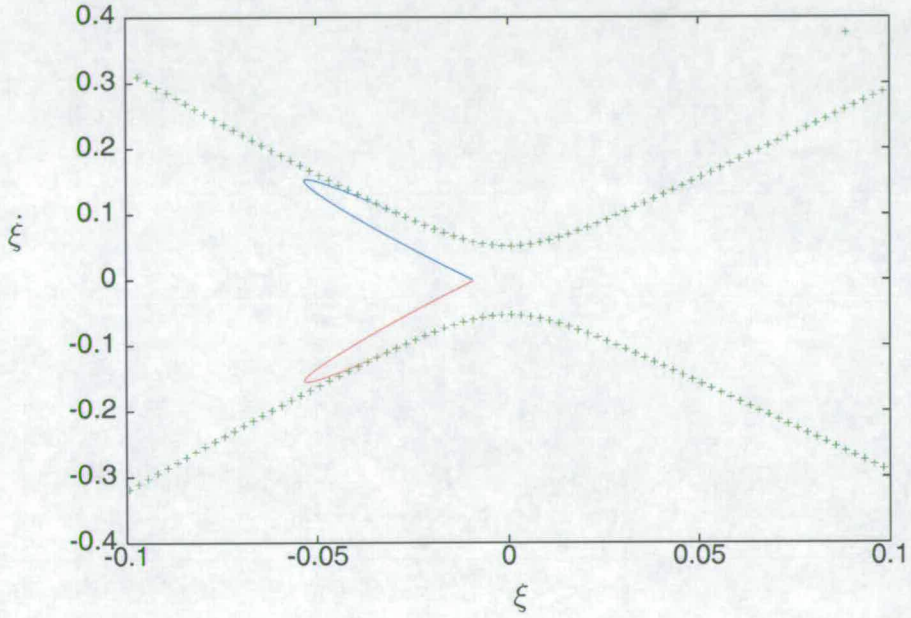

Figure 4.9: This shows the right unstable and stable manifolds in $(\xi, \dot{\xi})$ space near the Lagrangian point. The unstable manifold is shown in red and is a magnification of the region around $\xi = 0$ in fig(4.12). The blue curve represents the stable manifold (cf. fig(4.15)) and the green crosses represent the limiting curves (cf. fig(4.7)).

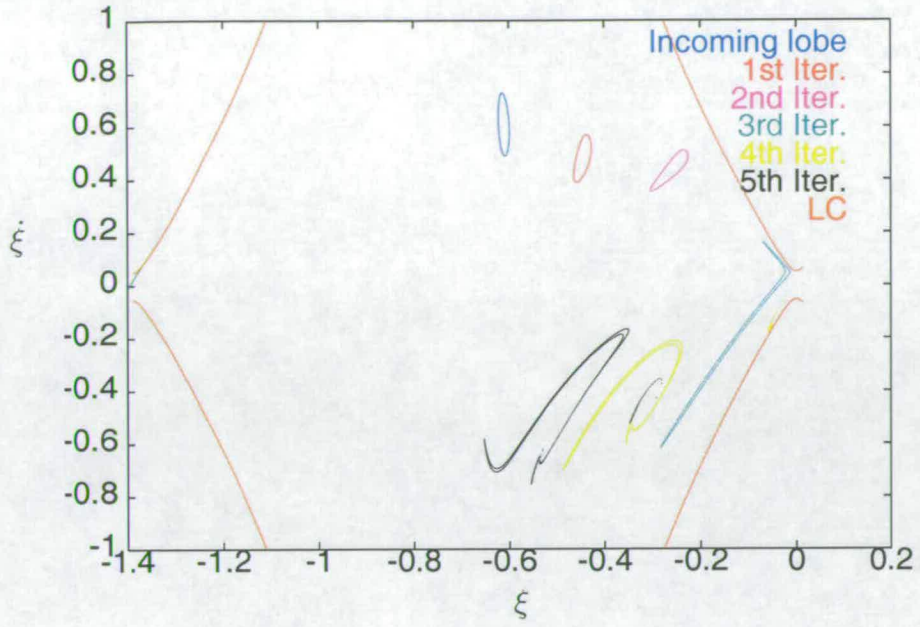

Figure 4.10: The (left) unstable manifold in $(\xi, \dot{\xi})$ space as it intersects the surface of section $\eta = 0, \dot{\eta} > 0$ (H=-2.1620). The line segment near the left fixed point is shown in green. "LC" refers to the limiting curves.

to curve, and end at an intersection with the lc at which point $\dot{\eta} = 0$. This is in keeping with the analytical approximation for the line segments which was obtained from eqns(??) and referred to earlier. The image of the line segments representing the unstable manifolds are the elongated closed curves, each of which is denoted 'Incoming lobe' - see figs(4.12) and (4.10). Subsequent intersections give further curves, which become increasingly stretched and convoluted. The series of closed curves in fig(4.10) represent the cross section of the tube.

Christou(1994) examined the surface of section at $H = H_{crit}$ and discovered the existence of a large zone of chaotic motion enclosing the curves in fig(4.11).

4.5 Comparison with Hénon's model

Many structures similar to those found in Hénon's model are present in Hill's problem. In order to consider the regions which are analogous to R_1 and R_2 of Chapter 3 we need to look closely at the stable and unstable manifolds

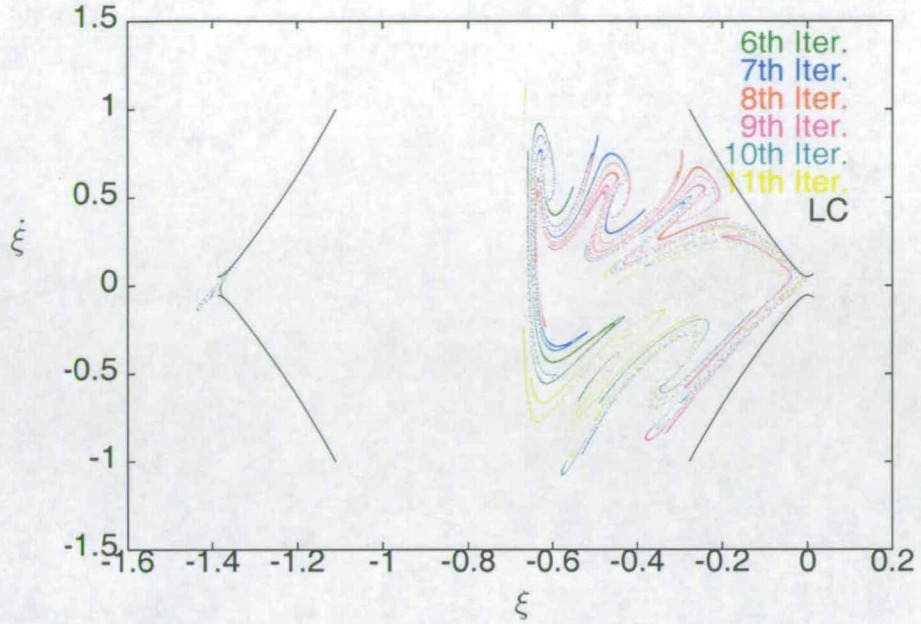

Figure 4.11: This shows further iterates of the manifold in fig(4.10).

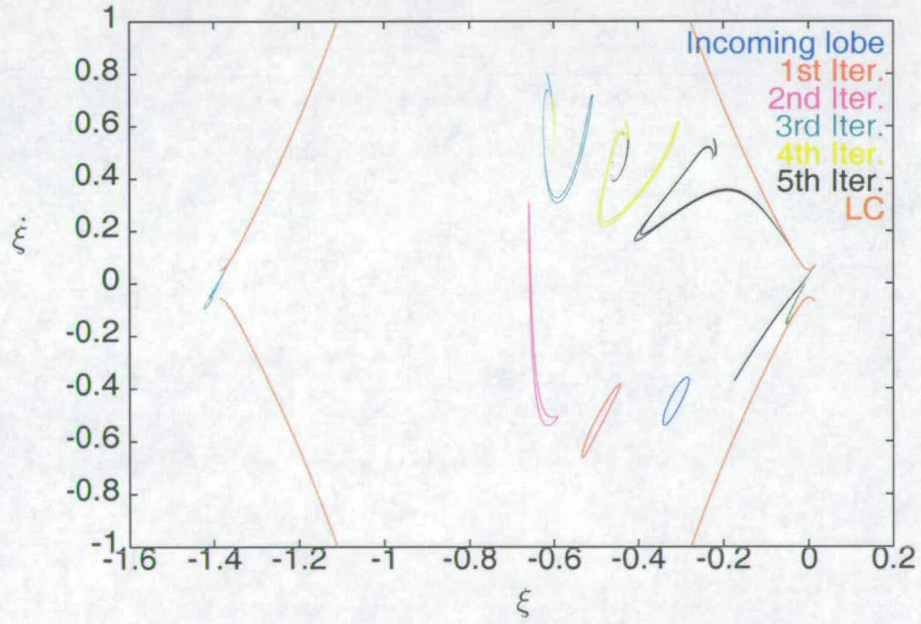

Figure 4.12: The (right) unstable manifold in $(\xi, \dot{\xi})$ space as it intersects the surface of section $\eta = 0, \dot{\eta} > 0$ (H=-2.1620). The line segment near the right fixed point is shown in green.

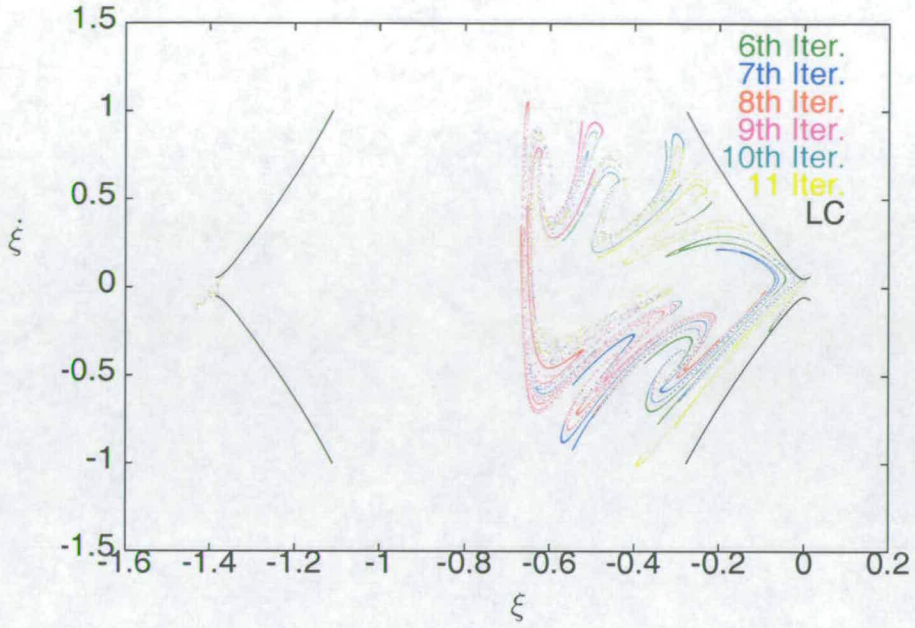

Figure 4.13: This shows further iterates of the manifold in fig(4.12).

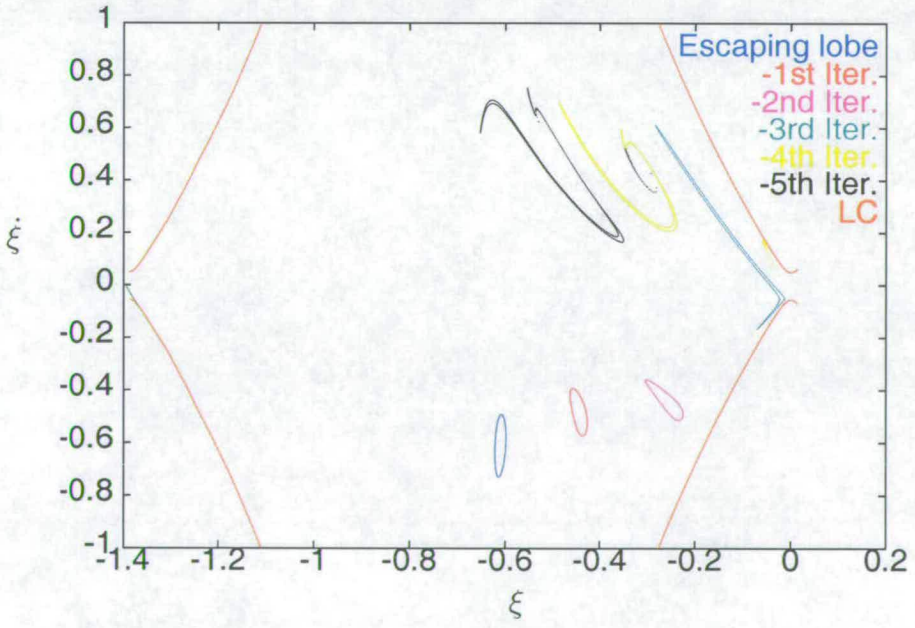

Figure 4.14: The (left) stable manifold.

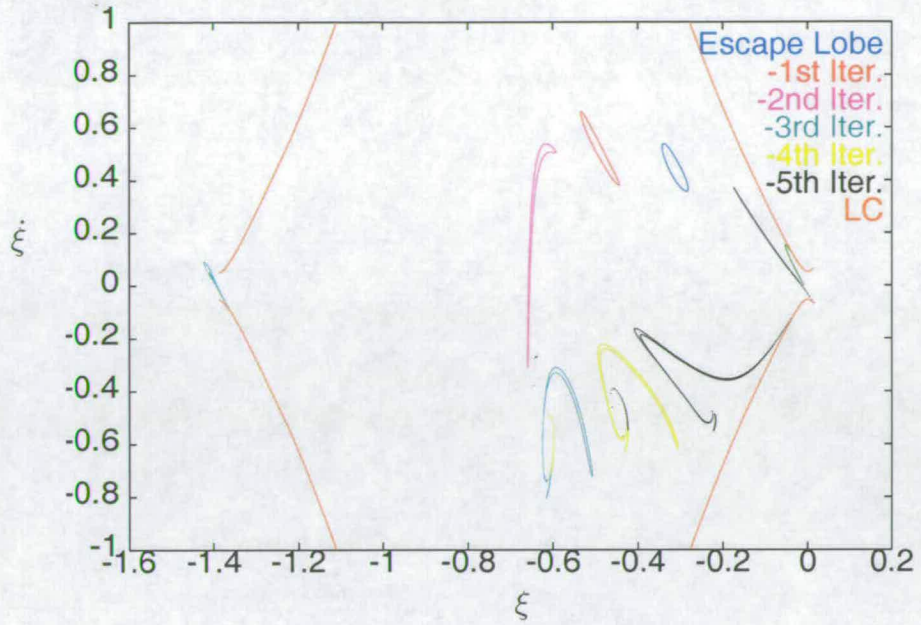

Figure 4.15: The (right) stable manifold.

in the vicinity of the fixed points. On the surface of section they appear as small continuous line segments (shown in green) in figs(4.10), (4.12), (4.14) and (4.15). The line segments are also shown schematically in fig(4.17); note that the inaccessible region is excluded from this description. We shall define the "interior" and "exterior" of the cluster by choosing these line segments as the boundary curve between the two regions. We now show that phase space which is about to enter the interior of the cluster lies just beyond the boundary curves. To see this, we could consider the preimage of points contained within the "Incoming lobe" of figs(4.10) and (4.12). The preimage is represented by the blue regions near the fixed points in fig(4.16). These regions are analogous to the lobes E_1 and E_1' of chapter three. Phase space which has just escaped from the cluster is represented by the red regions near the fixed points. The line segments shown (in bold) in fig(4.17) therefore form a convenient boundary curve between the interior and exterior of the cluster. The "Incoming" and "Escape" lobes of the previous section which are also shown in fig(4.16) may now be described according to the notation of chapter three. They are shown schematically in fig(4.17) when $H > H_{crit}$.

There are clear similarities between fig(4.17) and fig(3.19). In both cases

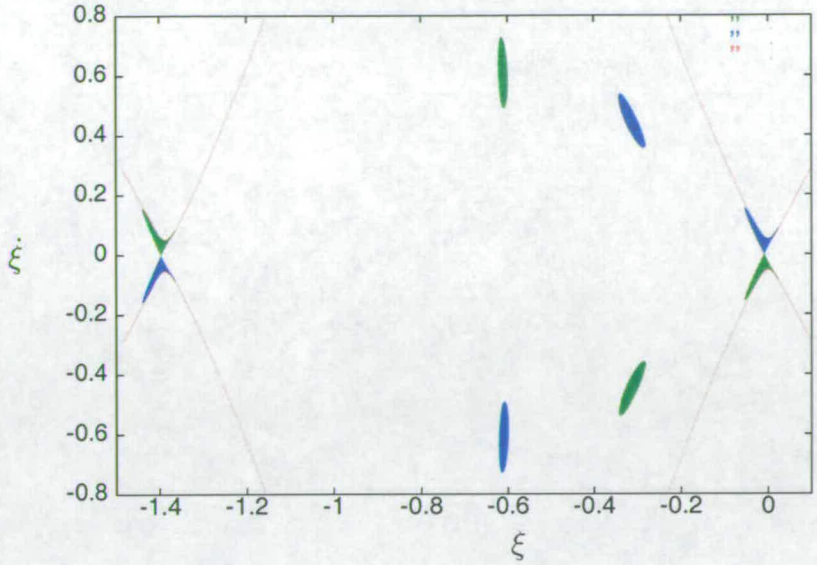

Figure 4.16: The blue and red regions near the fixed points lie outside the cluster just beyond the boundary curves (formed by the stable and unstable manifolds). The limiting curves are shown for $H = -2.1620$.

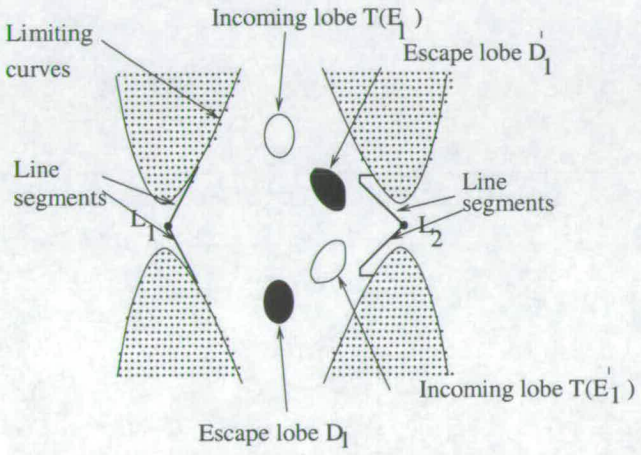

Figure 4.17: This shows (schematically) the incoming and escape lobes in Hill's Problem for some $H > H_{crit}$ using the notation of chapter three. D_1' and D_1 denote the right and left escape lobes respectively. Note that the preimage of (the boundary of) TE_1 on the surface $\eta = 0$ is the upper line segment at the Lagrangian point L_1; the preimage of (the boundary of) TE_1' is the lower boundary curve at L_2. The interior of the cluster consists of phase space lying between the Lagrangian points and bounded by the heavy line segments and the broken lines. The shaded region is inaccessible.

the area of phase space on the surface of section which enters the interior of the cluster (after one application of the Poincaré map) is equal to the combined area, $\mu(E_1 \cup E_1')$, of the incoming lobes. We should note that this area on the surface of section is not, in general, proportional to the volume of phase space. [2] The value of H in Hill's problem governs the area of the lobes (via its influence on A and the "diameter" of the "tubes") and plays the same role as ψ in Hénon's model.

Similarities can also be seen in observing the way the lobes undergo stretching. Fig(4.11) shows the incoming lobe from the left unstable manifold up to the 11th iteration. It is now very thin and elongated and no longer resembles the form it assumed on the first iteration. The lobes in Hénon's model also undergo stretching. Fig(4.11) is the analogue of fig(3.26).

In Hénon's model the incoming lobes are found to intersect the escape lobes after a certain number of iterations. Furthermore, the discontinuity at $X = 0$ causes the lobes to break up into disconnected sections. The transport of phase space in Hill's problem occurs in a roughly similar manner. Fig(4.18) shows portions of phase space, initially in the incoming lobes TE_1 and TE_1', after 2 and 5 applications of the Poincaré map - cf. fig(3.25). On the next iteration parts of these elements of phase space will escape. The areas of these portions (using the notation of Chapter 3) are $\mu(T^2TE_1' \cap D_1)$ and $\mu(T^5TE_1 \cap D_1)$. After intersecting the escape lobe the phase space which still remains in the interior of the cluster fragments into two disconnected sections. The 3rd iteration in fig(4.12) serves as a good example of a lobe in which this has happened. A similar situation arises at the right escape lobe -see fig(4.19). Phase space, initially in lobe TE_1', enters lobe D_1' on the 4th and 5th iterations. In addition, phase space, initially in lobe TE_1, enters lobe D_1' on the 2nd interation.

[2]The relationship between the full phase-space volume occupied by a group of orbits and the area in a surface of section filled by these orbits is discussed in Binney et al.(1985). One of the principal results they establish is that it is generally false to assume that the volume of phase space is proportional to the area on the surface of section. In this respect turnstile dynamics is less appropriate for the calculation of escape probabilities for a continuous dynamical system like Hill's problem than for a discrete system like Hénon's model.

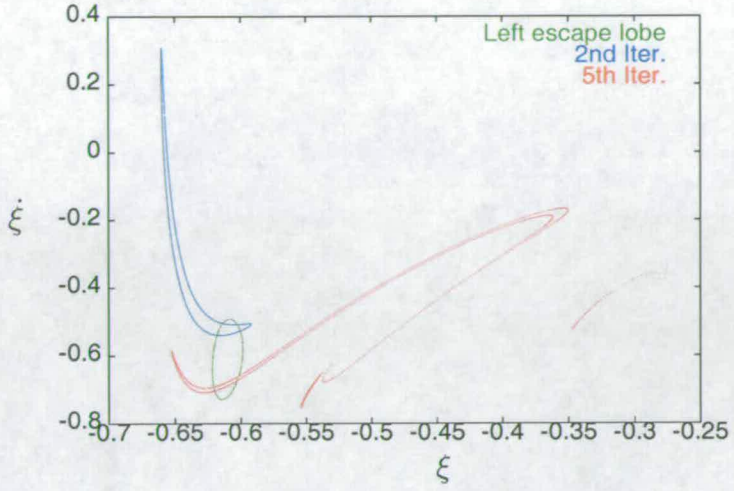

Figure 4.18: Portions of phase space belonging to the intersections $T^5(TE_1) \cap D_1$ (labelled "5th Iter.") and $T^2(TE_1') \cap D_1$ (labelled "2nd Iter.") will escape on the next iteration of the mapping - see figs(4.14), (4.12) and (4.10).

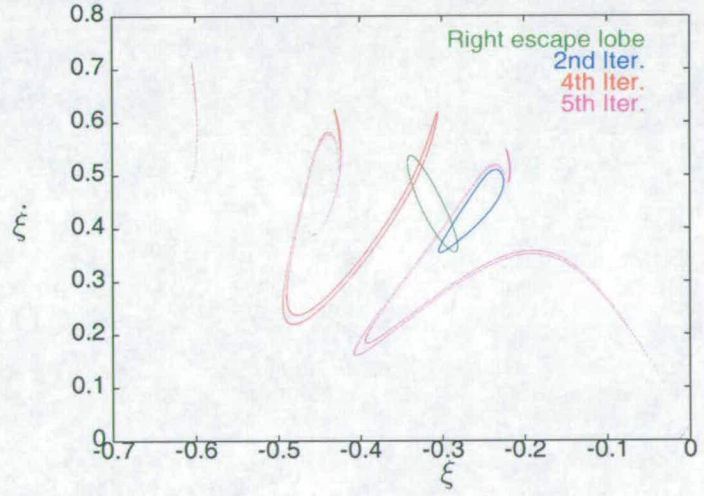

Figure 4.19: Portions of phase space belonging to the intersections $T^2(TE_1) \cap D_1'$ (labelled "2nd Iter."), $T^4(TE_1') \cap D_1'$ (labelled "4th Iter.") and $T^5(TE_1') \cap D_1'$ (labelled "5th Iter.") will escape from the cluster on the next iteration - see figs(4.15), (4.10) and (4.12).

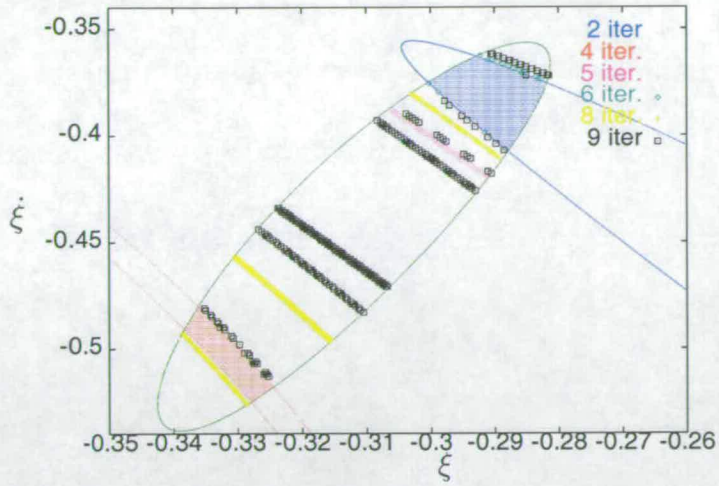

Figure 4.20: Lobe TE_1' showing portions of phase space which are labelled according to a colour scheme based on the escape time. The region "k iter." ($k = 2 \ldots 9$) enters either of the escape lobes in k iterations and escapes on the $k+1$th iteration.

Figs(4.20) and (4.21) show portions of the incoming lobe TE_1' which escape in a given number of iterations. For example, phase space which escapes in 3 iterations lies in the intersection $T^{-2}D_1 \cap TE_1'$ and is labelled "2 iter." - cf. fig(4.14). Figs(4.22) and (4.23) show the escape time (in the sense of number of iterations) for portions of phase space in lobe TE_1. Phase space which escapes in 3 iterations lies in the intersection $T^{-2}D_1' \cap TE_1$ and is labelled "2 iter." - see fig(4.15). Orbits which take longer to escape correspond to thinner strips of phase space. This is due to the stretching which occurs in lobes $T^{-n}D_1$ and $T^{-n}D_1'$ for large n.

4.5.1 The Escape Channels

As we have seen, phase space which is initially in the incoming lobes may escape from either lobe D_1 or D_1'. Fig(4.24) shows how this occurs. A region of chaos seems to exist (around the centre of the lobe) in which there is no clear boundary separating the right-escapers from the left-escapers. This is not unexpected, given the way the stable and unstable manifolds become tangled

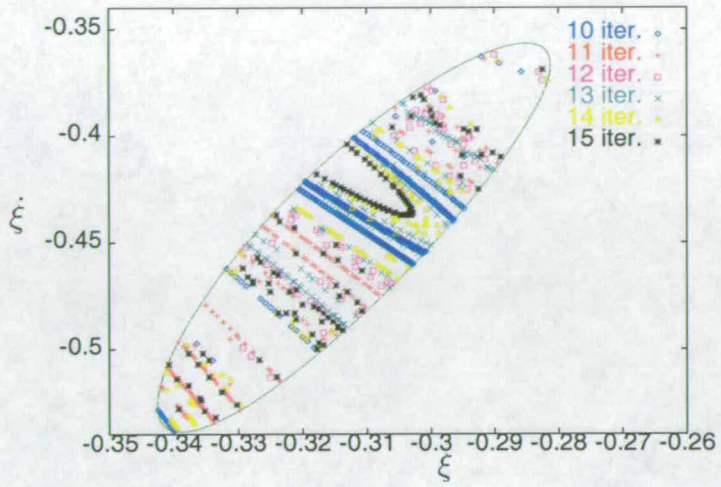

Figure 4.21: An extension of fig(4.20) ($k = 10 \ldots 15$).

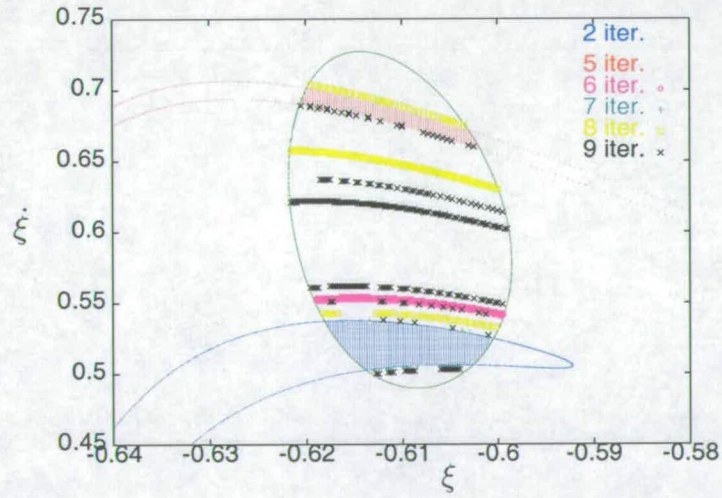

Figure 4.22: Lobe TE_1 showing portions of phase space which are labelled according to a colour scheme based on the escape time. The region "k iter." ($k = 2 \ldots 9$) enters either of the escape lobes in k iterations and escape on the $k + 1$th iteration.

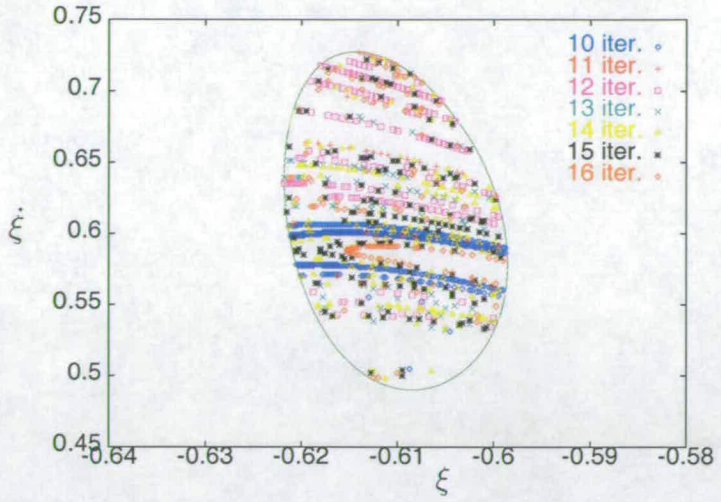

Figure 4.23: An extension of fig(4.22) ($k = 10 \ldots 16$).

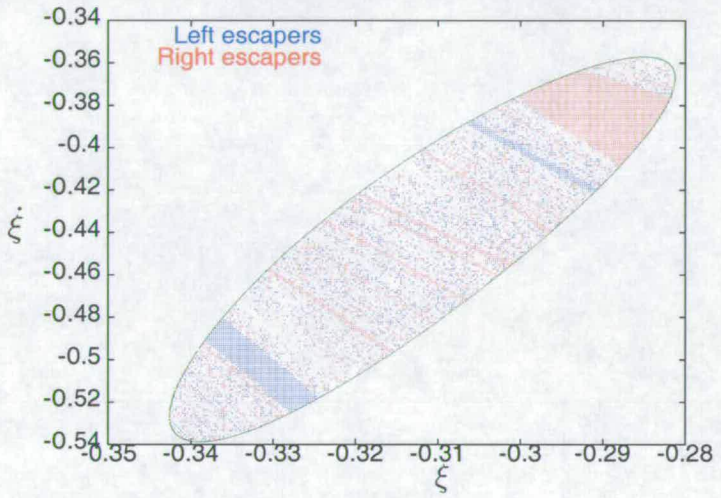

Figure 4.24: Lobe TE_1' showing the regions of phase space associated with right-escapers (red) (via lobe D_1) and left-escapers (blue) (via lobe D_1').

together.

4.5.2 The h-orbits

It will be recalled (Chapter 3) that the existence of right and left-escaping orbits had an important role to play in the structure of h-orbits in Hénon's model. Here we pursue the analogous orbits in Hill's problem.

Fractals may be generated from a set of orbits in Hill's problem in analogy to the h-orbits described in Chapter 3. In Hénon's model the particle was dropped with zero horizontal velocity onto the inclined surface from a fixed height (i.e.

with constant ψ) for various X_0 in the interval (-1,1) between the fixed points. In Hill's problem the family of h-orbits will be defined to be those with initial conditions

$$\xi_0 = C \quad \eta_0 = 0 \quad \dot{\xi}_0 = 0.$$

The Lagrangian points occur at $\xi = -2\xi_0$ and $\xi = 0$ (using displaced coordinates), and, due to symmetry, it is sufficient to select values of C from the subinterval $(-\xi_0, 0)$. (It will be seen that this interval demonstrates the salient features of the orbits.) The condition $\dot{\xi} = 0$ ensures that the orbits have "zero horizontal velocity". At a fixed value of H (analogous to the condition of constant ψ in Hénon's model), $\dot{\eta}_0$ is calculated from eqn(4.21).

Each time the orbit intersects the surface of section $\eta = 0, \dot{\eta} > 0$ the value of ξ is recorded. If $\xi = \xi_j$ on the jth intersection with the surface then the orbit may be represented symbolically by a sequence

$$\{d_j, \quad j = 1 \ldots \infty\}$$

where

$$d_j = \begin{cases} 1 & \text{if } \xi_j > -\frac{1}{3}^{1/3} \\ 0 & \text{if } \xi_j < -\frac{1}{3}^{1/3}. \end{cases}$$

If the orbit escapes through lobe D_1 on the kth iteration it will be assumed that

$$d_j = 1 \text{ for all } j \geq k.$$

(Note that an escaping orbit need not, however, intersect the surface of section more than once.) Similarly, if escape occurs through lobe D_1' on the kth iteration then

$$d_j = 0 \text{ for all } j \geq k.$$

As in Chapter 3 a real number $A \in (0, 1)$ can be calculated from the sequence $\{d_j\}$ as follows:

$$A = \sum_{j=1}^{\infty} 2^{-j} d_j.$$

Fig(4.25) exhibits the same fractal properties of self-similiarity which were present in fig(3.7). Notice, for example, that the curve between -0.3 and -0.2 appears to be a scaled version of the section between -0.2 and -0.05. Another

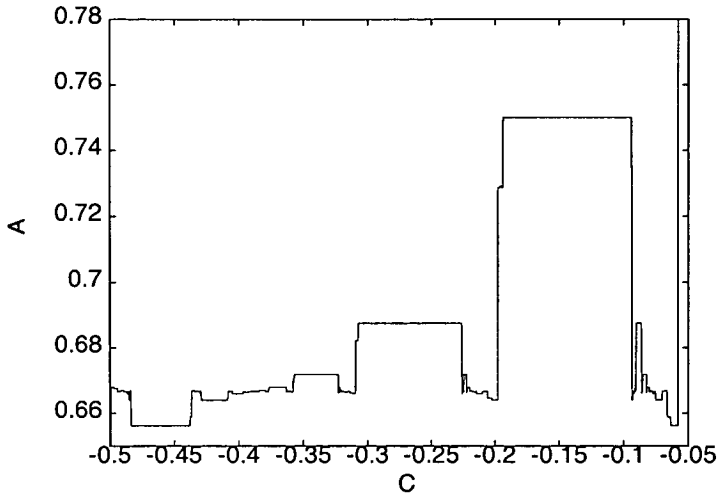

Figure 4.25: A against C in the case when $H = -2.12$.

common feature is the existence of horizontal bars whose length is a function of H. (It will be recalled that in Hénon's model the length of the bars was governed by the parameter ψ.) This gives further evidence that Hénon's model captures many of the features present in Hill's problem. [3]

4.6 The Escape Flux

4.6.1 Discrete Case

At each iteration the area of phase space (lying on the surface of section) which is detrained from the cluster is given by $\mu(D_1 \cup D_1')$. In what follows it will be convenient to introduce the notation D and TE to refer to the regions $D_1 \cup D_1'$ and $TE_1 \cup TE_1'$ respectively.

Suppose we consider phase space which is initially in lobe TE. After some time, on (say) the $(k-1)$th iteration of the mapping, a portion of this phase space may be found in lobe D. We define e_k to be that portion, i.e.

e_k = measure of phase space initially in lobe TE that escapes from the cluster on the kth iteration (cf. eqn. 3.91).

The following technique, which is based on eqn(3.98), describes how the escape

[3]With this in mind, fig(4.25) could be used to produce an escape distribution analogous to that for the case of h-orbits.

flux maybe computed.

Firstly, two grids (of the same mesh size) are placed over the incoming lobes TE_1 and TE_1'. The number of points contained in the lobes enables $\mu(TE)$ to be calculated approximately. The fraction of the total number of points which enter lobe D on the $(k-1)$th iteration is recorded. This is then used to give approximate values for e_k. Having calculated these quantities the following formula (cf. eqn. 3.98) is applied to compute the escape flux:

$$r_{1k} = \mu(TE) - \sum_{l=1}^{k} e_l. \tag{4.28}$$

Here, r_{1k} gives the area of phase space, initially in the interior of the cluster, which escapes on the kth iteration.

Taking $H = -2.1620$, two grids of mesh width (0.00025×0.001) were placed over the incoming lobes TE_1 and TE_1'. The lobes were found to accommodate 18433 and 16679 points respectively, giving a total of 35112. This meant that $\mu(TE) \simeq 0.00877$. The e_k were calculated using the technique described above. The escape flux is given in fig(4.26) which shows a plot of r_{1k} against k. The flux starts at a maximum but decreases due to the replacement of phase space, initially in the interior of the cluster, by phase space originating outside the cluster. It is expected that $r_{1k} \to 0$ as $k \to \infty$ and that the flux drops to zero more sharply when $H \gg H_{crit}$

4.6.2 Continuous Case

In the above calculation the escape flux was computed in a discrete fashion by applying the methods of Chapter 3. The time required for phase space, initially in the incoming lobes, to reach the escape lobes was measured crudely in terms of the number of iterations on the surface of section. We should note that this is of limited use since the actual time differs depending on which element of phase space is considered. Nevertheless, this approach, which was expressed in the language of Wiggins(1992), was useful in understanding the escape flux in the framework of turnstile dynamics. It also served to highlight similarities between Hénon's model and Hill's problem.

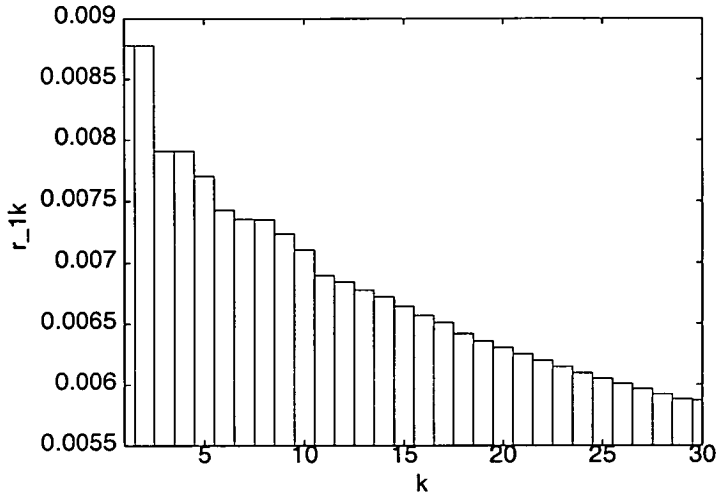

Figure 4.26: r_{1k} against k showing the flux of escaping phase when $H = -2.1620$.

In this section a *continuous* escape flux is computed by measuring the *instantaneous* rate at which phase space is detrained from the cluster. We consider elements of phase space entering the cluster near the Lagrangian points and lying on the surfaces of section $\xi = 0$ and $\xi = -2\xi_0$. When each element eventually escapes from the interior of the cluster it crosses either one of these surfaces in its outward passage. The escape flux is generated by measuring the time and the velocity component $\dot{\xi}$ at the instant at which this occurs. The precise details relating to this calculation are described as follows.

Points chosen subrandomly [4] are distributed uniformly in lobe TE_1 and then evolved backwards in time so that they lie on the surface $\xi = -2\xi_0$. These form region E_0 whose boundary may be approximated by an ellipse. The equation of this ellipse is given in sec(4.6.3). Suppose that the curves in $(\xi, \dot{\xi})$ and $(\eta, \dot{\eta})$ space which enclose lobe TE_1 and region E_0 are denoted by γ_1 and γ_2. In the vicinity of the fixed points, on a surface of section $\xi = -2\xi_0$, these curves are approximately elliptical The curves γ_1 and γ_2 encircle the same tube of phase trajectories. From a theorem on the integral invariant of Poincaré-Cartan (cf. Arnold 1978) we find that

$$\int_{\gamma_1} \dot{\xi} d\xi = \int_{\gamma_2} \dot{\eta} d\eta.$$

[4] see Numerical Recipes(1992)

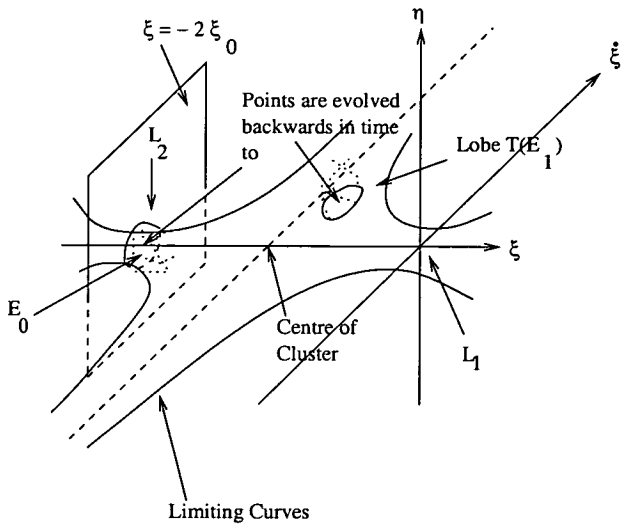

Figure 4.27: Points in lobe TE_1 are integrated backwards in time until they satisfy $\xi = -2\xi_0$.

This implies that the distribution of points in region E_0 (illustrated in fig(4.27)) is uniform since

$$\int_\gamma \dot{\xi} d\xi = \int_{\gamma'} \dot{\eta} d\eta$$

for *each* loop γ in $\xi = -2\xi_0$ and its image γ' in $\eta = 0$.

Similarly, region E_0' lies on the surface $\xi = 0$ and is the preimage of points in lobe E_1'. Figs(4.28) and (4.29) show regions E_0 and E_0' in $(\eta, \dot{\eta})$ space. Notice the existence of symmetry $(\eta \to -\eta, \quad \eta \to -\dot{\eta})$ which was not present in lobes TE_1 and TE_1'.

Fig(4.28) shows the projection onto the $(\eta, \dot{\eta})$ plane of a set of points $X = \{P_k, k = 1 \ldots 10000\}$, each member of which has position vector

$$\mathbf{p}_k = (\xi_k, \dot{\xi}_k, \eta_k, \dot{\eta}_k).$$

In this case $\xi_k = -2\xi_0$ for all k and the $\dot{\xi}_k$ component may be calculated from the Hamiltonian. Suppose the point P_k escapes at time $t = t_k^{esc}$ moving with a velocity component of $\dot{\xi}_k^{esc}$ across either the plane $\xi = -2\xi_0$ or $\xi = 0$. If each point represents an element of phase space of area δA then the escape flux, $r(t)$, (in analogy to eqn(4.28)) is given by

$$r(t) = r_0 - \sum_{\{k | t_k^{esc} < t\}} (\delta A) \dot{\xi}_k^{esc} \tag{4.29}$$

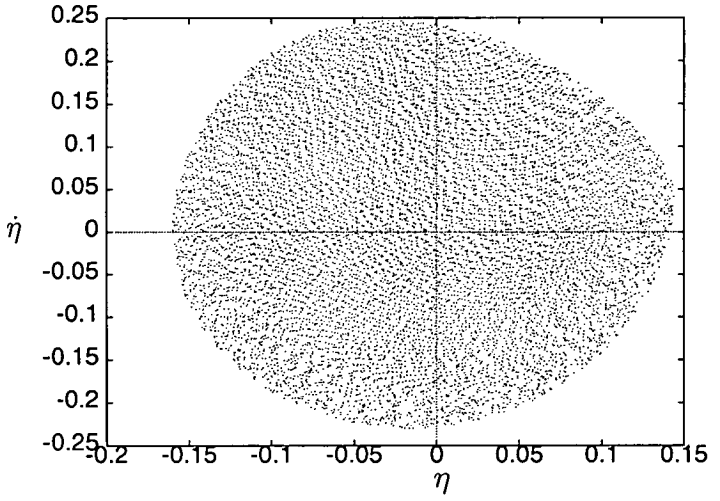

Figure 4.28: Region E_0 in $(\eta, \dot{\eta})$ space ($H = -2.1263$).

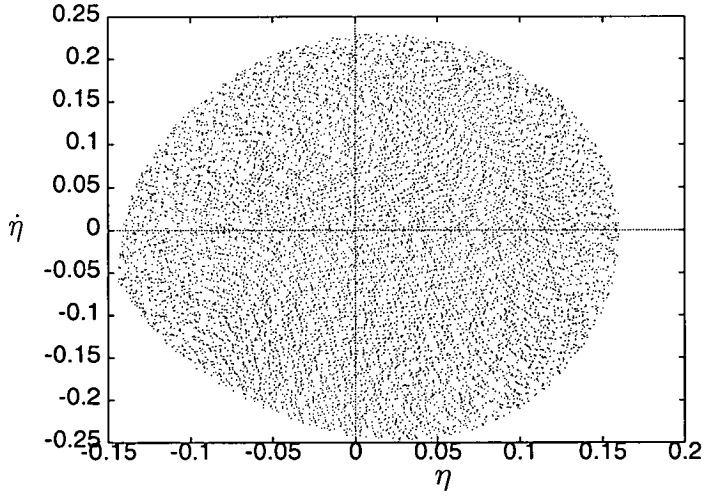

Figure 4.29: Region E_0' in $(\eta, \dot{\eta})$ space ($H = -2.1263$).

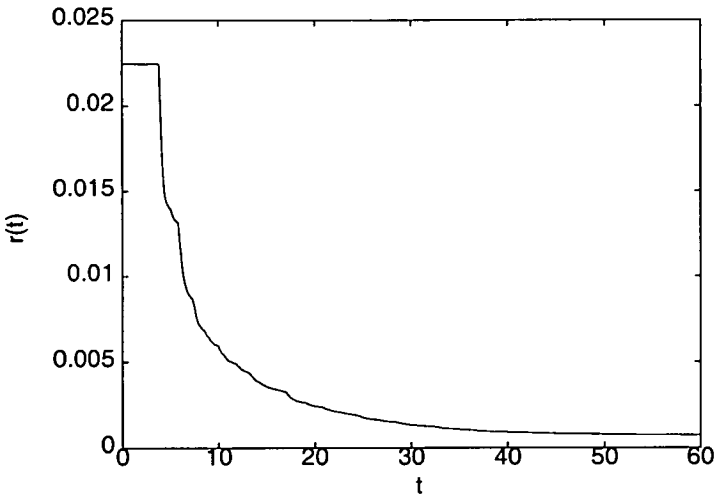

Figure 4.30: $r(t)$ against t showing the escape flux. In this case $H = -2.1263$, $\mu(E_0) = 0.1119$ (determined numerically using a Monte Carlo technique), $\delta A = 0.1119/10000$ (since the points are distributed uniformly) and $r_0 = 0.02246$.

where r_0 is the total initial flux given by

$$r_0 = \sum_{all\ k} (\delta A)\dot{\xi}_k.$$

Fig(4.30) shows $r(t)$ against t for phase space originating in region E_0. An identical graph is obtained for phase space in region E_0'. This is due to the symmetry which is present in fig(4.28) and fig(4.29). Note that in sec(4.6.1) this symmetry was not present in lobes TE_1 and TE_1'.

4.6.3 Analytical determination of $\mu(E_0)$.

In the above calculation $\mu(E_0)$ was determined numerically using a Monte Carlo approach. This was done by placing a rectangle filled with points (chosen subrandomly) over the vicinity of the lobe TE_1. The fraction of the total number of points lying inside the lobe multiplied by the area of the rectangle gives an estimation of $\mu(E_0)$. The analytical theory (valid near the fixed points) can be used to estimate the area. The projection of the unstable manifold (obtained from eqn(4.19)) on the surface $\xi = -2\xi_0$ gives a good approximation[5].

[5]In reality both the stable and unstable manifolds require to be considered in order to ensure that the condition $\dot{\xi} > 0$ is satisfied. Although more complicated to describe, this would explain the existence of the cusp near the point (0.14,0.03) in fig(4.28).

Consider the unstable manifold of the Liapounov orbit in eqn(4.19) at the right fixed point. Replacing $\xi - \xi_0$ by ξ and setting $c_2 = t = 0$ a solution is sought which satisfies $\xi = 0$. Region E_0 is then described parametrically in the variables A and α by the following equations :

$$\begin{aligned} \eta &= -b_1 A\cos(\alpha) + Ab_2\sin(\alpha) \\ \dot{\eta} &= -b_1 k_1 A\cos(\alpha) - Ak_2 b_2\cos(\alpha). \end{aligned} \tag{4.30}$$

We assume that A can vary between 0 and A_0 where A_0 is an upper bound determined from the value of the Hamiltonian in eqn(4.23). The area enclosed in the region is given by

$$\begin{aligned} \mu(E_0) &= \int_0^{2\pi}\int_0^{A_0} \frac{\partial(\eta,\dot{\eta})}{\partial(A,\alpha)} dAd\alpha \\ &= \pi A_0^2(b_1 b_2 k_1 + k_2 b_2^2) \\ &= \frac{2\pi(b_1 b_2 k_1 + k_2 b_2^2)(H - H_{crit})}{k_2^2 b_2^2 - 9} \\ &= \frac{2\pi(H - H_{crit})}{k_2} \\ &= 3.033019232(H - H_{crit}) \end{aligned} \tag{4.31}$$

When $H = -2.1263$ we find that $\mu(E_0) = 0.1124$ which should be compared with the Monte Carlo estimate of 0.1119. We could also have used eqn(4.31) to obtain an estimate of the value of $\mu(TE_1)$ in sec(4.6.1). In that case, $H = -2.1620$ and eqn(4.31) gives 0.004246. This should be compared with the Monte-Carlo estimate of (18433/35112)*0.00877=0.004604.

4.7 Escape in the 3-Dim Hill Problem

In the 3-dimensional Hill problem motion is permitted in the direction of the axis which lies perpendicular to the plane defined by the motion of the cluster around the galaxy. Certain modifications require to be made to the earlier theory. In particular, a 3-dimensional orthogonal system of rotating coordinates, (X_r, Y_r, Z_r), centred on the galaxy is introduced. The star's position (in this more general system) is given by (cf. sec 4.2)

$$X_i = R + \xi, \quad Y_i = \eta, \quad Z_i = \zeta$$

and the Lagrangian is

$$\mathcal{L} = \frac{1}{2}(\dot{X}_i^2 + Y_i^2 + Z_i^2) - V_g - V_c$$

where

$$V_g = -\frac{GM_g}{\sqrt{X_r^2 + Y_r^2 + Z_r^2}}.$$

Following a similar approach to that described earlier V_g may be expanded around the point $X_i = R, Y_i = 0, Z_i = 0$ to yield the approximation :

$$V_g \approx \omega^2 R\xi - \omega^2\xi^2 + \frac{1}{2}\omega^2(\eta^2 + \zeta^2).$$

¿From eqn(4.6) it is clear that the expressions for p_1 and p_2 remain unaltered. If ζ is temporarily replaced by q_3 then the conjugate variable p_3 is given by

$$p_3 = \frac{\partial \mathcal{L}}{\partial \dot{q}_3} = \dot{q}_3.$$

In the 3-dimensional problem we may take

$$\mathcal{H} = \frac{1}{2}(p_1 + \omega q_2)^2 + \frac{1}{2}(p_2 - \omega(q_1 + R))^2 - \frac{3}{2}\omega^2 q_1^2 + V_c + \frac{1}{2}(p_3^2 + \omega^2 q_3^2).$$

This expression yields eqns(4.10) as before. In addition the following equation is obtained for q_3 :

$$\ddot{q}_3 + \omega^2 q_3 = -\frac{GM_c q_3}{r^3}.$$

Rescaling distance and time gives

$$\begin{aligned}
\ddot{\xi} - 2\dot{\eta} - 3\xi &= -\frac{\xi}{r^3} \\
\ddot{\eta} + 2\dot{\xi} &= -\frac{\eta}{r^3} \\
\ddot{\zeta} + \zeta &= -\frac{\zeta}{r^3}.
\end{aligned} \tag{4.32}$$

These equations are the 3-dimensional form of Hill's equations. The value of the Hamiltonian, which is conserved, may also be written as

$$\mathcal{H} = \frac{1}{2}(\dot{\xi}^2 + \dot{\eta}^2 + \dot{\zeta}^2) + \frac{1}{2}(\zeta^2 - 3\xi^2) - \frac{1}{r}. \tag{4.33}$$

The latter equation in (4.32) may be linearised around the right fixed point to give

$$\ddot{\zeta} + 4\zeta = 0.$$

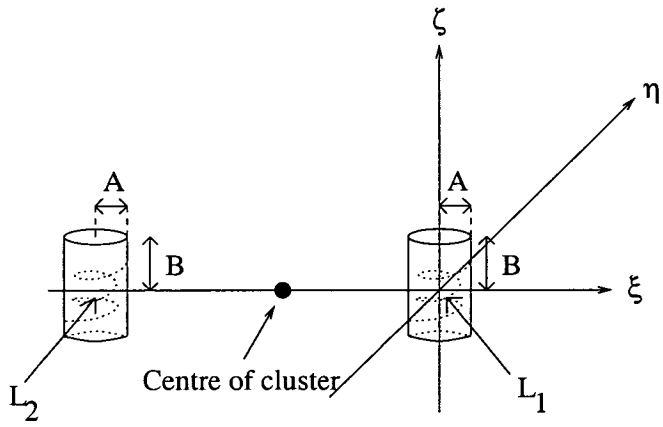

Figure 4.31: The quasi-periodic orbit in the 3-dimensional problem lies inside one member of a family of cylinder-like surfaces generated for various A, B satisfying eqn(4.34). The origin is taken at the Lagrangian point L_1.

The solution to this equation, which should be taken together with eqn(4.19), is

$$\begin{aligned} \zeta &= B\sin(2t+\beta) \\ \dot{\zeta} &= 2B\cos(2t+\beta). \end{aligned}$$

This gives an orbit which is quasi-periodic if we take $c_1 = c_2 = 0$. An expression analogous to eqn(4.22) may be found in the 3-dimensional problem by expanding $H - H_{crit}$ about the fixed point and then substituting the expression for the quasi-periodic orbit. The expansion gives

$$H - H_{crit} = \frac{1}{2}(\dot{\xi}^2 + \dot{\eta}^2 + \dot{\zeta}^2) - \frac{9}{2}(\xi - \xi_0)^2 + \frac{3}{2}(\eta^2 + \zeta^2) + \frac{\zeta^2}{2}$$

and after carrying out the substitution (and setting $t = \frac{\alpha+2\pi}{k_2}$) it is found that

$$2(H - H_{crit}) \approx A^2 k_2^2 b_2^2 - 9A^2 + 4B^2 \tag{4.34}$$

in place of eqn(4.23). In this approximation no assumptions are made concerning the value of β. Fig(4.31) shows the general arrangement.

The escape flux is computed by applying the same technique which was described in section (4.6.2). The main difference is that in the 3-dimensional problem the lobes are of a higher dimension than their corresponding counterparts in the coplanar setting. The details are described as follows.

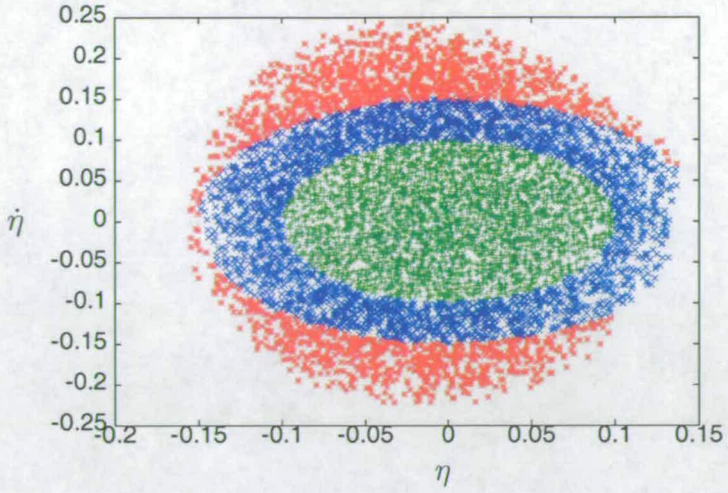

Figure 4.32: Points in $\mathcal{X}$ lying on the surface of section $\xi = -2\xi_0$ projected in $(\eta, \dot{\eta})$ space ($H = -2.1263$).

In the 3-dimensional problem the analogue of lobe TE_1 on the surface of section $\eta = 0$ is a 4-dimensional volume in $(\xi, \dot{\xi}, \zeta, \dot{\zeta})$ space. This volume is filled with points, chosen subrandomly, which are then evolved backwards in time until they lie on the surface of section $\xi = -2\xi_0$. Suppose that the set of points on the surface $\xi = -2\xi_0$ is denoted by $\mathcal{X} = \{\mathcal{P}_i, \quad i = 1 \ldots 10073\}$. (Note the change in notation from the previous section, i.e. $\mathcal{P}, \mathcal{X}$ and not P, X.) Each point has a position vector

$$\mathbf{p}_i = (\xi_i, \dot{\xi}_i, \eta_i, \dot{\eta}_i, \zeta_i, \dot{\zeta}_i)$$

where $\xi = -2\xi_0$ and $\dot{\xi}_i$ is calculated from the Hamiltonian in eqn(4.33). The volume of the region these points occupy may be denoted by $\mu(\mathcal{E}_0)$. Figs(4.32) and (4.33) show the projection of these points in $(\eta, \dot{\eta})$ and $(\zeta, \dot{\zeta})$ space.

As described in fig(4.31) the quasi-periodic orbit lies inside a cylinder-like volume. This volume is one member of a family of similar structures generated for various A, B satisfying eqn(4.34). When A is at a maximum B is at minimum and vice versa (since the total coefficient of A^2 in eqn(4.34) is positive). This observation is in keeping with the colour scheme in figs(4.32) and (4.33). For example, points near the origin in $(\eta, \dot{\eta})$ space (shown in green) correspond to points existing up to large distances from the origin in $(\zeta, \dot{\zeta})$ space.

The points are evolved forward in time until they escape crossing either the

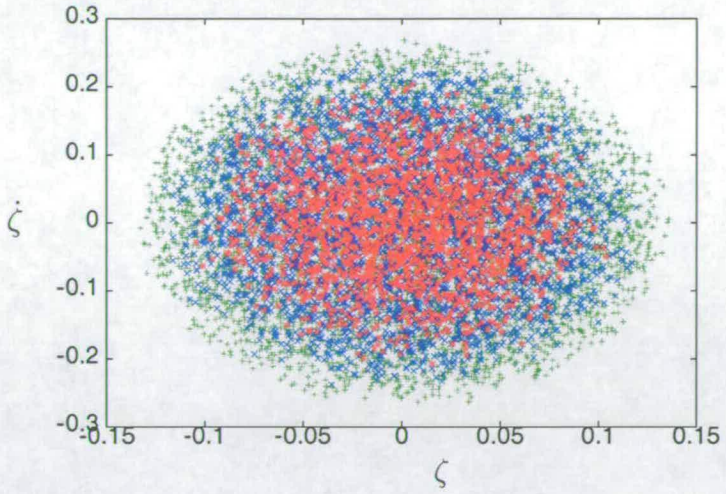

Figure 4.33: Points in $\mathcal{X}$ lying on the surface of section $\xi = -2\xi_0$ projected in $(\zeta, \dot{\zeta})$ space ($H = -2.1263$).

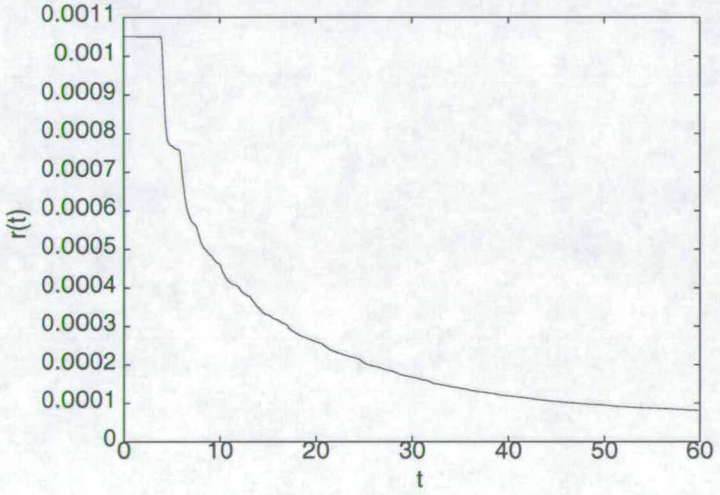

Figure 4.34: $r(t)$ against t showing the escape flux in the 3-dimensional problem. In this case $H = -2.1263$, $\mu(\mathcal{E}_0) = 0.00653$ (determined numerically using a Monte Carlo technique), $\delta A = \mu(E_0)/10073 = 6.48 \times 10^{-7}$ and $r_0 = 0.001050$.

plane $\xi = 0$ or $\xi = -2\xi_0$ on their outward passage. The flux of escapers is computed in the same way as described in the previous subsection by applying an equation analogous to eqn(4.29). The results are shown in fig(4.34). Fig(4.34) is the analogue of fig(4.30). Note that the total initial flux, r_0, in the 3-dimensional problem is small in comparison to the value of r_0 in the coplanar setting.

4.7.1 Analytical determination of $\mu(\mathcal{E}_0)$.

In the 3-dimensional problem region E_0 is parametrised by 4 variables A, α, B, β. We shall use an analogous technique to that which is described in subsec(4.6.3), the only difference being that we now have to consider motion in the ζ direction. This means integrating over a 4-dimensional volume. As before, the value of the Hamiltonian imposes an upper bound on A which we shall call A_0. The equations which describe the region on the surface $\xi = 0$ are given by

$$\begin{aligned} \eta &= -b_1 A\cos(\alpha) + Ab_2\sin(\alpha) \\ \dot{\eta} &= -b_1 k_1 A\cos(\alpha) - Ak_2 b_2\cos(\alpha) \\ \zeta &= B\sin\beta \\ \dot{\zeta} &= 2B\cos\beta \end{aligned} \tag{4.35}$$

Taking the function $f(A)$ to be, from eqn(4.34),

$$f(A) = \frac{1}{2}\sqrt{2(H - H_{crit}) - (k_2^2 b_2^2 - 9)A^2}$$

the volume, $\mu(\mathcal{E}_0)$, is given by

$$\begin{aligned} \mu(\mathcal{E}_0) &= \int_{A=0}^{A_0}\int_{B=0}^{f(A)}\int_{\beta=0}^{2\pi}\int_{\alpha=0}^{2\pi}\frac{\partial(\eta,\dot{\eta},\zeta,\dot{\zeta})}{\partial(A,\alpha,B,\beta)}d\alpha d\beta dB dA \\ &= \int_{A=0}^{A_0}\int_{B=0}^{f(A)}\int_{\beta=0}^{2\pi}\int_{\alpha=0}^{2\pi} 2BA(b_1 b_2 k_1 + k_2 b_2^2)\ d\alpha d\beta dB dA \\ &= 4\pi^2\int_{A=0}^{A_0}\int_{B=0}^{f(A)} 2BA(b_1 b_2 k_1 + k_2 b_2^2)dB dA \\ &= \frac{\pi^2(b_1 b_2 k_1 + k_2 b_2^2)(H - H_{crit})^2}{k_2^2 b_2^2 - 9} \\ &= \frac{\pi^2(H - H_{crit})^2}{k_2} \\ &= 4.764255615(H - H_{crit})^2. \end{aligned}$$

When $H = -2.1263$ this gives $\mu(\mathcal{E}_0) = 0.006548$ which should be compared with the Monte Carlo estimate of 0.00653.

4.8 The Elliptic Hill Problem

In the Elliptic Hill Problem it is assumed that the cluster moves round the centre of the galaxy in an elliptical orbit as illustrated in fig(4.35). The coplanar

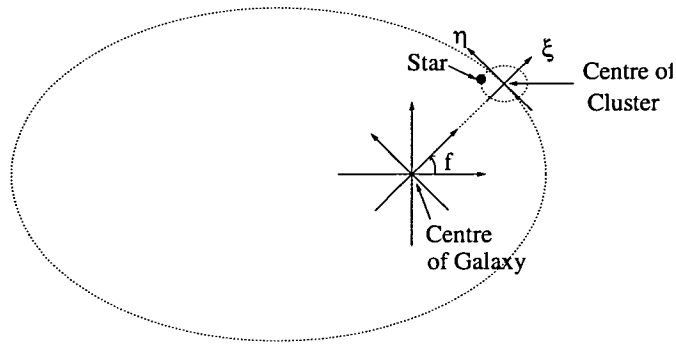

Figure 4.35: The elliptical motion of the cluster around the centre of the galaxy.

problem will be dealt with here.

A nonuniformly rotating and pulsating [6] coordinate system, (ξ, η), centred on the cluster is introduced, so that the "transformed distance $\sqrt{\xi^2 + \eta^2}$" between the cluster and galaxy remains constant. A suitable rescaling is performed so that the equations are expressed in Hill's coordinates. The Elliptic Hill Equations may be derived from Szebehely(1967) by considering the case of the Elliptic Restricted Problem in which $\mu \rightarrow 0$ (cf. sec. 1.2).

Unlike the circular case, in which the cluster rotates with constant angular velocity ω, the Hamiltonian is now time dependent and is given by

$$H = \frac{1}{2}\{(p_1 + q_2)^2 + (p_2 - q_1)^2\} - \frac{1}{1 + e\cos f}(\frac{3}{2}q_1^2 + \frac{1}{r}) \qquad (4.36)$$

where $q_1 = \xi, q_2 = \eta, p_1 = p_\xi, p_2 = p_\eta$ and $r = \sqrt{\xi^2 + \eta^2}$; f is the true anomaly of the cluster with respect to the galaxy (i.e. the polar angle of the radius vector to the cluster centre) and is used as the independent variable; e is the eccentricity of the orbit. The generalised momenta are given by

$$\begin{aligned} p_1 &= \dot{\xi} - \eta \\ p_2 &= \dot{\eta} + \xi. \end{aligned}$$

where a dot denotes differentiation with respect to f.

Now we seek an expression analogous to the Jacobi Integral (cf. eqn. 4.21).

[6] This means that the physical coordinates are scaled by the distance between the cluster and the galaxy, which is variable.

If h is the value of H then (from Hamilton's equations)

$$\dot{h} = \frac{\partial H}{\partial f} = \frac{-e \sin f}{(1 + e \cos f)^2} \{ \frac{3}{2} \xi^2 + \frac{1}{r} \}.$$

This implies that

$$h = h_0 - e \int \frac{\Omega \sin f \ df}{(1 + e \cos f)^2}.$$

where

$$\Omega = \frac{3}{2} \xi^2 + \frac{1}{r}$$

and h_0 is determined from the the initial conditions (assuming $f = 0$ initially) by

$$h_0 = \frac{1}{2}(\dot{\xi}_0^2 + \dot{\eta}_0^2) - \frac{1}{1+e}(\frac{3}{2}\xi_0^2 + \frac{1}{r_0}).$$

The fact that h now varies increases the complexity of the problem since many familiar structures such as the limiting curves are no longer present.

The Elliptic Hill Equations which result from eqn(4.36) are given by

$$\begin{aligned} \ddot{\xi} - 2\dot{\eta} &= \frac{1}{1 + e \cos f}(3\xi - \frac{\xi}{r^3}) \\ \ddot{\eta} + 2\dot{\xi} &= \frac{1}{1 + e \cos f}(\frac{-\eta}{r^3}). \end{aligned} \tag{4.37}$$

4.8.1 The Quasi-Periodic Orbits

Quasi-periodic (qp) orbits will be used later in this chapter to form an approximate boundary curve in the stability analysis of h-orbits. Approximate analytic expressions are derived here which show the main features of the orbits.

When e is small an approximate solution may be found to the Elliptic Hill Equations in the neighbourhood of the Lagrangian point $(\xi_0, 0)$. For small eccentricities, the linearised form of eqns(4.37) is

$$\begin{aligned} \ddot{\xi} - 2\dot{\eta} &= 9(\xi - \xi_0)(1 - e \cos f) \\ \ddot{\eta} + 2\dot{\xi} &= -3\eta(1 - e \cos f) \end{aligned} \tag{4.38}$$

where, it will be recalled,

$$\dot{} \equiv \frac{d}{df}.$$

We now seek a solution for ξ and η in terms of a power series in e. It is assumed that

$$\xi = \xi^{(0)} + e\xi^{(1)} + e^2\xi^{(2)} \ldots$$
$$\eta = \eta^{(0)} + e\eta^{(1)} + e^2\eta^{(2)} \ldots . \tag{4.39}$$

By substituting these expansions for ξ and η into eqn(4.38) and comparing coefficients of powers in e we obtain

$$\begin{aligned}
\ddot{\xi}^{(0)} - 2\dot{\eta}^{(0)} &= 9(\xi^{(0)} - \xi_0) \\
\ddot{\eta}^{(0)} + 2\dot{\xi}^{(0)} &= -3\eta^{(0)} \\
\ddot{\xi}^{(1)} - 2\dot{\eta}^{(1)} &= 9\xi^{(1)} - 9(\xi^{(0)} - \xi_0)\cos f \\
\ddot{\eta}^{(1)} + 2\dot{\xi}^{(1)} &= -3\eta^{(1)} + 3\eta^{(0)}\cos f.
\end{aligned} \tag{4.40}$$

The periodic solutions for $\xi^{(0)}$ and $\eta^{(0)}$ are, from eqn(4.19),

$$\begin{aligned}
\xi^{(0)} &= \xi_0 + A\cos(k_2 f - \alpha) \\
\eta^{(0)} &= -Ab_2 \sin(k_2 f - \alpha).
\end{aligned} \tag{4.41}$$

The third and fourth equations may then be solved for $\xi^{(1)}$ and $\eta^{(1)}$. The final solution for the qp orbit is given by

$$\begin{aligned}
\xi &= \xi_0 + A\cos(k_2 f - \alpha) + e\{C_1 A\cos((k_2+1)f - \alpha) \\
&\quad + C_2 A\cos((k_2 - 1)f - \alpha)\} \\
\dot{\xi} &= -k_2 A\sin(k_2 f - \alpha) + e\{-AC_1(k_2+1)\sin((k_2+1)f - \alpha) \\
&\quad - AC_2(k_2 - 1)\sin((k_2 - 1)f - \alpha)\} \\
\eta &= -Ab_2\sin(k_2 f - \alpha) + e\{C_3 A\sin((k_2+1)f - \alpha) + \\
&\quad C_4 A\sin((k_2 - 1)f - \alpha)\} \\
\dot{\eta} &= -Ab_2 k_2\cos(k_2 f - \alpha) + e\{C_3 A(k_2+1)\cos((k_2+1)f - \alpha) + \\
&\quad C_4 A(k_2 - 1)\cos((k_2 - 1)f - \alpha)\}
\end{aligned} \tag{4.42}$$

where the constants are given by

$$C_1 = \frac{3}{2}\Big\{\frac{-28\sqrt{7} + 59 - 31k_2 + 14\sqrt{7}k_2}{k_2(-3 + 12\sqrt{7} + 4k_2 + 8\sqrt{7}k_2)(k_2+1)}\Big\} = -0.007483122$$

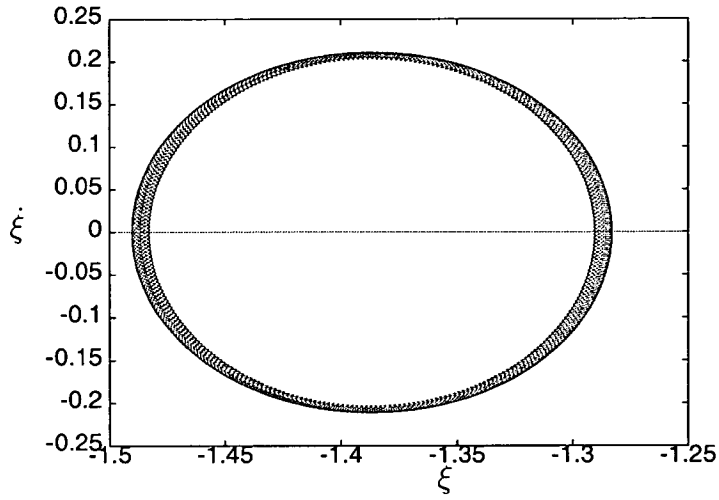

Figure 4.36: The qp orbit in $(\xi, \dot{\xi})$ space ($e = 0.05$, $A = 0.1$, $\alpha = 0$).

$$C_2 = \frac{3}{2}\Big\{\frac{22\sqrt{7}k_2 + 14\sqrt{7} - 125k_2 - 160}{k_2(-9 - 2\sqrt{7} + 2k_2)(-12\sqrt{7} + 3 + 4k_2 + 8\sqrt{7}k_2)}\Big\} = 0.7973457746$$

$$C_3 = \frac{3}{2}\Big\{\frac{5\sqrt{7} + 56 + 2k_2(1 + \sqrt{7})}{(4 + 8\sqrt{7})k_2^2 + (12\sqrt{7} - 3)k_2}\Big\} = 0.7549742433$$

$$C_4 = \frac{3}{2}\Big\{\frac{-5\sqrt{7} - 56 + 2k_2 + 2\sqrt{7}k_2}{k_2(-12\sqrt{7} + 3 + 4k_2 + 8\sqrt{7}k_2)}\Big\} = -1.675874763.$$

Figs(4.36) and (4.37) show the quasi-periodic orbit (obtained from eqns(4.42)) at the Lagrangian point L_1 in $(\xi, \dot{\xi})$ space and $(\eta, \dot{\eta})$ space respectively. The orbit lies on a torus and a family of tori is obtained by varying the constant A. (In the circular case a relationship was found to exist between A and the quantity $H - H_{crit}$. In the elliptic problem, however, there is no analogue to this since the Hamiltonian is time dependent.) An important observation which will be required later is that if $\alpha = 0$ each member of this family is essentially an h-orbit (although this is not true in general). The h-orbits are characterised by the fact that $\dot{\xi}(0) = 0$ and $\eta(0) = 0$, and so their initial conditions may be represented in the two dimensional phase space $(\xi, \dot{\eta})$.

4.8.2 Regularisation

The Elliptic Hill Equations contain a singularity when $r = 0$. It was found that this singularity led to numerical errors when integrating orbits passing close to the centre of the cluster. (The same singularity exists in the circular case but

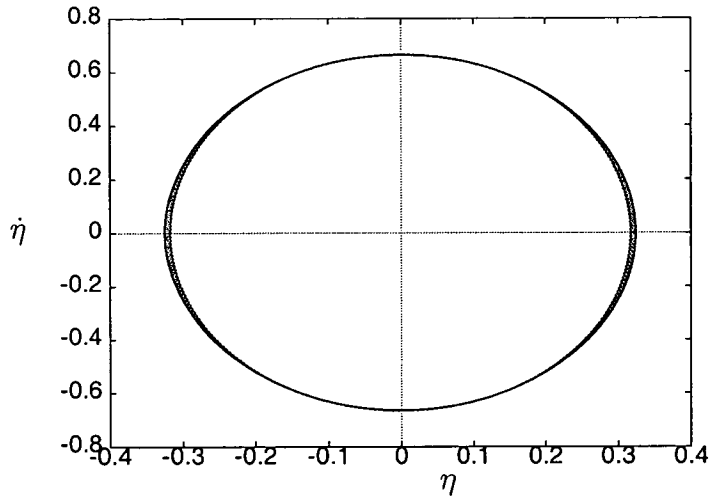

Figure 4.37: The qp orbit in $(\eta, \dot{\eta})$ space ($e = 0.05$, $A = 0.1$, $\alpha = 0$).

the results in secs(4.4) to (4.6) were obtained from the unregularised equations. This was permissible since the orbits did not pass close enough to the centre of the cluster for this to be a problem.) To obtain accurate results it was therefore necessary to implement a regularised form of eqns(4.37). The regularisation process removes the singularities and is helpful for numerical studies.

The regularised equations may be derived by applying a canonical transformation to the Hamiltonian in eqn(4.36). The variables ξ, η, p_ξ, p_η and the Hamiltonian H are transformed to u, v, p_u, p_v and $\tilde{H}$ by the generating function

$$S = -p_\xi(u^2 - v^2) - p_\eta(2uv)$$

(cf. Szebehely 1967). This implies that the transformation is

$$\xi = -\frac{\partial S}{\partial p_\xi} = u^2 - v^2; \quad \eta = -\frac{\partial S}{\partial p_\eta} = 2uv$$

$$p_u = -\frac{\partial S}{\partial u} = 2up_\xi + 2vp_\eta; \quad p_v = -\frac{\partial S}{\partial v} = -2vp_\xi + 2up_\eta.$$

The new variables u, v are functions of f. Note also that the transformed Hamiltonian

$$\tilde{H} = H + \frac{\partial S}{\partial f}$$

and so $\tilde{H} = H$. This Hamiltonian is now written in the *extended* phase space (cf. Szebehely 1967) as

$$\Gamma = \tilde{H} - h = \frac{1}{4(u^2 + v^2)}\{\frac{1}{2}(p_u^2 + p_v^2) - 2(u^2 + v^2)(-vp_u + up_v)$$

$$-\frac{6(u^2-v^2)^2(u^2+v^2)}{1+e\cos f}-\frac{4}{1+e\cos f}+2(u^2+v^2)^3\}-h.$$

We now introduce a time transformation to remove the singularity associated with the term

$$\frac{1}{u^2+v^2}$$

in Γ. Sundman's selection is

$$dt=g(u,v)d\tau$$

where τ is the new time and $g(u,v)=u^2+v^2$. If we denote the transformed Hamiltonian by Γ^* then

$$\Gamma^*=g(\tilde{H}-h)=\frac{1}{2}(p_u^2+p_v^2)-2(u^2+v^2)(-vp_u+up_v)-\frac{6(u^2-v^2)^2(u^2+v^2)}{1+e\cos f}$$
$$-\frac{4}{1+e\cos f}+2(u^2+v^2)^3-4h(u^2+v^2).$$

Hamilton's equations yield

$$u'=\frac{\partial\Gamma^*}{\partial p_u}=p_u+2v(u^2+v^2);\quad v'=\frac{\partial\Gamma^*}{\partial p_v}=p_v-2u(u^2+v^2);$$
$$p_u'=-\frac{\partial\Gamma^*}{\partial u}=4u(-vp_u+up_v)+2p_v(u^2+v^2)$$
$$+\frac{24u(u^2-v^2)(u^2+v^2)+12u(u^2-v^2)^2}{1+e\cos f}-12u(u^2+v^2)^2+8hu;$$
$$p_v'=-\frac{\partial\Gamma^*}{\partial v}=4v(-vp_u+up_v)-2p_u(u^2+v^2)-$$
$$\frac{24v(u^2-v^2)(u^2+v^2)-12v(u^2-v^2)^2}{1+e\cos f}-12v(u^2+v^2)^2+8hv,$$

where $'$ denotes differentiation with respect to τ.

The regularised equations are therefore given by

$$u''-8(u^2+v^2)v'=\frac{12u(u^2-v^2)(3u^2+v^2)}{1+e\cos f}+8uh_0-8ue\int\frac{\Omega\sin f\ df}{(1+e\cos f)^2},$$
$$v''+8(u^2+v^2)u'-\frac{12v(u^2-v^2)(3v^2+u^2)}{1+e\cos f}+8vh_0-8ve\int\frac{\Omega\sin f\ df}{(1+e\cos f)^2}.$$

In order to integrate these equations numerically we transform the system to a set of first order equations which are then solved using the subroutine D02BHF from the NAG library. The integral is handled by introducing a new variable, w (say) where

$$w=\int\frac{\Omega\sin f\,df}{(1+e\cos f)^2}.$$

4.8.3 Escape Analysis of h-orbits.

The escape of h-orbits in the Elliptic Hill Problem is explored in this section by placing a grid of points over the $(\xi_0, \dot{\eta}_0)$ plane of initial conditions. As in sec(4.8.1) we shall assume that $\dot{\xi}_0(0) = \eta_0(0) = 0$. Escape will be said to have occurred when the particle remains beyond either one of the two Lagrangian points for two consecutive passages of the cluster through pericentre. Furthermore we will insist that the particle lies further away on the second passage than on the first. In mathematical terms this may be expressed as follows. If r_k denotes the star's distance from the centre of the cluster at $f_k = f_0 + 2k\pi, \quad f_0 = 0, \quad k = 0, 1, 2 \ldots$ then escape occurs in k revolutions of the cluster about the galaxy if

$$r_{k+1} > r_k > (\frac{1}{3})^{\frac{1}{3}}.$$

The stable and unstable regions are determined by computing the escape time for each grid point. A very similar technique has been used by Benest (1998) in an investigation of planetary orbits in the Elliptic Restricted Problem. Loosely speaking, regions of stability (instability) are associated with orbits having long (short) escape times. The regularised equations are used throughout this study so that those trajectories which pass close to the centre of the cluster may be integrated accurately.

Figs(4.38), (4.39) and (4.40) show the regions of stability/instability for $e = 0$, $e = 0.25$, $e = 0.5$ respectively. The region shown in yellow leads to stable orbits. Orbital stability was investigated for the region $\xi_0 < 0$ since this region represents the interior of the cluster. (These use a shifted coordinate ξ such that the Lagrangian point lies at $\xi = 0$.) Notice that the retrograde orbits ($\xi > -\xi_0$, $\dot{\eta} < 0$) are, in general, more stable than the prograde orbits (cf. Ross et al. 1997). The main conclusion which may be drawn from these results is that increasing the eccentricity causes the stable region to contract slightly. In addition to this, the border separating the stable and unstable regions becomes much less distinct.

The lower boundary curve in fig(4.38) represents a family of retrograde periodic orbits. These are shown in figs(4.41) (4.42) and (4.43). It is useful to

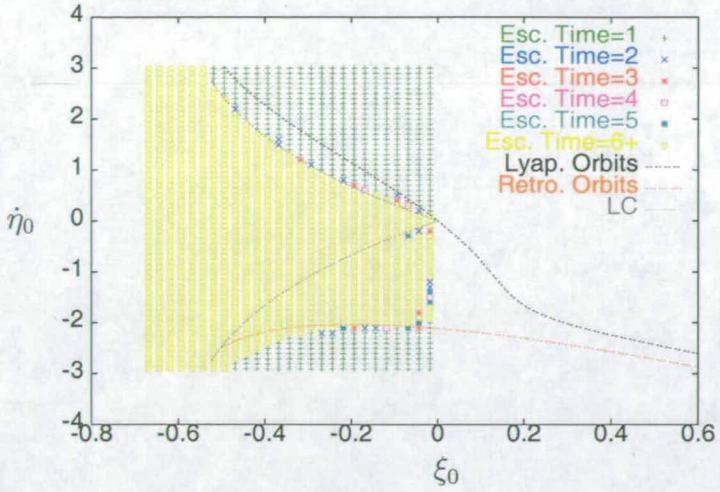

Figure 4.38: Regions of stability/instability in the plane $(\xi_0, \dot{\eta}_0)$, $e = 0$.

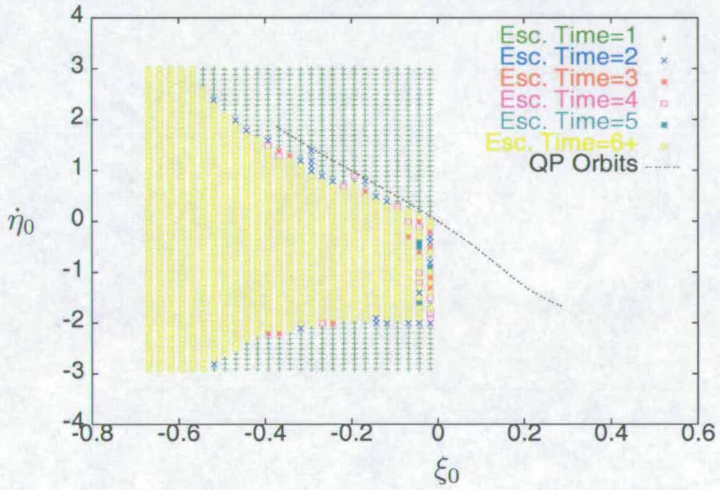

Figure 4.39: Regions of stability/instability in the plane $(\xi_0, \dot{\eta}_0)$, $e = 0.25$.

mention some earlier work on these orbits. Hénon(1970), for example, considered one particular member of this family and showed that, surrounding the orbit, was a family of *quasi-periodic* orbits. Other studies include the work of Ross et al.(1997) who use the retrograde periodic orbits to show that stars may lie at large distances from a globular cluster without escaping.

We see in fig(4.38) that the retrograde periodic orbits are useful for (approximately) demarcating the boundary between regions of stability and instability, at least in the circular problem.

An attempt was also made to calculate a boundary curve from the retrograde periodic orbits in the case $e \neq 0$. There is a complication, however, which is that

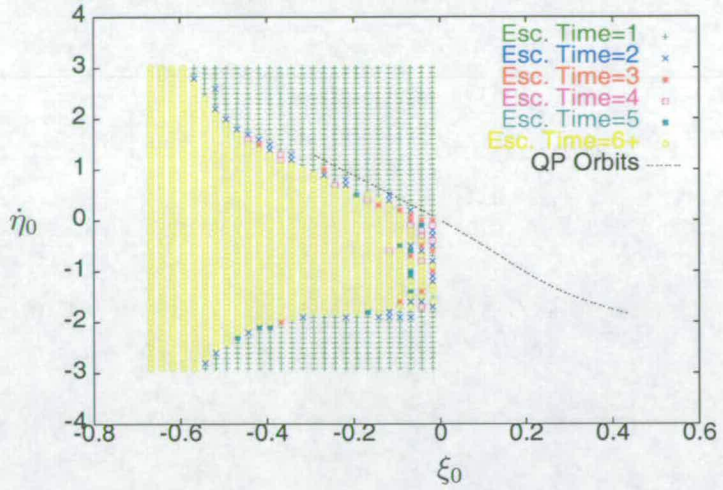

Figure 4.40: Regions of stability/instability in the plane $(\xi_0, \dot{\eta}_0)$, $e = 0.5$.

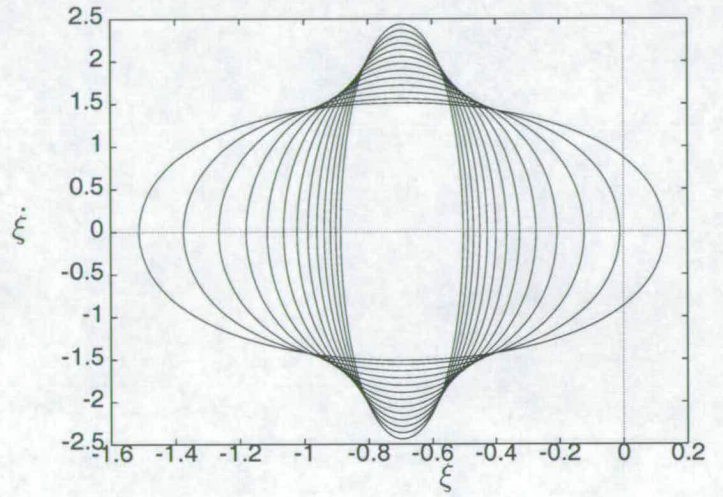

Figure 4.41: The retrograde periodic orbits in $(\xi, \dot{\xi})$ space $(e = 0)$.

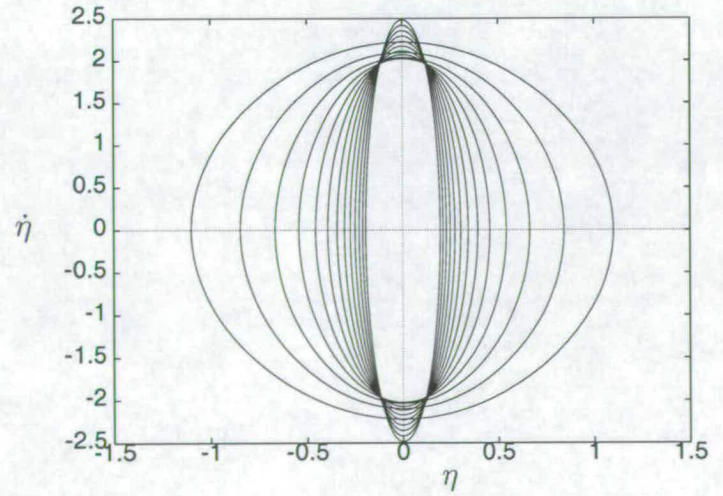

Figure 4.42: The retrograde periodic orbits in $(\eta, \dot{\eta})$ space $(e = 0)$.

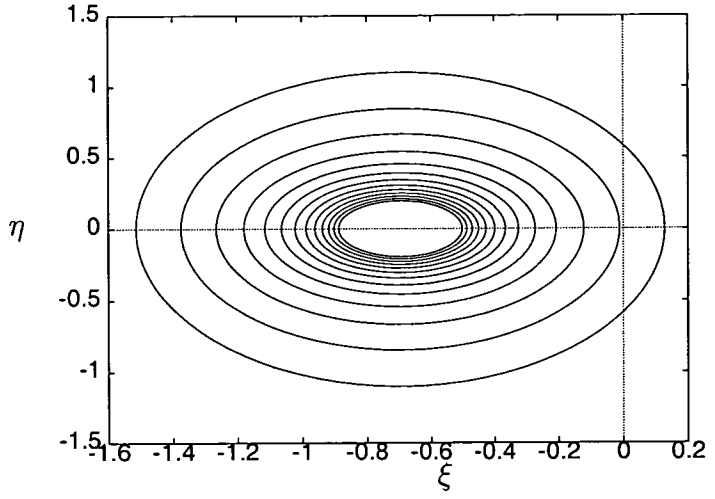

Figure 4.43: The retrograde periodic orbits in (ξ, η) space $(e = 0)$.

continuity of behaviour with respect to the eccentricity can only be expected to occur when the period of the star's orbit in the circular problem $(e = 0)$ is an integer multiple of 2π (Ichtiaroglou 1980, 1981). A smooth transition can only be found, therefore, at discrete points along the boundary curve in fig(4.38). For this reason, successive attempts at mapping the border of the stable region in the case $e \neq 0$ proved to be unfruitful.

4.8.4 Escape at high eccentricities

When the cluster moves in a highly eccentric orbit around the centre of the galaxy, the star, for the most part, describes nearly 2-body Keplerian motion about the centre of the cluster as the perturbation from the galaxy is so weak. The star's motion undergoes dramatic change, however, when the cluster moves through pericentre, when it is closest to the centre of the galaxy. The force due to the galaxy increases sharply for a short period of time and causes the star to experience a sudden change in momentum. This behaviour may be modelled approximately by supposing that the star is subjected to an impulsive force or "kick" [7]. The effect of this "kick" is to send the star into a new Keplerian orbit. It will remain in this orbit until the next passage through pericentre. After a certain number of "kicks" the star may receive enough energy to escape. (We

[7] A clear treatment of impulsive forces is contained in Synge and Griffith(1959).

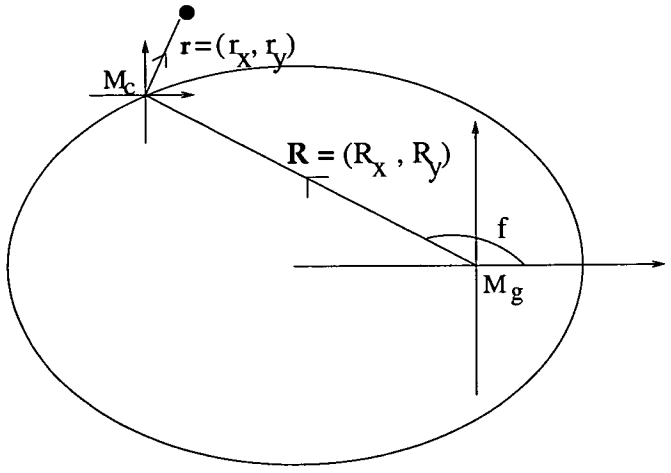

Figure 4.44: The rotating frame of reference.

shall deal with the coplanar problem in which the plane of motion of the star coincides with that of the cluster around the galaxy.)

We shall describe the motion of the star in an accelerating frame of reference as shown in fig(4.44). The impulsive force is obtained by expanding the disturbing function in terms of Legendre polynomials (cf. eqn 2.4 or Szebehely 1967) and is given by $\nabla\mathcal{R}$ where

$$\mathcal{R} \approx \frac{GM_g}{R^3}(\frac{1}{2}r^2 - \frac{3}{2}(\hat{\mathbf{R}}.\mathbf{r})^2).$$

$\mathbf{R} = (R_x, R_y)$ and $\mathbf{r} = (r_x, r_y)$ are the position vectors of the cluster and the star - see fig(4.44). This implies that

$$\nabla\mathcal{R} = n^2(\frac{a}{R})^3(3(\mathbf{r}.\hat{\mathbf{R}})\hat{\mathbf{R}} - \mathbf{r})$$

where we have used the approximate relation $n^2a^3 = GM_g$ (cf. eqn 2.10). Here n is the mean motion of the cluster around the centre of the galaxy and a is the semi-major axis of the elliptical orbit.

The differential equation governing the motion of the star contains the additional term, $\nabla\mathcal{R}$, and is therefore given by

$$\ddot{\mathbf{r}} = -\frac{GM_c}{r^3}\mathbf{r} + \nabla\mathcal{R}. \tag{4.43}$$

Distance and time may be rescaled as follows

$$\mathbf{r} = \left(\frac{GM_c}{n^2}\right)^{\frac{1}{3}}\bar{\mathbf{r}}, \quad \bar{t} = nt$$

to give (dropping the bars)

$$\ddot{\mathbf{r}} = -\frac{\mathbf{r}}{r^3} + \frac{a^3(3(\mathbf{r}.\hat{\mathbf{R}})\hat{\mathbf{R}} - \mathbf{r})}{R^3}.$$

As already stated we model the solution by treating the perturbation as an impulsive force. This causes the star's momentum to change discontinuously by an amount $\Delta\dot{\mathbf{r}}$ where

$$\Delta\dot{\mathbf{r}} = \int \frac{a^3(3(\mathbf{r}.\hat{\mathbf{R}})\hat{\mathbf{R}} - \mathbf{r})}{R^3}\ dt \tag{4.44}$$

$$= 3\Big(\int_{-\pi}^{\pi} \frac{r_x(\cos E - e)^2\ dE}{(1 - e\cos E)^4}, \int_{-\pi}^{\pi} \frac{r_y(1-e^2)\sin^2 E\ dE}{(1 - e\cos E)^4} \Big)$$

$$- \Big(\int_{-\pi}^{\pi} \frac{r_x\ dE}{(1 - e\cos E)^2}, \int_{-\pi}^{\pi} \frac{r_y\ dE}{(1 - e\cos E)^2} \Big)$$

where we have written $\mathbf{r} = (r_x, r_y)$ and have used the facts that

$$\hat{\mathbf{R}} = (\hat{R}_x, \hat{R}_y) = \Big(\frac{\cos E - e}{1 - e\cos E}, \frac{\sin E\sqrt{1-e^2}}{1 - e\cos E}\Big);$$

$$R = a(1 - e\cos E); \quad dt = (1 - e\cos E)dE$$

(cf. Murray and Dermott 2000). The integrals are, however, more easily evaluated in terms of the variable f. We use the following expressions for dt and R:

$$dt = \frac{R^2 df}{a^2\sqrt{1-e^2}} \quad \text{and} \quad R = \frac{a(1-e^2)}{1 + e\cos f}$$

Eqn(4.44) can then be written as

$$\Delta\dot{\mathbf{r}} = \Big(\int \frac{r_x a^3\cos^2 f\ dt}{R^3}, \int \frac{r_y a^3 \sin^2 f\ dt}{R^3} \Big)$$

$$= \Big(\int_{-\pi}^{\pi} \frac{r_x a\cos^2 f\ df}{R\sqrt{1-e^2}}, \int_{\pi}^{\pi} \frac{r_y a\sin^2 f\ df}{R\sqrt{1-e^2}} \Big)$$

$$= \frac{\pi}{(1-e^2)^{\frac{3}{2}}}(r_x, r_y)$$

since r_x and r_y are treated as constants. This implies that

$$\Delta\dot{\mathbf{r}} = 14.54441044(r_x, r_y) \text{ when } e = 0.8 \tag{4.45}$$

$$\Delta\dot{\mathbf{r}} = 37.93319916(r_x, r_y) \text{ when } e = 0.9 \tag{4.46}$$

The change in momentum, $|\Delta\dot{\mathbf{r}}|$, is greatest(least) when the star is at apocentre(pericentre) in its orbit about the cluster.

We now consider a 1-parameter family of initial conditions which, in the absence of perturbations, gives rise to circular Keplerian orbits at various energies. This family is parametrised by γ and is given by:

$$\left\{\xi_0 = \gamma; \quad \dot{\xi}_0 = 0; \quad \eta_0 = 0; \quad \dot{\eta}_0 = \frac{1}{\sqrt{\gamma}}\right\}.$$

The Keplerian orbit is numerically integrated until $f = 2n\pi, \quad n = 1, 2, \ldots$. Each time $f \equiv 0 mod 2\pi$ the star is subjected to an impulsive force. The integer n measures the number of revolutions of the cluster about the galaxy. If the star's position and velocity at the instant the "kick" occurs are $\mathbf{r}_{old}$ and $\dot{\mathbf{r}}_{old}$ (respectively) then the new position and velocity are given by

$$\mathbf{r}_{new} = \mathbf{r}_{old} \qquad \dot{\mathbf{r}}_{new} = \frac{\pi \mathbf{r}_{old}}{(1-e^2)^{\frac{3}{2}}} + \dot{\mathbf{r}}_{old}.$$

The star therefore assumes a different Keplerian orbit each time the cluster passes through pericentre. Eventually the star's energy may change sign (i.e. from negative to positive) implying that it is no longer bound to the cluster. The escape time is measured in terms of the number of kicks, n, which occurred prior to the change in sign of the energy. The typical situation is illustrated in fig(4.45).

It would be of interest to know how the escape time depends on the initial energy. Stars orbiting in close proximity to the centre of the cluster (with large negative energy) are least affected by the impulsive force and therefore have long escape times. If $Esc(\gamma)$ is the number of revolutions of the cluster about the centre of the galaxy before escape occurs and γ is the radius of the (initially circular) orbit then $Esc(\gamma) \to \infty$ as $\gamma \to 0$. A critical energy exists above which the star will escape immediately. Figs(4.46) and (4.47) show the escape time, $Esc(\gamma)$, against $\frac{1}{\gamma}$ when $e = 0.8$ and $e = 0.9$ respectively. Increasing the eccentricity causes the stars to escape more quickly.

In reality stars do not escape exactly in the way described above. Though the star may experience a sharp change in momentum when the cluster is at pericentre its momentum still changes continuously with respect to time and not discontinuously (which is an assumption made in the above model).

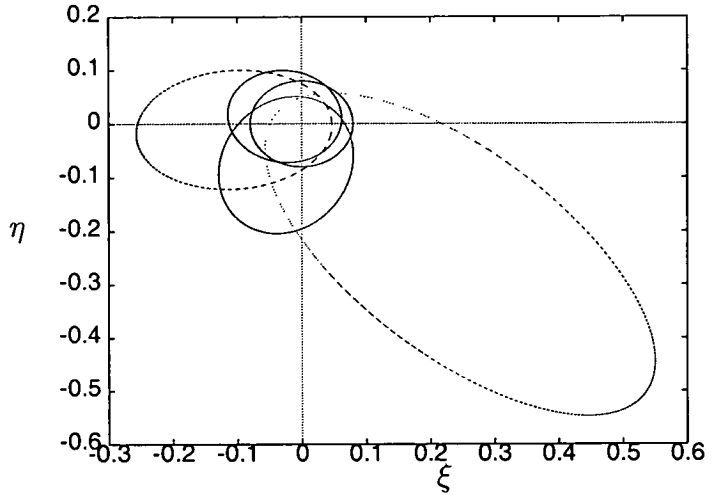

Figure 4.45: This shows a star with initial conditions ($\xi_0 = 0.08, \dot{\xi}_0 = 0, \eta_0 = 0, \dot{\eta}_0 = \sqrt{1/0.08}$) which is subjected to 4 kicks (taking $e = 0.8$). On the 5th kick its energy becomes positive causing it to escape. (The resulting escape trajectory is not shown.)

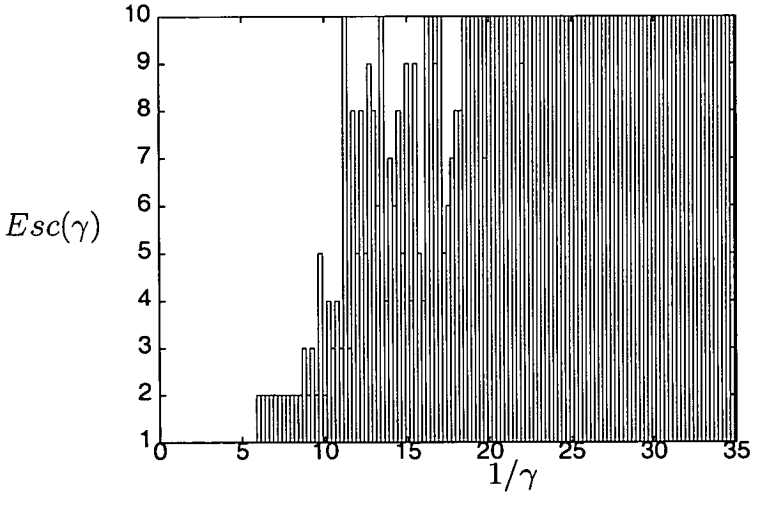

Figure 4.46: The escape time, $Esc(\gamma)$, against the energy, $\frac{1}{\gamma}$ when $e = 0.8$.

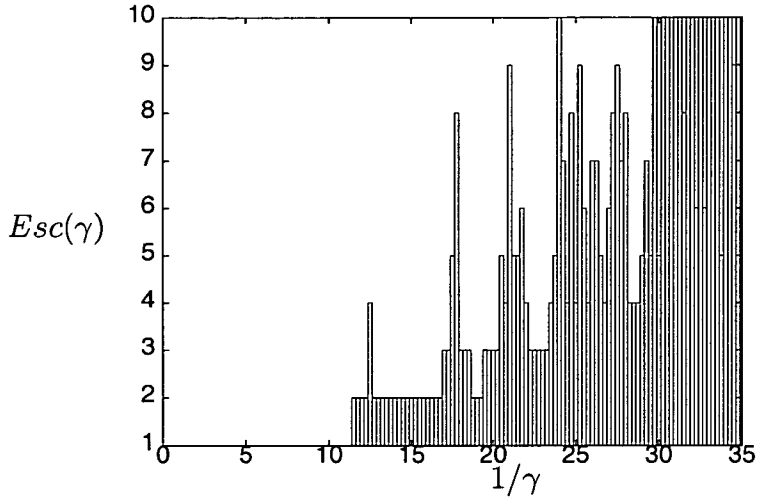

Figure 4.47: The escape time, $Esc(\gamma)$, against the energy, $\frac{1}{\gamma}$ when $e = 0.9$.

4.9 Conclusion

Many of the ideas presented in the previous chapter have been applied to Hill's problem in order to understand the distribution of escape times. Turnstile dynamics, which was used to investigate the transport of phase space in Hénon's model problem, is found to be equally applicable in the case of Hill's problem, with some complications because of its continuous nature.

The Elliptic Hill problem was explored with a view to finding similar structures. Unfortunately, the complexity of the problem, due to the absence of the Jacobi Integral, thwarted attempts at computing an escape flux. The escape phenomenon was therefore investigated by mapping out the stable and unstable regions of phase space. The last section, which deals with impulsive forces at high eccentricities, describes a useful model for understanding how the escape process occurs. It would appear that there are stable orbits which can exist at relatively large distances from the centre of the cluster. These "islands of stability" are apparent from the jagged nature of figs(4.46) and (4.47).

Bibliography

[1] Arnold, V. I., 1978. Mathematical Methods of Classical Mechanics. (Springer-Verlag, New York, Heidelberg, Berlin)

[2] Bak, P. 1986. The Devil's staircase. *Physics Today, December 1986* 38-45

[3] Barrow-Green, J., 1996. Poincaré and the three body problem. (AMS, Providence RI)

[4] Benest, D., 1988. Planetary orbits in the elliptic restricted problem. I - The Alpha Centauri system. *Astron. Astrophys.* **206**, No. 1, 143-146

[5] Benest, D., 1989. Planetary orbits in the elliptic restricted problem. II - The Sirius system. *Astron. Astrophys.* **223**, No. 1-2, 361-364

[6] Benest, D., 1996. Planetary orbits in the elliptic restricted problem. III. The eta Coronae Borealis system. *Astron. Astrophys.* **314**, 983-988

[7] Benest, D., 1998. Planetary orbits in the elliptic restricted problem. IV. The ADS 12033 system. *Astron. Astrophys.* **332** 1147-1152

[8] Binney, J., Gerhard, O., Hut, P., 1985. Structures of surfaces of section. Mon. Not. of the Roy. Astron. Soc. **215**, 59-65

[9] Born, M., 1960. The mechanics of the atom, Frederick Ungar Publishing Co., New York.

[10] Boyd, Patricia T. and McMillan, Stephen L. W., 1993. Chaotic scattering in the gravitational three-body problem. *Chaos*, **3**, No. 4, 507-523

[11] Boyd, Patricia T. and McMillan, Stephen L. W., 1992. Initial-value space structure in irregular gravitational scattering, *Physical Review A*, **46**, No. 10, 6277-6287

[12] Chandrasekhar, S., 1942. Principles of Stellar Dynamics, Dover Publications, New York.

[13] Christou, A., 1994. On the Dynamics of Globular Clusters: Chaos, Lyapounov Orbits and Escapes. MSc Thesis, University of Edinburgh.

[14] Clairaut, A. C., 1747. Du Système du Monde dans les Principes de la Gravitation Universelle. *Mémoirs de l'Académie royale des Sciences de Paris*, 329-364

[15] Contopoulos, G. and Kaufmann, D., 1992. Types of escape in a simple Hamiltonian system. *Astron. Astrophys.*, **253**, 379-388

[16] Darwin, G. H., 1900. Address on presenting the Gold Medal to M. H. Poincaré for his researches in celestial mechanics, *Mon. Not. of the Roy. Astron. Soc.* **60**, 406

[17] Eckhardt, B., 1988. Irregular Scattering. *Physica D*, **33** 89-98

[18] Elson, R. and Hut, P., 1987. Dynamical evolution of globular clusters. *Ann. Rev. Astron. Astrophys.* **25**, 565-601

[19] Erdi, B., 1981. The perturbations of the orbital elements of Trojan asteroids. *Celestial Mechanics*, **24**, 377-390.

[20] Froeschlé, C., 1991. Modelling: An aim and a tool for the study of the chaotic behaviour of asteroidal and cometary orbits. *Proceedings of a NATO Advanced Study Institute on Predictability, Stability and Chaos in N-Body dynamical systems, held August 6-17, 1990, in Cortina d'Ampezzo, Italy. Edited by Archie E. Roy*, Plenum Press, New York.

[21] Fukushige, T. and Heggie, D. C. 2000, The Time Scale of Escape from Star Clusters. *Mon. Not. of the Roy. Astron. Soc.*, **318**, 753

[22] Goldstein, H., 1980. Classical Mechanics, 2nd ed. (Addison-Wesley, Reading, MA)

[23] Haddow, M. and Heggie, D.C., 1996. Three Body Scattering, Summer Report, *Unpublished Manuscript*

[24] Heggie, D. C., 1975. Binary evolution in stellar dynamics *Mon. Not. of the Roy. Astron. Soc.* **173**, 729-787.

[25] Hénon, M. 1969. Numerical Exploration of the Restricted Problem. V. Hill's case: Periodic Orbits and their Stability. *Astron. Astrophys.*, **1**, 223-238

[26] Hénon, M., 1970. Numerical Exploration of the Restricted Problem. VI. Hill's case: non-periodic orbits, *Astron. Astrophys.*, **9**, 24-36

[27] Hénon, M. and Petit, J.M., 1986. Satellite Encounters. *Icarus* **66**, 536-555

[28] Hénon, M., 1988. Chaotic scattering modelled by an inclined billiard, *Physics D* **33**, 132-156

[29] Hill, G. W., 1877. On the part of the motion of the lunar perigee which is a function of the mean motions of the sun and moon, Cambridge, Mass., Press of J. Wilson and son. (also *Collected Mathematical Works* **I**, No. 29, 243-270 (1905))

[30] Hill, G. W., 1878. Researches into the Lunar Theory. *American Journal of Mathematics*, **I**, 5-26, 129-147, 245-260 = *Collected Mathematical Works* **I**, No. 32, 284-335 (1905)

[31] Ichtiaroglou, S., 1980. Elliptic Hill's problem - The continuation of periodic orbits. *Astron. Astrophys.* **92**, No 1-2, 139-141

[32] Ichtiaroglou, S., 1981. Elliptic Hill problem - Families of periodic orbits. *Astron. Astrophys.* **98**, No. 2, 401-405

[33] Kandrup, H., 1998. Phase mixing in time-independent Hamiltonian systems. *Mon. Not. R. Astron. Soc.* **301**, 960-974

[34] Keenan, D.W. 1981. Galactical tidal limits on star clusters. I - Stability of stellar orbits and the zero velocity surfaces. *Astron. Astrophys.* **95**, No. 2, 334-339

[35] Keenan, D.W. 1981. Galactic Tidal Limits on Star Clusters II. Tidal Radius and Outer Dynamical Structure. *Astron. Astrophys.* **95** 340-348

[36] MacKay, R.S., Meiss, J.D., Percival, I.C., 1984. Transport in Hamiltonian Systems. *Physica*, **13D**, 55-81

[37] Marchal, C., 1990. The Three-Body Problem. *Studies in Astronautics 4*, Elsevier Press. New York

[38] Milani, A. and Nobili, A. M., 1984. Dynamical instabilities in the outer asteroidal belt. *Asteroids, comets, meteors. Proceedings of the Meeting, Uppsala, Sweden June 20-22, 1983. Astronomiska Observatoriet* 127-135

[39] Murray, C.D. and Dermott, S. F., 2000. Solar System Dynamics, Cambridge University Press.

[40] Petit, J. M. and Hénon, M., 1986. Satellite Encounters, *Icarus*, **66**, 536-555.

[41] Plummer, H. C., 1960. An Introductory Treatise on Dynamical Astronomy, Dover, New York.

[42] Poincaré, H., 1899. "Les Methodes Nouvelles de la Mecanique Celeste", Gauthier Villars, Paris, Vol. III.

[43] Press, William H. et al. 1992. Numerical Recipes in Fortran 77, 2nd. ed. (Cambridge University Press).

[44] Rom-Kedar, V., Leonard, A., Wiggins, S., 1988. An Analytical Study of Transport, Mixing and Chaos in an Unsteady Vortical Flow, *J. Fluid Mech.*, **214**, 347-394

[45] Ross, J.R., Mennim, A., Heggie, D.C., 1997. Escape from a tidally limited star cluster. *Mon. Not. R. Astron. Soc.* **284**, 811-814

[46] Spirig, F. and Waldvogel, J., 1991. Chaos in coorbital motion. *Proceedings of a NATO Advanced Study Institute on Predictability, Stability and Chaos in N-Body dynamical systems, held August 6-17, 1990, in Cortina d'Ampezzo, Italy. Edited by Archie E. Roy*, Plenum Press, New York.

[47] Spitzer, L., 1986. Dynamical Evolution of Globular Clusters. *Proceedings of a Workshop held at the Institute for Advanced Study, Princeton, USA, June 2-4, 1986. Lecture Notes in Physics, Vol. 267, edited by P. Hut and S. McMillan.*, Springer-Verlag, Berlin Heidelberg New York.

[48] Synge, J. and Griffith, B., Principles of Mechanics, 1959. McGraw-Hill Book Company, Inc., New York

[49] Szebehely, V., 1967. Theory of Orbits (Academic Press, New York)

[50] Szebehely, V. and McKenzie, R., 1977. Stability of the Sun-Earth-Moon system. *A. J.*, **82**, 303-305

[51] Wiggins, S., 1992. Chaotic Tranport in Dynamical Systems. Springer-Verlag, New York.

Appendix A

Integral Formulas

These approximate formulae are used in sec(2.4.1) and sec(2.4.4) and are derived in sec(2.3.1).

$$\int_{-\infty}^{\infty} \dot{\mathbf{R}}.\frac{\partial}{\partial \mathbf{R}}\left(\frac{(\hat{\mathbf{a}}.\mathbf{R})\cos M}{R^5}\right)dt = \frac{\sqrt{\pi}K^{\frac{5}{2}}e^{-\frac{2K}{3}}}{12q^5}\Im\left[(2qi\hat{\mathbf{B}}+2q\hat{\mathbf{A}}).\hat{\mathbf{a}}e^{-int_0}\right] \quad \text{(A.1)}$$

$$\int_{-\infty}^{\infty} \dot{\mathbf{R}}.\frac{\partial}{\partial \mathbf{R}}\left(\frac{(\hat{\mathbf{b}}.\mathbf{R})\cos M}{R^5}\right)dt = \frac{\sqrt{\pi}K^{\frac{5}{2}}e^{-\frac{2K}{3}}}{12q^5}\Im\left[(2qi\hat{\mathbf{B}}+2q\hat{\mathbf{A}}).\hat{\mathbf{b}}e^{-int_0}\right] \quad \text{(A.2)}$$

$$\int_{-\infty}^{\infty} \dot{\mathbf{R}}.\frac{\partial}{\partial \mathbf{R}}\left(\frac{(\hat{\mathbf{a}}.\mathbf{R})\sin M}{R^5}\right)dt = \frac{\sqrt{\pi}K^{\frac{5}{2}}e^{-\frac{2K}{3}}}{12q^5}\Im\left[-i(2qi\hat{\mathbf{B}}+2q\hat{\mathbf{A}}).\hat{\mathbf{a}}e^{-int_0}\right] \quad \text{(A.3)}$$

$$\int_{-\infty}^{\infty} \dot{\mathbf{R}}.\frac{\partial}{\partial \mathbf{R}}\left(\frac{(\hat{\mathbf{b}}.\mathbf{R})\sin M}{R^5}\right)dt = \frac{\sqrt{\pi}K^{\frac{5}{2}}e^{-\frac{2K}{3}}}{12q^5}\Im\left[-i(2qi\hat{\mathbf{B}}+2q\hat{\mathbf{A}}).\hat{\mathbf{b}}e^{-int_0}\right] \quad \text{(A.4)}$$

$$\int_{-\infty}^{\infty} \frac{e^{-in_0t}(\hat{\mathbf{a}}.\mathbf{R})^p dt}{R^5} = \frac{K^{\frac{3}{2}}\sqrt{\pi}e^{-\frac{2K}{3}}}{12nq^4}\left[2(\hat{\mathbf{a}}.\hat{\mathbf{A}})-2qi(\hat{\mathbf{a}}.\hat{\mathbf{B}})\right]^p \quad \text{(A.5)}$$

$$\int_{-\infty}^{\infty} \frac{e^{-in_0t}(\hat{\mathbf{b}}.\mathbf{R})^p dt}{R^5} = \frac{K^{\frac{5}{2}}\sqrt{\pi}e^{-\frac{2K}{3}}}{12nq^5}\left[2q(\hat{\mathbf{b}}.\hat{\mathbf{A}})-2qi(\hat{\mathbf{b}}.\hat{\mathbf{B}})\right]^p \quad \text{(A.6)}$$

$$\int_{-\infty}^{\infty} \frac{e^{-in_0t}(\hat{\mathbf{a}}.\mathbf{R})(\hat{\mathbf{b}}.\mathbf{R})dt}{R^5} = \frac{K^{\frac{5}{2}}\sqrt{\pi}e^{-\frac{2K}{3}}}{12nq^5}[2q(\hat{\mathbf{a}}.\hat{\mathbf{A}})-2qi(\hat{\mathbf{a}}.\hat{\mathbf{B}})]$$

$$\times[2q(\hat{\mathbf{b}}.\hat{\mathbf{A}}) - 2qi(\hat{\mathbf{b}}.\hat{\mathbf{B}})] \tag{A.7}$$

$$\int_{-\infty}^{\infty} \dot{\mathbf{R}}.\frac{\partial}{\partial \mathbf{R}}\left(\frac{(\hat{\mathbf{a}}.\mathbf{R})^p \cos E}{R^7}\right) dt = \frac{K^{\frac{7}{2}}\sqrt{\pi}e^{-\frac{2K}{3}}}{120q^7}\Im\left([(2qi\hat{\mathbf{B}} + 2q\hat{\mathbf{A}}).\hat{\mathbf{a}}]^p e^{-int_0}\right) \tag{A.8}$$

$$\int_{-\infty}^{\infty} \dot{\mathbf{R}}.\frac{\partial}{\partial \mathbf{R}}\left(\frac{(\hat{\mathbf{a}}.\mathbf{R})^p \sin E}{R^7}\right) dt = \frac{K^{\frac{7}{2}}\sqrt{\pi}e^{-\frac{2K}{3}}}{120}\Im\left(-i[(2qi\hat{\mathbf{B}} + 2q\hat{\mathbf{A}}).\hat{\mathbf{a}}]^p e^{-int_0}\right) \tag{A.9}$$

$$\int_{-\infty}^{\infty} \dot{\mathbf{R}}.\frac{\partial}{\partial \mathbf{R}}\left(\frac{(\hat{\mathbf{b}}.\mathbf{R})^p \cos E}{R^7}\right) dt = \frac{K^{\frac{7}{2}}\sqrt{\pi}e^{-\frac{2K}{3}}}{120}\Im\left([(2qi\hat{\mathbf{B}} + 2q\hat{\mathbf{A}}).\hat{\mathbf{b}}]^p e^{-int_0}\right) \tag{A.10}$$

$$\int_{-\infty}^{\infty} \dot{\mathbf{R}}.\frac{\partial}{\partial \mathbf{R}}\left(\frac{(\hat{\mathbf{b}}.\mathbf{R})^p \sin E}{R^7}\right) dt = \frac{K^{\frac{7}{2}}\sqrt{\pi}e^{-\frac{2K}{3}}}{120q^7}\Im\left(-i[(2qi\hat{\mathbf{B}} + 2q\hat{\mathbf{A}}).\hat{\mathbf{b}}]^p e^{-int_0}\right) \tag{A.11}$$

$$\int_{-\infty}^{\infty} \dot{\mathbf{R}}.\frac{\partial}{\partial \mathbf{R}}\left(\frac{(\hat{\mathbf{a}}.\mathbf{R})^p(\hat{\mathbf{b}}.\mathbf{R})^q \cos E}{R^7}\right) dt = \frac{K^{\frac{7}{2}}\sqrt{\pi}e^{-\frac{2K}{3}}}{120q^7}\Im\Big([(2qi\hat{\mathbf{B}} + 2q\hat{\mathbf{A}}).\hat{\mathbf{a}}]^p$$
$$\times[(2qi\hat{\mathbf{B}} + 2q\hat{\mathbf{A}}).\hat{\mathbf{a}}]^q e^{-int_0}\Big) \tag{A.12}$$

$$\int_{-\infty}^{\infty} \dot{\mathbf{R}}.\frac{\partial}{\partial \mathbf{R}}\left(\frac{(\hat{\mathbf{a}}.\mathbf{R})^p(\hat{\mathbf{b}}.\mathbf{R})^q \sin E}{R^7}\right) dt = \frac{K^{\frac{7}{2}}\sqrt{\pi}e^{-\frac{2K}{3}}}{120q^7}\Im\Big(- i[(2qi\hat{\mathbf{B}} + 2q\hat{\mathbf{A}}).\hat{\mathbf{a}}]^p$$
$$\times[(2qi\hat{\mathbf{B}} + 2q\hat{\mathbf{A}}).\hat{\mathbf{b}}]^q e^{-int_0}\Big) \tag{A.13}$$